ShadX Presents:
SPRICHO
"An On-Demand Energy-Efficient E-VTOL Airtaxi"

AIAA Graduate Team
Aircraft Design Competition
2018-2019

MAY 2019

Yasamin Karamian
Wight Estimation,W&B
984190

S. Reza Fattahi M.
Project Advisor
AFCS Design &
Flight Simulation

Farid Rassouli
Team Leader
920911

Prof. S. Mohammad B. Malaek
Faculty Advisor

Hossein Akbari
Aerodynamics, CFD
984028

Mohaddeseh Ghasemi
Structural Design, FEM
978756

Alireza Akbari
Electric Propulsion System
984891

Mohammad Reza Najafi
S&C, Autonomy
984026

Mohammad Alizadeh
Cost Analysis, Systems
983762

Mohammad Hassan Sabeti
CAD & 3D Modeling
1003554

Zahra Saedi
Market Analysis
983781

Mohammad Mehdi Mohammadi
Performance Analysis, Configuration
984069

1. Executive Summary

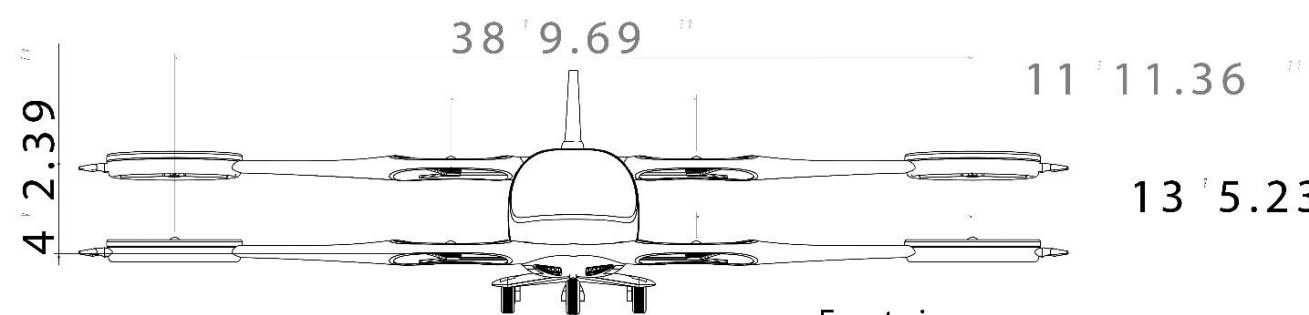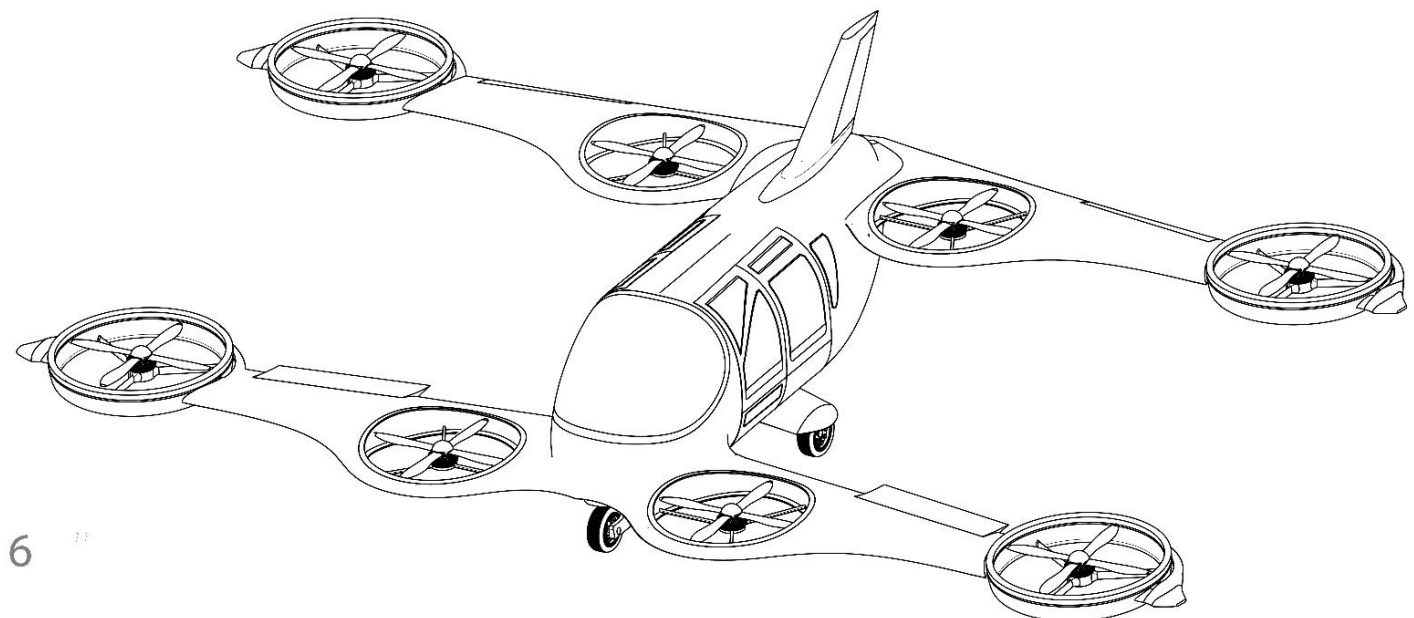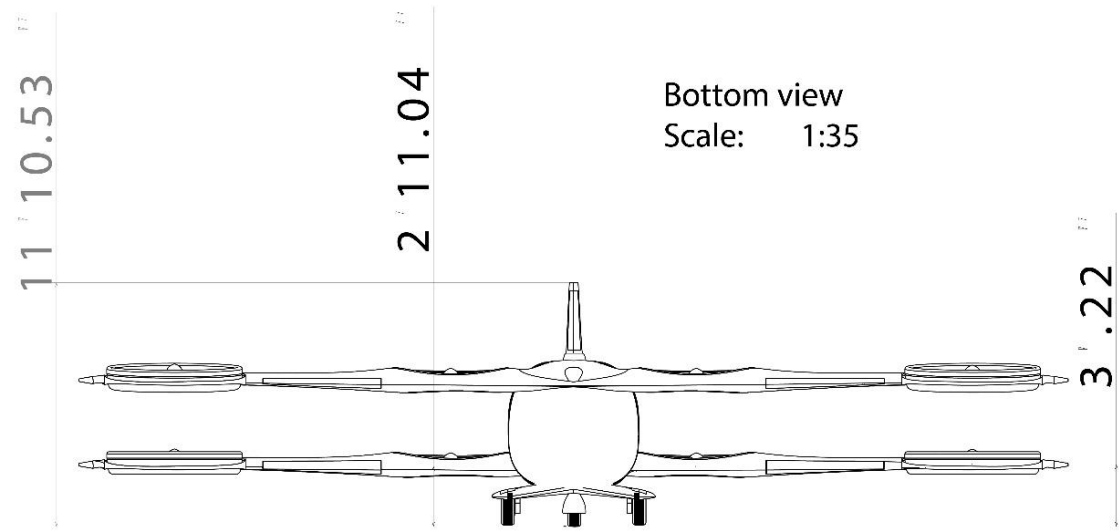*"Without proper planning the history repeats itself." — anonymous*

By the 1870s, New Yorkers were taking over 100 million horsecar trips per year and by 1880 there were at least 150,000 horses in the city that required a credible workforce to just clean the streets from their drops. The situation became intolerable until Henry Ford introduced affordable personal vehicle for transportation. Currently, there are more than seven million vehicles in the New York city and the history is getting ready to repeat itself. In fact, this proposal is the team ShadX2019's response to the AIAA's 2019 Graduate Team Aircraft Design Competition RFP for an E-VTOL flight vehicle to meet ODM/UAM requirements.

Developments of high-tech electric motors and batteries have been a growing allure for aerospace engineers to propose new designs that are more in line with other green sustainable products. We firmly believe that all-electric flying vehicles will attract interests of most populated cities municipalities and aviation industry stakeholders. The goal here is to create a sound and sustainable means for transportation for the near future and even a step toward the lure of "everyone may fly" dream. We are certain that our success would be a giant leap towards this dream.
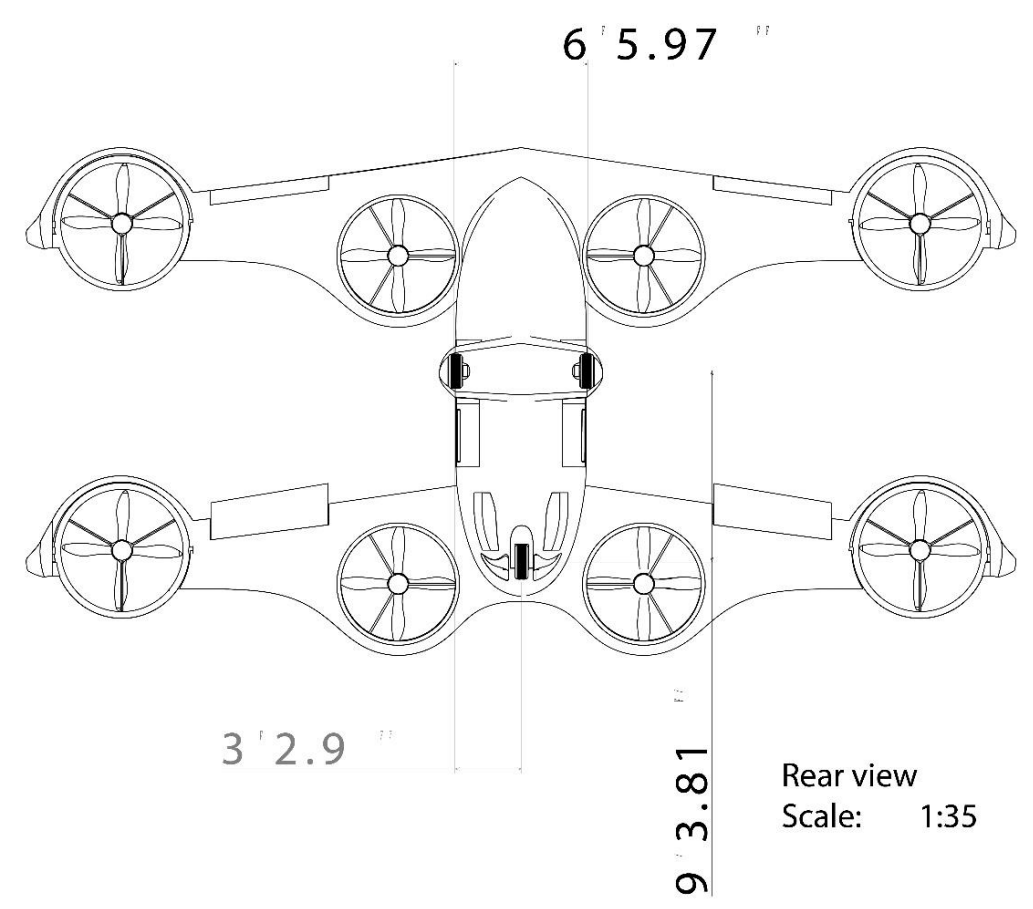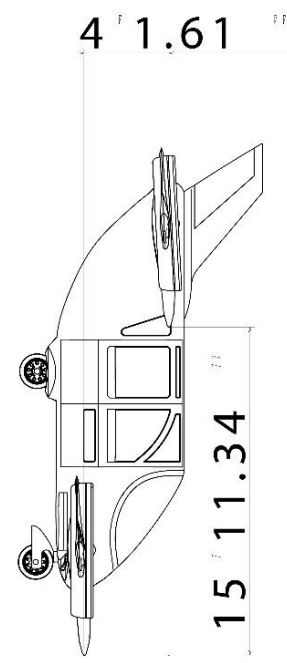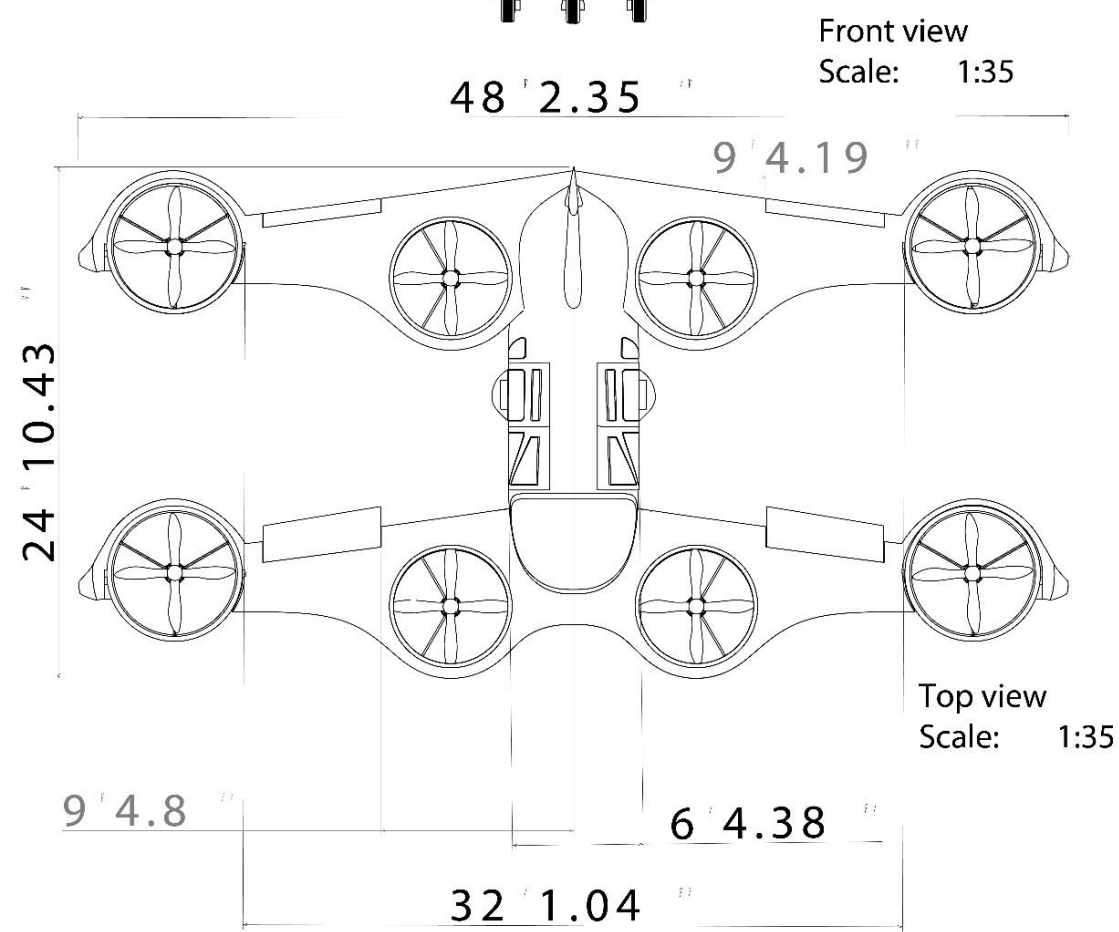
With the help of "especially tailored design cycle" Spricho has been meticulously examined for both safety and handling issues. Spricho design is mainly inspired by the "Fault-tolerant design philosophy". The implemented redundancies ensure a safe response to the UAM objective for flying over and in the vicinity of the populated cities.

One of the most significant achievements of Spricho is its capability of autonomous flights with accepted level of safety. Market study reveals that in the future, autonomous vehicles become a dominant mode of land transportations. Therefore, we believe autonomous flights vehicles follow suit. Nonetheless, we must think of an optimized flight network over the US by considering disparate market scenarios. However, we must stick to our ODM concept to gain market trust and to avoid undue risks.

we at ShadX are clearly aware that any existing aircraft "Cost Estimation Relationships" could hardly be suitable for E-VTOLS. Therefore, we developed a tailored cost model to predict the production as well as operation cost of such aircrafts and especially for Spricho. The preliminary studies have made us certain that a unit cost of less than 500,000 USD and a total operating cost less than 180 USD/hour would well be justified. This approach allows us to propose a production plan that gives %15.6 profit margin during a 22-year production with enough confidence. This is a sound and scientific way to attract more launch customers and definitely help finance the project.

Bottom view
Scale: 1:35

11'10.53"

2'11.04"

3'.22"

38'9.69"

4'2.39"

11'11.36"

13'5.23"

Front view
Scale: 1:35

Isometric view
Scale: 1:35

48'2.35"

9'4.19"

4'1.61"

6'5.97"

24'10.43"

15'11.34"

Top view
Scale: 1:35

9'4.8"

6'4.38"

32'1.04"

Left view
Scale: 1:35

3'2.9"

9'3.81"

Rear view
Scale: 1:35

2. Table of Content

3. Abbreviations

Symbol	Description	Symbol	Description
CG	Center of Gravity	Max Q	maximum value of dynamic pressure
AFCS	Automatic Flight Control System	TCAS	Traffic Collision Avoidance System
RPM	Rounds Per Minute	NSP	Navigation/Anti-collision Strobe/Position
GA	General Aviation	AGL	above ground level
$W_{battery}$	Weight of Battery	IFR	Instrument Flight Rules
W_{motor}	Weight of motor	VFR	Visual Flight Rules
$D_{transition}$	Transition Distance	IoT	Internet of Things
LFC	Life Cycle Cost	F_{dif}	judgmental factor for difficulty (i.e. complexity)
AOA (α)	Angle of Attack	F_{CAD}	judgmental factor for the effect of computer aided design
MGC	Mean Geometric Chord	RoD	Rate of Descend
$\Lambda_{c/4}$	Quarter Chord Sweep	TAS	true air speed
Cl	Coefficient of Lift	e	Oswald's efficiency factor
Cd	Coefficient of Drag	ft	foot unit
cd_0	Zero lift drag coefficient	FAR	Federal Acquisition Regulation
mph	mile per hour	MSL	Mean Sea Level
W_{TO}	Takeoff weight	fpm	foot per minute
e_x	Modified Span Efficiency Factor	DL	Disk Loading
kW	kilowatt	RoC	Rate of Climb
kg	kilogram	lb	Pound
HP	horsepower	C_T	thrust coefficient
Wh	watthour	X_{CG}	X location of gravity center
TRL	Technology readiness level	$\bar{V}_v$	Vertical tail volume coefficient
DC	direct current	X_v	Vertical tail moment arm
AC	Alternating current	$S_{v,initial}$	Initial vertical tail area
λ	Taper ratio	$S_{v,final}$	Final vertical tail area
S	Wing area	Λ_{LE}	Leading edge sweep angle
N_D	drag induced yawing moment	$c_{n\beta}$	yawing moment coefficient due to sideslip
N_t	critical engine-out yawing moment	AR	Aspect ratio
AAA	Advanced Aircraft Analysis	PAX	Passenger allowed in expenses
h	Flight altitude	I_{XX}	Rolling moment of inertia
δ_{CV}	Canardvator deflection angle	I_{YY}	Pitching moment of inertia
δ_r	rudder deflection angle	I_{ZZ}	yawing moment of inertia
DOF	Degree of freedom	I_{XZ}	XZ product of inertia
J_{RD}	ride discomfort index	I_{rot}	Rotor moment of inertia
ζ	Damping ratio	OEI	One engine inoperative
T_{half}	Time to halve the amplitude	N_{δ_r}	yawing moment due to rudder deflection
τ	Roll mode time constant	N_{δ_T}	yawing moment due to required differential thrust
ω_{n_D}	Dutch roll undamped natural frequency	δ_T	required differential thrust
ζ_D	Dutch roll damping ratio	y_t	Motor moment arm
PID	proportional–integral–derivative	q	Air dynamic pressure
V_{stall}	Stall velocity	β	Sideslip angle
φ_T	Thrust –line inclination angle	$L \& P$	Leakage and protuberance

Compliance Matrix		
Parameter	RFP	Spricho
General		
Num. of Occupants	4	4
Autonomous Flight	Optional	✓
EIS	2028	2028
Performance		
Cruising Alt. [ft.] MSL	≥ 1500	1500 2500 3500
Avg. Speed (transition， climb， cruise， descent) [mph]	≥ 150	150
Hover Alt. [ft.]	50	50
Avg. ROC $[\frac{ft}{min}]$	≥ 500	1000
Range [mile]	60	99
Instantaneous Decent Rate $[\frac{ft}{min}]$	≤ 1000	1000
Max. Speed @ 50% payload [mph]	≥ 176	207
Max. Speed Demonstration Alt. [ft.] MSL	1500 to 3500	1500
Assumed Battery Energy Density $[\frac{W，}{kg}]$	≤ 450	381

General Characteristics	E-SP608 "Spricho"
Num. of Occupants	4
Length $[ft]$	24.8
Height $[ft]$	11.8
Wing Span $[ft]$	31.92
Total Wing Area (tandem) $[ft]$	176
M.A.C $[ft]$	4.99
Empty Weight (w/o autonomy) $[lbs.]$	3582
Max. Takeoff Weight $[lbs.]$	4371
Battery Weight $[lbs.]$	1230
Fixed-wing Max. ROC @ SL $[fpm]$	2460
Rotor-craft Max. ROC @ SL $[fpm]$	2100
Max Level Speed $[kts]/[mp，]$	169/194
Max. Speed @ 50% payload $[kts]/[mp，]$	207
Cruise Alt. [ft.] MSL	1500 2500 3500
Hover Alt. [ft.]	50
Avg. ROC $[\frac{ft}{min}]$	1000
Range $[mile]$	99
Instantaneous Decent Rate $[\frac{ft}{min}]$	1000
Max. Speed Demonstration Alt. [ft.] MSL	1500
Assumed Battery Energy Density $[\frac{W，}{kg}]$	381
Wing Loading $[\frac{lb.}{ft^2}]$	24.88
Fixed-wing Power Loading $[\frac{lb.}{，p}]$	8.33
Rotor-craft Power Loading $[\frac{lb.}{，p}]$	5.56
Disk Loading $[\frac{lb.}{ft^2}]$	20.48
Hover Ceiling $[ft]$	8500
Static Margin	[20.92% to 31.27%]
Max CG Excursion	30.04% M.A.C
Max. Design g-Load	[+3.8/-1]
Unit Cost $[\$K]$	499
Operating Cost $[\frac{\$}{，r}]$	176.4
EIS	2028

4. Design Strategy

The RFP requests a four-passenger E-VTOL aircraft with concept of ODM/UAM. Spricho design process begin with studying the real-world market. We start to analyze all of the functions that an E-VTOL could have, and based on that analysis we choose to compete as an air taxi & sightseeing air vehicle. These functions lead us to determine these three main objectives in our design strategy:

- **Safety:** flying over cities and urban areas made us to consider safety as one of main objectives in our design.

- **Marketability:** UAM/ODM is a modern concept but at the same time it has a fast-growing market that makes it hard for every aircraft of this category to compete, so we find and contemplate the market factors that will assure our predominance in future competitive market. These factors are short turnaround time (ODM), being economical competing urban taxis and visually appealing.

- **Energy efficiency:** Electric aircraft sensitivity to weight forces us to minimize the energy consumption in order to minimize the battery weight we need during the flight.

As shown in Figure 1 after investigating the whole market, a comprehensive configuration study was performed, and we reached 5 final configurations. Then a conceptual sizing was done for preliminary selected alternatives in order to find the most agreeing configuration with design objectives (section 8.). In this point, we at ShadX, started to develop a novel energy-based optimization method which has been implemented throughout the preliminary design.

Enjoying the results of extensive configuration study, we figure out all of these configurations have different methods of control and structural analysis since they are totally novel. So, we decided to focus on these two sections to reach accurate results.

The steps in the design process from initial design to preliminary design are illustrated in Figure 1. Numerical methods (CFD and FEM) was executed to support the decisions made during process.
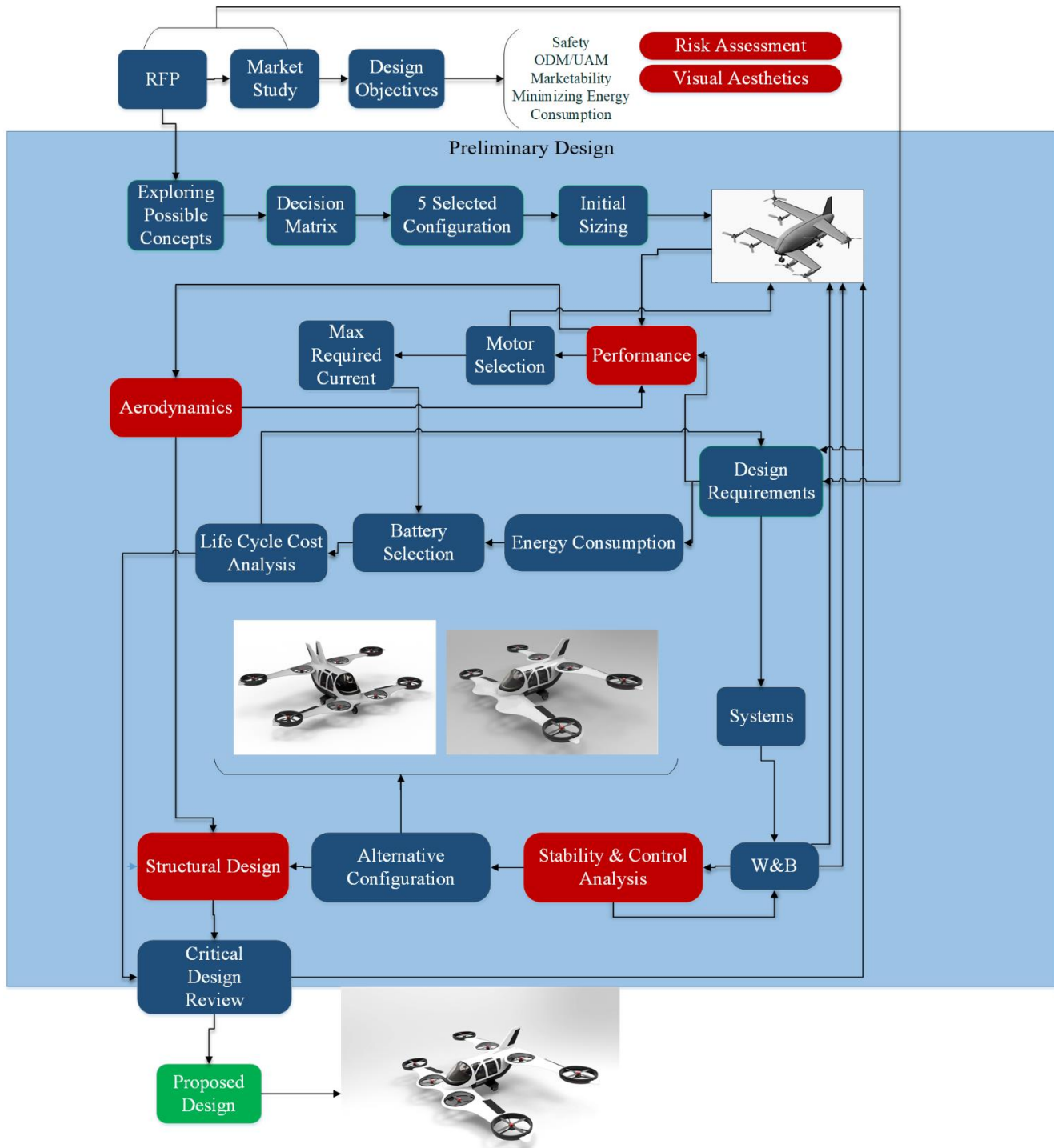
Figure 1: ShadX Design Cycle

5. Market Analysis

As shown in Figure 1, Spricho design cycle starts with market analysis which is discussed in this chapter.

5.1. Target Market Segment & Customers

Since urban air transportation is a totally new concept, its customers behavior is currently ambiguous. But due to the following reasons, we expect that the E-VTOL target market is air-taxi users.

First, E-VTOL aircrafts would be too expensive to be used as a personal car. Second, special parking lots should be considered for E-VTOL aircrafts which are not compatible with current parking lots and garages, and it would take a long time for new-designed parking lots to be widely implemented in the cities, this problem exists for landing ports too, recharging and maintenance equipment for E-VTOL is not widely available neither, So it is expected that in the early years, the E-VTOL category would be mainly used as air-taxi which illustrates our target market segment and customers.

5.2. Defining the Target Regional Market

Customers' preferences may differ around the world, so we start with defining the main market target region. The north America is the largest market for GA with 69.6 percent market share in 2016. Due to year 2016 statistics, among north America countries US has the largest market with 211793 active GA aircrafts, followed by Canada with 36436 [1]. From the macroeconomics point of view, US has the largest GDP with expected 2.3 percent annual growth which supports its pioneering in GA market. Hence, we have defined the US GA market as our target market.

Large and crowded cities are suitable for E-VTOL air taxis to operate. We at ShadX have chosen
San Francisco as our target region. The city that 32% of its residents use public transportation for their daily commute, ranking it first on the west coast and third in the United States [3].

According to the Figure 2, which determine the most important parameters during a survey for passengers who use taxis, objectives are chosen to be: 1) Ease of payment 2) Short wait time 3) getting to the destination as fast as possible. Here, the "Lean Market" method is used [4], [5]. The proposed system is based on data derived from potential customers.
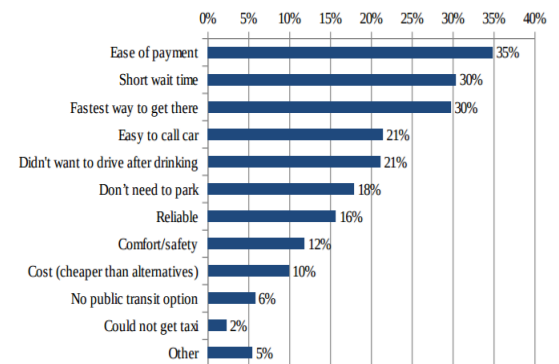

Figure 2: Responses to the reason of using taxis

5.3.   Infrastructure Requirements Management

In this part, we investigate the required infrastructure for E-VTOL Air-taxi. The main objectives of this part are defining the stations number and location, as well as the number of required aircrafts.

5.3.1. Urban Air taxi

Since Uber customers' behavior is the closest to our potential clients, its requests' data (geographic coordinates of origins, destinations, day of the week, hours and number) in San Francisco is used for modeling the transportation system. The data from the survey is used to make a distribution map of Uber users using Tableau software.

By clustering the Uber's data [7], the most crowded areas have been determined and we decided to build the vertiports at these areas which have the most requests with two considerations. First, the value of minimum distance between two stations is calculated based on the fact that short distances using a taxi is faster than our service. However, as the travel distance increases the duration of flying between the origin and destination is remarkably less than driving the same distance. A distance at which the duration of flying and driving is equal is chosen as the minimum distance. It is shown in Figure 3 for San Francisco, and the value is found to be 0.8 mile.
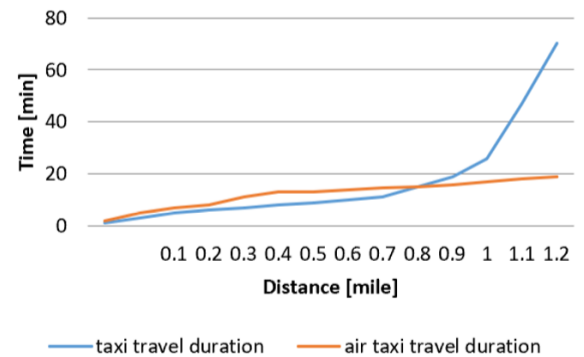

Figure 3 Time travel of taxi and air-taxi in distances

Second, The concentration of transportation requests peaks slants from residential areas in the morning toward business areas in the evening. Considering the peak hours' demand in specifying the stations' capacity will impose a prohibitive cost to the system, and not considering them will cause a profit reduction. To solve this, we change the architecture of stations located in urban areas; the number of residing air taxis in the stations reduce, and in return, the number of landing pods increase. (Type II stations in Section 5.3.4).

By solving these problems, the distribution of the stations is determined as shown in Figure 4. Assuming there are two other rivals, only one-third of market is within the reach.
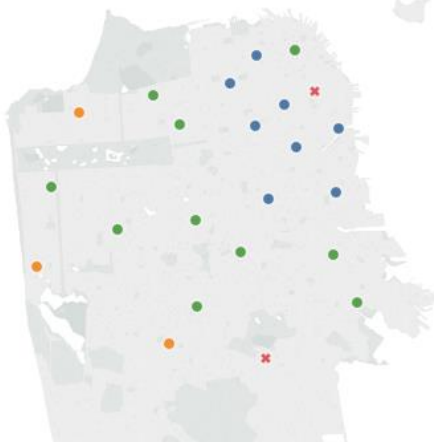
Figure 4: Finally determined vertiports

Table 1: Number of cities and vertiports

Number of cities	5
Number of station type I in each city	7
Number of station type II in each city	10

There are twenty cities in the vicinity of San Francisco and the explained procedure is done for these cities and five cities are found to be appropriate for air taxi operation. The avarage number of stations are tabulated in Table 1.

The revenue and cost of urban air taxis are summarized in Table 2.

Table 2: Cost and profit estimation in first year for urban

First year profit	Cost	Income	
-1.53 %	218.4 M USD	**Average ticket price:**	50 $
		Average number of customers in first year:	1.7 M

It shows that during the five first years of operation, the least profit of 15 percent is not achievable for urban operations. Therefore, to increase the profit, our selected to entry to market changes (Section 5.40).

5.3.2. **Suburban Air Taxi**

Spricho also has the potential for competing in intercity trips, since its cost of intercity usage is lower than its taxi counterpart, and it reduces the duration of travel considerably. Moreover, in spite that the number of intercity trips is lower than the trips in the city, transportation options are limited compared to urban areas so we can draw customer's attention.
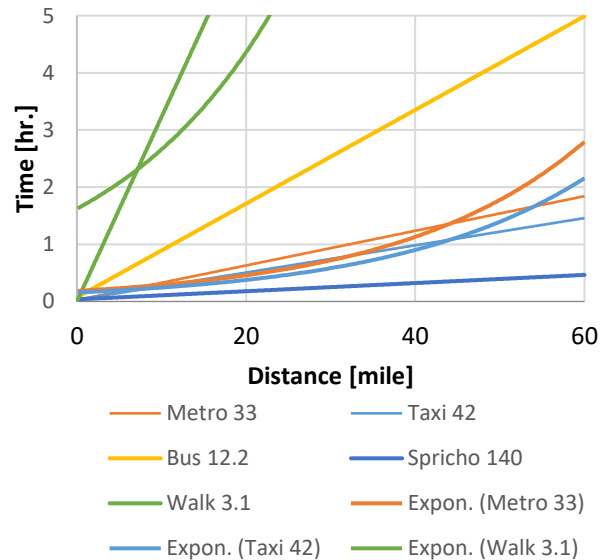

Figure 5: comparing of types of transportation

After evaluating the target area, 30 stations are allocated to 20 cities. Some cities have two stations and others have one station. The outcome of suburban air taxi's financial analysis is summarized in cost analysis.

Table 3: cost and profit estimation in first year for suburban

First year profit	Cost	Income	
+12 %	138.7 M USD	**Average ticket price:**	87 $
		Average number of customers in first year:	1.7 M

5.3.3. **Sightseeing Air Taxi**

This mission is proposed in order to introduce our product to the market. In addition, this mission is used to test the product to find possible minor problems and solve them and gather data from the customers' behavior and improve the related aspects before the final project is launched. In overall, 18 stations are assigned for sightseeing in the targeted region.

5.3.4. **Types of Stations**

Types of our ground stations differ due to their function. The characteristics of each type is investigated here.

Type I stations: These stations are located in administrative and commercial areas. There is a 24/7 demand for our service in these areas.

Type II stations: These stations are located in residential areas. They act as hubs to daily commuters in the rush hours where and when there are many customers. Since these stations are only crowded at certain times of the day, the number of permanent air taxis is low, and in return, there is enough landing space required to respond to the peak time.

Sightseeing stations: These stations are the ones to build and operate. As explained earlier, in the first two years of running the system, they are entertaining sites located in the cities. After launching into the urban market, they are used as urban stations.

Main port: Traveling between cities is only possible from the main ports. Main ports are a large station with a high frequency of T.O. and landings. Each city can have one or more main ports.

Table 4: characteristics of stations

	Number of stations	Number of landing pods	Number of air taxis	Servicing hours
Type I Station	7	4	6	24/7
Type II Station	10	4	3	18 hours
Sightseeing Station	3	2	4	12 hours
Main Station	30	13	10	24/7

5.3.5. Ground Support Requirements

Maintenance and Repairing: For basic checks, additional space is considered in the stations. For overhauls, there are special stations. For instance, three stations are considered in San Francisco.

Emergency: There is a first aid kit in each aircraft. In stations, the required firefighting, EMS, and power cutoff equipment is arranged. The stations are never fully occupied and there is always enough space for emergency landing or needed rescue helicopters.

ATC: There is one ATC center for the whole region and there is at least one dispatcher in each station for organizing the stations.

5.4. Market Timeline

Typically, a new product goes through the stages shown in Figure 6 during its life span [6].

The air taxi growth period starts when the product is trying to gain a toehold in the market. It is followed by the sustainability period when enough people are familiar with the product and its use has become widespread. Here, estimating the number of E-VTOL air taxis and stations are based on the stabilization period.
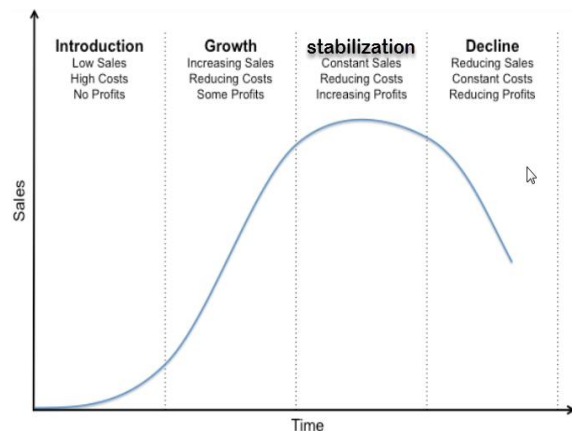

Figure 6: Service life cycle [6].

The market development of Spricho is shown in Figure 7.

Manufacturing should start two years before EIS in 2028, and by that time two hundred aircrafts will be manufactured and stored in hangars. There will be no income, and expenses of storing as well. Also, entering the market will face some drawbacks. But, despite all of these drawbacks, we set a timeline and contemplate a strategy to sell our product and reach the target profit. This timeline is explained in the following sections.
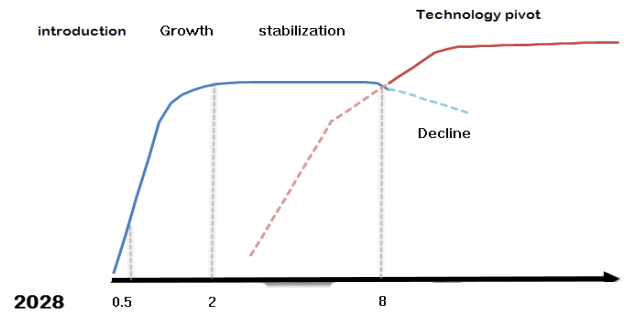

Figure 7: Service life cycle for Spricho

Introduction: The sightseeing will be the target mission, in order to introduce the product to the market in the first six months of 2028. During this time, the storing expenses are reduced, and the product is introduced to people.

This mission will help us gathering data from customers and their preferences for improving the final prototype before its launch.

Growth: After six months, enough products (two hundred and fifty) are manufactured to run the intercity air taxi transportation system. It takes 18 more months for the market to grow and reach the stabilization period. The mentioned number of stations is for when the market is stabilized.

Stabilization: In the second year, the number of active air taxis will be suitable for entering the urban market. The number of trips in urban areas makes them potentially a lucrative target. However, it is mentioned earlier that the urban air taxis are not profitable in the first years as it seems it cannot attract enough customers. This issue is addressed with changing the time of entering into the urban market. The intercity operation provides people with enough time to get accustomed to this new mode of transportation and also helps the developer to better plan to enter this part of the market with tailoring the product and services to increase profitability.

Decline: Every product faces a decline phase in the number of its customers through its life span. In order to prevail and survive in the market, innovative strategies are needed.

Technology pivot & Rejuvenation: With introducing the novel autonomous technology and incorporating them into our product, the costs are decreased, and the efficiency of the system is increased. The result is providing services to more customers and decreasing the waiting time. Cost verification of this phase is discussed in cost chapter.

.

other Flight corridors:
Aircrafts which fly in other corridors to
avoid midair collision.

Approach and Descent:
Air taxi lands in determined landing pod.

Accident and Emergency:
Existing at least one pod for emergency and
accident is obligatory in every vertiports.

Parking lot:
Considered places for for aircrafts to stop.

Battery Charging Chambers
underground chambers where we put
batteries to charge

**passengers' boarding
and egress:**
this process will be taken
in landing pods.

Recharging the battery:
Batteries are recharged and replaced via
robotic arms and ground recharging.

Take off and Climb :
ATC will assign the corridors to each aircraft.
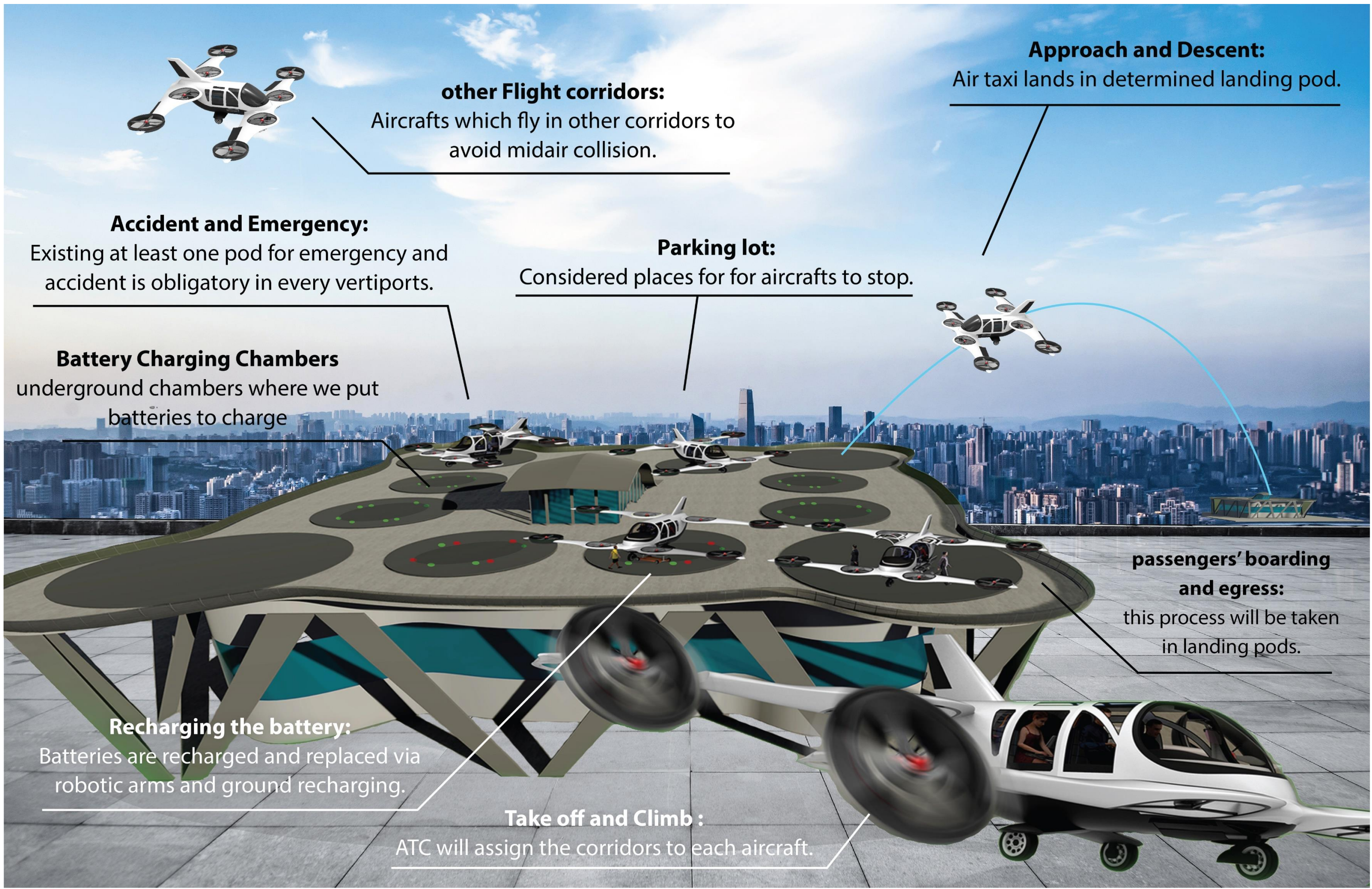
6. Autonomous System for Spricho

Current trend of technology alongside with RFP's implication suggest, ShadX is moving toward incorporating an autonomous system. Using an autonomous system offers the benefits of reducing the cost and increasing safety as it eases the control complexities associated with the transition between rotorcraft and fixed-wing mode. In addition, it eliminates the pilot's error as indicated in D. Kenny's report "Aviation Accidents in 2014", pilot error consistently is the primary cause of 75% of all general aviation accidents. [11] Moreover, it increases the number of passengers by one thereby increasing the gained profit per each flight.

6.1. Factors Influencing on Airplane Status

Factors affecting the condition, route, stability of the aircraft are divided into two categories Figure 8:

- **Static factors:** Factors that determine the beginning of the flight and are almost predictable.

- **Dynamic factors:** These unpredictable factors are already in place and may cause disturbance in the safety of passengers during flight.
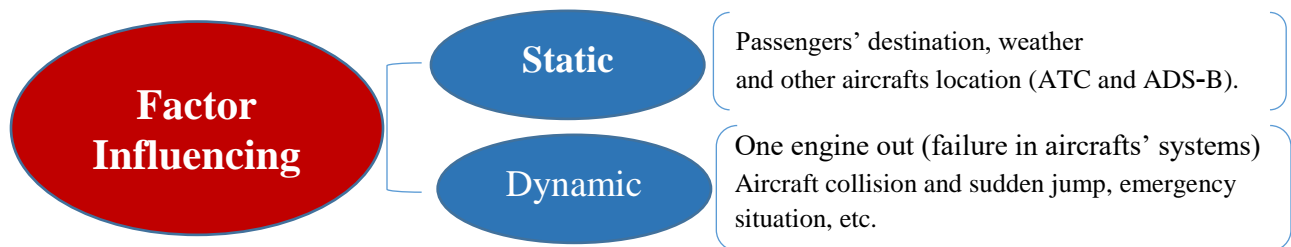

Figure 8: influencing factors on airplane status

6.2. Computer Systems

Aircraft computers consist of two parts:

1) Hardware including memory (database), CPU, GPU, sensors, ADS_B

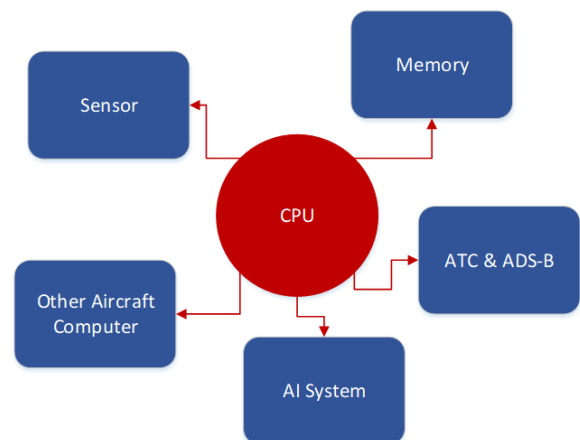2) Software including neural network, searching software, etc.

Figure 9: aircraft computer in autonomous

CPU is an important part of aircraft computer bridging different parts together and searching software is programed on CPU.
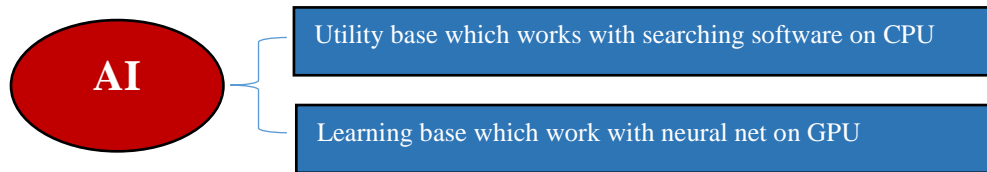
6.3. Autonomous system (HACS)

Autonomous system is a decision making unit in aircraft interacting with other aircraft's computers (engines computer, FCS, etc.).

Clients submit their request via Spricho mobile application. This request alongside all the other requests is gathered in the main computing server embedded in ATC. Then, the flight missions are produced based on an algorithm using all required data such as air traffic, weather, etc. Then, the results are sent to aircraft computer.

Spricho's autonomous system is HACS (Hybrid Autonomous Control System) deciding with artificial intelligence software which is programed in GPU and CPU.

According to [12] Spricho's artificial intelligence utilize two methods: 1) learning base, 2) utility base

AI

Utility base which works with searching software on CPU

Learning base which work with neural net on GPU

Figure 10: AI system's parts

- **Utility base:** This method addresses the static factors to find the best flight path, cruise speed, and mission
- **Learning base:** This method addresses the dynamic factors such as emergency situations and uses a neural network for decision making.

6.4. Learning Method and Autonomous Justification

A neural network requires to be trained. To do so, flight information is transmitted to the network. Meanwhile, the aircraft is controlled by a pilot in dynamic factors such as emergency situations. In addition, in order to increase the autonomous system reliability, all previous aircraft accidents (which are gathered in accident reports including phenomenon such as microburst, bird strike, etc. should be simulated for our learning system, thereby Spricho's autonomous system reliability would be more than any pilot in the history. After training is completed, the neural network controls the aircraft but still, there is a pilot to correct neural network's possible mistakes. The pilot will be removed after these four steps (Figure 11).

6.5. The Verified time for autonomous entry into service

According to [13], this method of learning requires a period of time for training that will be calculated from the Equation 1. According to [13], due to the level of Spricho's autonomy complexity, which is required for civil aircraft, n is equal to four. Therefore, after three years Spricho autonomous system is trained and needs two years to be tested. After five years, the autonomous system is ready to be certified. According to the certification's dataset [14], this process takes up to three years. Hence, the autonomous system development takes eight years to be completed overall. Afterwards, the pilot can be substituted with one passenger. The effect of this change is discussed in section 5 and 20.

$$t = Omega\ (n \log n)$$

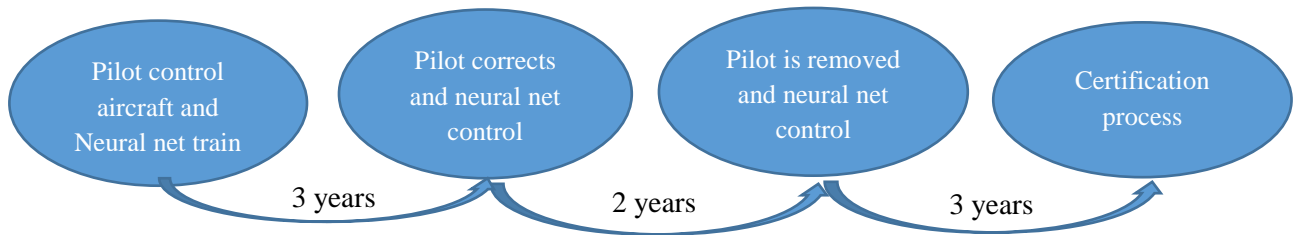*Equation 1: Autonomous training time*

Figure 11: autonomous trend

Finally, AI system transmits data to the CPU and CPU transmits data to PID control system. Hence, Spricho's flight control has two parts: First, a PID controller for known trajectories (static system); and second, an AI system which is proposed with the learning capability (Dynamic system).

To ensure the safety of flight, Spricho has two autonomous system. If the primary unit fails, the other one assume its responsibilities.

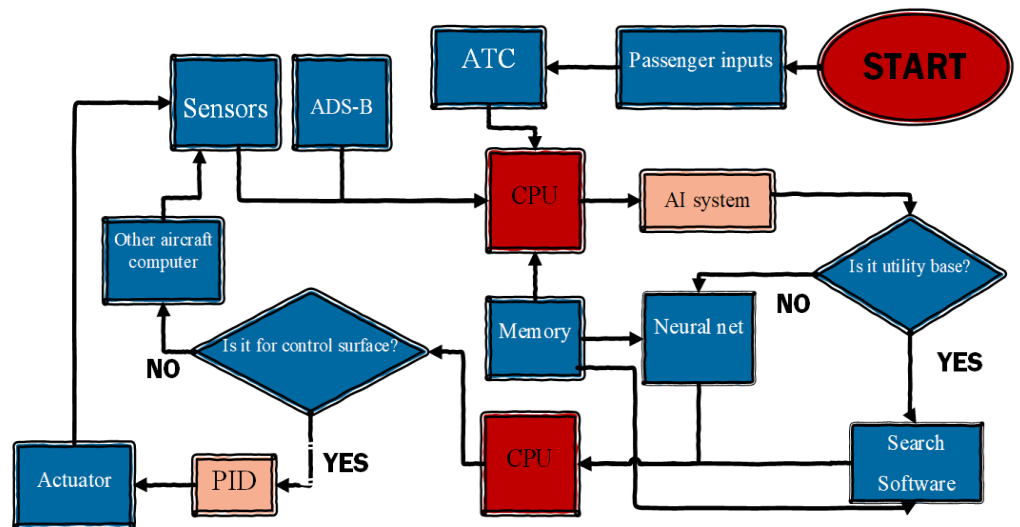In the following diagram the autonomous cycle and how it operates is illustrated in figure 12.

Figure 12: Autonomous System cycle and architecture

7. Mission Analysis

7.1. Mission Description

According to the proposed transportation model in section 5, there are rush hours during a day especially in administrative and commercial areas. In order to respond to the high number of requests from busy areas in a short time, aircrafts from not crowded areas are needed to assist transporting the passengers. It suggests a mission consisted of three separate legs without replacing batteries however in shorter distances.

A schematic overview of the designed mission is provided in Figure 15. All missions' properties is described in Table 5. This mission is referenced as 3 stop mission in the other sections. Note that the reserve mission is the same for all missions and is sized based on the RFP.

Figure 15: Three Stop Mission

Intercity travel is an important part of entry to the market strategy. The traveled distance during this mission is based on RFP's sizing mission. It is also verified in section 5. However, as explained in Section 10.3.1 it offers an extended range as shown in Figure 15. The schematic overview of the mission and reserve mission is provided in Figure 15

Figure 15: Long Range Mission

As stated in the section 5, the sightseeing mission is another part of entry to market strategy. The schematic overview of the mission is provided in Figure 15. The available hover time has been calculated based section 10.3.1.
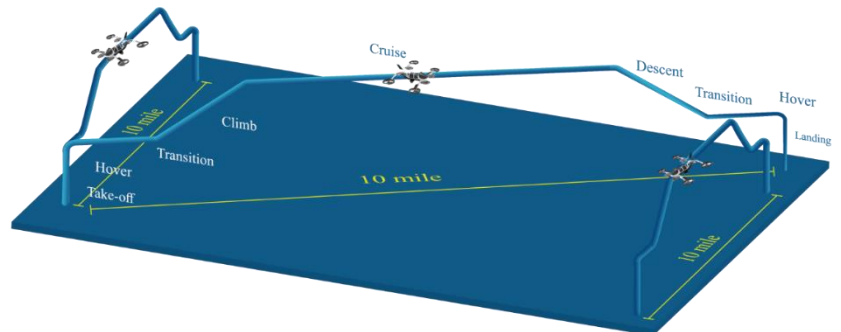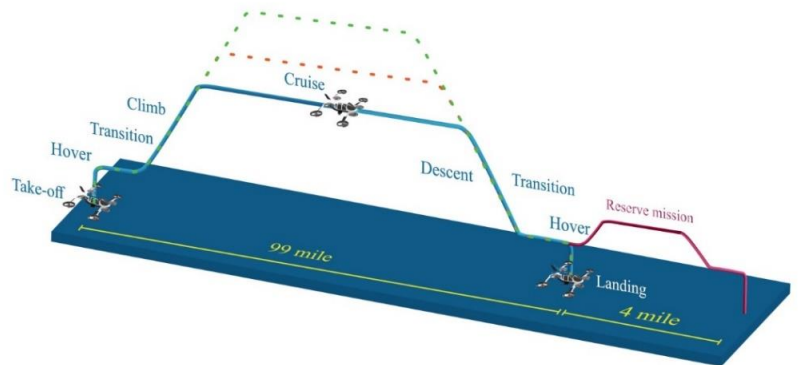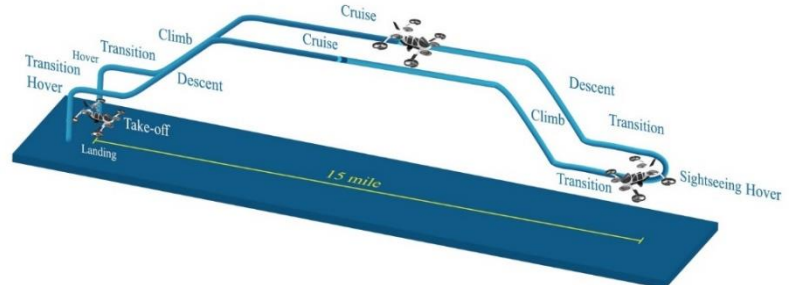

Figure 15: Sightseeing mission

Table 5: Common and reserve mission properties

Common Mission		Reserve Mission	
Take-off altitude	50[ft.]	**Reserve mission climb time duration**	60[sec.]
Take-off time duration	5[sec.]	**Reserve mission climb rate**	1000 fpm
Hover time duration	85[sec.]	**Cruise speed**	164mph
Transition time duration	10[sec.]	**Reserve mission descent time duration**	60[sec.]
Transition distance traversed	434[ft.]	**Reserve mission descent rate**	1000 fpm
Climb rate	1000 fpm	**Hover time duration**	85[sec.]
Climb time duration	87[sec.]	**Landing altitude**	50[ft.]
Cruise speed	164 mph	**Landing time duration**	5[sec.]
Cruise altitude	1500[ft.], 2500[ft.], 3500[ft.]		
Descent rate	-1000fpm		
Descent time duration	87[sec.]		
Landing altitude	50[ft.]		
Landing time duration	5[sec.]		

8. ShadX Conceptual Design Considerations

8.1. Introduction

In general, aircraft design process starts with "Weight Estimation" followed by the so called "Performance Sizing" [5]. However wide variety of concepts available for E-VTOLs do not necessarily begin with estimating aircraft weight, we at ShadX decided to study all E-VTOL classes and further to narrow those down to what seemed to best fit the RFP requirements. This is described in the following section.

Based on how the lifting force is primarily generated during cruise, VTOL aircrafts can be divided into different categories. The first category includes those which utilize wing to balance their payload weight and includes the following configurations:

- Conventional 2) Tandem Wing or Canard 3) Three surface 4) Joined wing 5) Blended Wing Body (BWB)

And the second category includes those which use only rotors to produce the necessary lift to conduct their mission.

There is of course a different distinguishing feature about how the transition phase from vertical to the horizontal is completed. That latter is summarized into three main groups similar to that presented in [16]:

- Lift + Cruise: Where hover and cruise propulsion systems are installed separately.
- Lift = Cruise: Where same propulsion system is used for both hover and cruise including: tilt rotor and tilt wing
- Lift + Lift/Cruise: Where the cruise propulsion system is used in hover phase and supplemented by additional lift generating propulsion system

Once all categories are studied and their pros and cons with respect to the RFP requirements are understood, we can prepare a decision matrix (Table 7) we are ready to introduce are potential alternatives to meet the RFP.
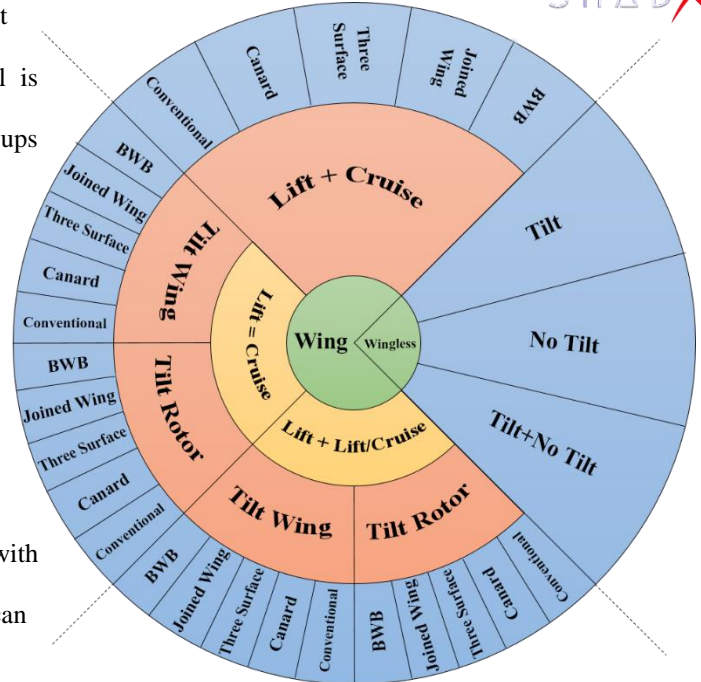
Figure 16: Alternatives classification

Obviously, we need to categorically sort our objectives as mandated by the RFP, in case they come into conflict. This is done with the help of some scoring factor based on ShadX team members' BODI[1] architecture. The result is shown in Table 11. It is emphasized that the general configuration presented in Table 7 are just preliminary and just for scoring purposes.

With decision matrix of Table 7, we are able to select promising alternatives that are in-line with RFP mandates; as well as other important requirements such as passenger comfort during boarding and egress, ground handling, ground operation and power consumption and efficiency. We also have studied "Tilt Wing" concept and came to the conclusion that its complexities are not justified for civil applications; especially when it comes to inspections for control system reliability. With Table 7 the first five configurations were selected for sizing process the most promising one is selected for further refinement and detailed computations.

8.2. Initial Sizing of Promising Alternatives

With the decision matrix we limit the number of alternatives for initial sizing to FIVE cases. Now it is the role of "Initial Sizing" to further limit the number of alternatives to ONE. "Preliminary Sizing", is in fact a process during

---

[1] Belief/Obligations/Desires/Intentions (BODI)

which quantitative measures help us compare different alternatives that had already past "qualitative measures". We find this as a sound approach to finalize ShadX configuration.

The "initial sizing" is based on the "Energy Method" that assumes the weight of the ShadX batteries is simply equal to the energy consumed during its mission divided by the battery power density itself. Although this method is not precise as it does not account for other batteries characteristics; nonetheless, it is fast and provides the opportunity to examine different configurations. Here, the relative performance of each alternative is the goal. A much accurate method is then employed later that is more useful for preliminary sizing. Following subsections provides the details.

8.2.1. Weight Estimation

We have estimated the weights of each alternatives using "weight sizing techniques" [15]. Weight's fraction of wing, fuselage, tail, landing gear, edges, and nacelles have been estimated based on data provided by [15]. Whenever needed, minor modifications have been made due to the available data based on any particular feature of each alternative (Table 6). For example, modifications due to the use of Composite materials are based on [15].

Batteries weight have been estimated as a function of aircraft take-off weight and the energy needed for each mission leg. Further to this, propulsion system components weight is then estimated that consider motors, passengers, pilot and baggage weights mandated by the RFP.

Table 6: Structural weight percentage
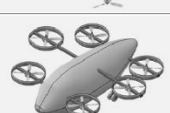
	Alternate #1	Alternate #2	Alternate #3	Alternate #4	Alternate #5
Percent of W_{st}	16.98%	19.10%	21.23%	23.25%	21.90%

8.2.2. Batteries and Motors Considerations

Noting that electric motors have wide variety of usage in different fields of the transportations; such as large trains, ships, and submarines; it would seem logical to select those motors for Spricho which are in agreement with other modes of transportations. Obviously, for Spricho, the total mass of motor is of great importance. An increase in motor weight leads to an increase in required power thereby increasing energy consumption. Based on our research, currently, it is possible to produce electric motors with a specific mass between 5 to 7 kW/kg [17]; while future developments could possibly increase this value up to 10 kW/kg. For initial sizing alternatives we have decided to use EMRAX e-motor's data [18]with some scaling factor that makes us certain to achieve the specific mass of 7 kW/kg.

Table 7: Decision matrix for alternatives E-VTOL

	Alternatives		Structural integrity	Energy Consumption	Motor location noise and inspection	ride quality/ handling Quality	ease of board and egress	Visually Appealing	complexity	Final Score
			15	25	15	15	20	20	20	
1		Lift+Cruise Joined Wing	3	3	5	3	3	3	3	420
2		Lift+Cruise Blended Wing Body	3	5	1	3	1	5	3	410
3		Lift+Cruise Conventional	3	3	3	3	3	1	5	390
4		Lift=Cruise Tilt Rotor Canard	3	3	3	1	3	3	3	360
5		Lift/Lift+Cruise Tilt Rotor Canard	3	3	3	1	3	3	3	360
6		Lift+Cruise Canard	5	1	1	3	3	3	3	340
7		Lift/Lift+Cruise Tilt Rotor Triple Surface	3	3	3	1	1	3	3	320
8		Lift+Cruise Joined Wing	3	1	3	3	3	3	3	340
9		Lift=Cruise Tilt Rotor Triple Surface	3	3	3	1	3	3	1	320
10		Wingless No Tilt	3	1	1	5	3	1	3	300

	Alternatives		Structural integrity	Energy Consumption	Motor location noise and inspection	ride quality/ handling Quality	ease of board and egress	Visually Appealing	complexity	Final Score
			15	25	15	15	20	20	20	
11		Wingless Tilt + No Tilt	3	1	1	5	3	1	3	300
12		Lift/Lift+Cruise Tilt Wing Canard	3	3	1	1	3	3	1	290
13		Lift+Cruise Conventional	3	1	1	3	3	1	3	270
14		Lift/Lift+Cruise Tilt Rotor Conventional	1	1	3	1	3	3	3	280
15		Wingless Tilt	3	1	1	5	3	1	1	260
16		Lift/Lift+Cruise Tilt Rotor Belended Wing Body	1	3	1	1	1	5	1	260
17		Lift=Cruise Tilt Wing Canard	3	1	1	1	3	3	1	240
18		Lift/Lift+Cruise Tilt Wing Conventional	3	1	1	1	3	1	1	200
19		Lift/Lift+Cruise Tilt Wing Canard	3	1	1	1	1	3	1	200
20		Lift=Cruise Tilt Wing Triple Surface	3	1	1	1	1	3	1	200
21		Lift/Lift+Cruise Tilt Wing Canard, 3 motors in canard	3	1	1	1	1	1	1	160

Moreover, minimizing energy consumption as one of the RFP's requirements is directly proportional to the value of L/D. therefore, this values of cl max and l/d for each of alternatives are estimated . Moreover, the value of CD_0 is calculated via the class I [15] method. These values are summarized in Table 8.

Table 8: Aerodynamic characteristics of alternatives

Alternatives	CD0	CL-max	(L/D)$_{max}$
No.1	0.032	2.4	18.9
No.2	0.037	2.5	25
No.3	0.033	1.8	13.5
No.4	0.033	1.8	13.5
No.5	0.033	1.8	13.5

8.2.3. Design Target Technology

To be able to compare the alternatives, we first need to select some performance measures such as maximum Rate of climb, maximum forward speed. This allows us to compare each alternative with that of both a rotorcraft and a fixed-wing configurations through parameters such as (1) Installed power, (2) weight, and finally (3) Operating (or total) cost.

Table 9: Design Point of alternatives on matching diagram

E-VTOL Alternative	No.1	No.2	No.3	No.4	No.5
W/S [lb/ft^2]	11.67	7.49	8.60	12.08	11.83
$W/P_{rotorcraft}$ [lb/hp]	5.26	5.59	5.26	5.26	5.42
$W/P_{fixed-wing}$ [lb/hp]	13.80	14.30	12.16	8.71	8.55

* Note: for all alternatives the disk loading after several iterations and tradeoff between disk rotor area and required power, is selected to be 20.48 [lb./ft^2].

Further to account for the UAM concept, a rough estimation has been made which gives the distance traversed during the transition phase. For this estimation, we assume that the power provided by "Hover Rotors" reduce as the forward speed of the aircraft increases. Once, "Hover Rotors" are finally shut-down, the "Tilting Rotors" have completed their tilt and provide the necessary forward thrust for cruising flight. At this phase, the aircraft forward acceleration is controlled while "Tilting Rotors" are at cruise condition rotating with a fixed rotational speed (Figure 61).

8.2.4. Control Policy for Selected Alternatives

Different scenarios studied by ShadX reveals that regardless of the configuration, the devised control system for ShadX must be robust and provide enough stability as well as controllability throughout the flight envelope. Here, Wing loading as a measure of the aircraft "ride quality" becomes very important; especially during One-Engine

Inoperative (OEI). Fortunately, Center of Gravity (CG) travel during flight is not a major concern and it would not increase the level of complexities involved.

In following section, the merits and drawback associated with each alternative is summarized in Table 10.

Table 10: comparing controlability of 5 alternatives

	Merits	Drawbacks
Alternative No.1	Wide-spread potential options for the placement of control surfaces	Unacceptable short period oscillation and high amplitudes of the Phugoid dynamic mode [9]
Alternative No.2	Simple stability analysis in transition and cruise mode, Better performance at hover in case of motor failure due to lower W/S	
Alternative No.3	Simple stability analysis in cruise mode, High values of wing loading (hence better ride quality)	Large vertical stabilizer due to cruise motors being too far away from CG
Alternative No.4	Attitude of the aircraft can be controlled by the means of blade pitch angle or motor RPM change during hover	
Alternative No.5	Better controllability in OEI case (in hover mode) compared to alternative No.4	Longer to throttle the rotors, due to the distance of the motors from fuselage [13]

8.2.5. Cost Consideration

For ShadX, we have modified a method for cost calculating based on Roskam and Eastlake[reference]. It is well explained in [20].

We have also computed the so called "Life-Cycle Cost" estimation for comparison between configurations. Life-Cycle Estimation is based on the following sequence :
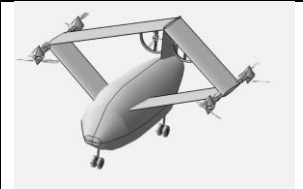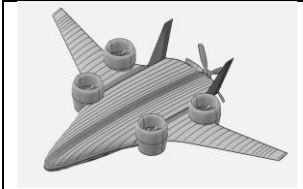
- 5 years of operation considering operating cost with loan repayment

- 7 years of operation considering operation cost without loan repayment.

- 8 years of operation considering autonomous flight

These steps are elaborated in [20].

8.3. Conclusion and accepted Configuration

The outcome of the implemented initial sizing for selected classes is summarized in Table 11.

Table 11: Result of initial Result of initial sizing of 5 selected

No.	1	2	3	4	5
$W_{battery}$	564 lb.	617 lb.	707 lb.	657 lb.	648 lb.
W_{motor}	286 lb.	354 lb.	286 lb.	275 lb.	275 lb.
Power installed	728 hp.	725 hp.	838 hp.	566 hp.	544 hp.
$D_{transition}$	1026 ft.	2309 ft.	1338 ft.	820 ft.	662 ft.
Span	31 ft.	39 ft.	37 ft.	31 ft.	31 ft.
Unit cost	353 k$	328 k$	297 k$	320 k$	317 k$
LFC	6.487 M$	6.619 M$	6.679 M$	6.610 M$	6.576 M$

The chosen class is selected based on design objectives. Mentioned parameters in Table 11 are representatives of design objectives.

$W_{battery}$ speaks for energy consumption. W_{motor} is a measure of installed power although the amount of installed power is presented as well. UAM concept is addressed via $D_{transition}$ and span of the aircraft as transition distance is limited when operating in urban area due to required clearance from nearby obstruction. In addition, the longer the span of the aircraft, the more space is required for take-off and landing. Moreover, unit and life cycle costs are given as indication of marketability.

Although No.1 is the best candidate in energy consumption and life cycle cost, as will be discussed in section 10.3.1, the limiting factor is battery sizing in the installed power. Hence, the No.5 is superior in both in energy consumption and installed power. Moreover, No.5 offers the least transition distance and span length making it the perfect choice for urban operations. In conclusion, No.5 class has been chosen and carried through the preliminary sizing.

9. Aerodynamic Verification

In this section, substantial aerodynamic characteristics and performance for different mission segments and requirements are discussed and analyzed.

9.1. Wing Design

The wing planform design process for Spricho is somewhat different from a conventional aircraft; the VTOL capability and transition sequence demand a rapid lift generation at low angles of attack and speeds even lower than stall speed to reduce energy consumption. Moreover, the novelty of our configuration as a tandem-wing aircraft, utilizing two functionally different sets of motors, alters the general wing design strategy.

On the other hand, a tandem-wing configuration tends to reduce the induced drag; this advantage becomes significant when the wings have the same planform, span, and aspect ratio with proper spacing [25], [26]. Hence, the aft and fore wings are designed similarly, which also helps reduce the manufacturing cost.

9.1.1. Wing Overall Planform

The motors are placed at the tip and root of the wings. A part of the wing root acts as a stand for the hover motors and thus does not generate lift; resulting in a smaller effective wing area. Besides, Spricho flies at Mach numbers lower than 0.3; rendering air compressibility negligible and a sweep angle unjustifiable. The wing geometric parameters are specified in Table 12.
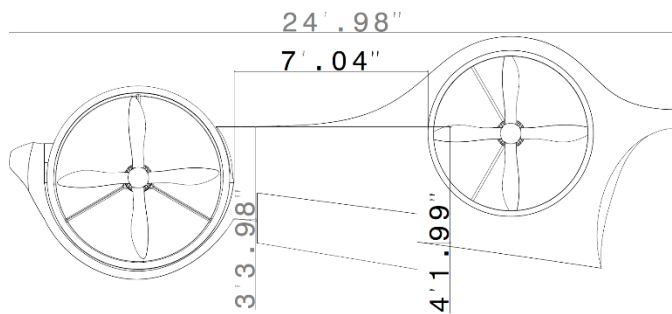

Figure 17: Wing Geometry

Table 12: wing specification

Parameters	Number	Parameters	Number
Area [ft^2]	88.2	AR	4.5
Root chord [ft.]	5.21	λ	0.7
Tip chord [ft.]	3.65	Span [ft]	19.92
$\Lambda_{\frac{c}{4}}$ [deg.]	0	MGC [ft]	4.47

It is noted that the wing span and AR determined above, are for an isolated wing.

Spricho has no high lift devices, primarily due to the selected airfoil being able to solely provide the required lift and the VTOL capability of the aircraft which eliminates the segments of flight envelope where high lift devices are usually used.

As will be mentioned in section 9.4, $\left(\frac{L}{D}\right)_{max}$ in cruise occurs at AOA= 2.3°. Therefore, to avoid a constant

need to reach high angles of attack to achieve aerodynamic efficiency, the wing incidence angle is selected to be 2°,

instead. Furthermore, twist angle is decided to be 0°, as the wing tip-located motors surmount the tip stall problem. In

addition, the aircraft reaches high values of lift coefficient, so there is no need to fly at high angles of attack.

9.1.2. **Wing-Fuselage Arrangement**

In a tandem-wing aircraft, the gap between the fore and aft wings $\left(\frac{h}{b}\right)$, defined as the vertical gap between two

wings, divided by the wing span, becomes important as it strongly affects the induced drag (due to fore-wing's

downwash) [25], [26]. In Spricho this gap is 0.21 and induced drag is about 75% of a conventional aircraft's, having

the same span and AR [25], [26]. Hence, the aft wing is located higher than the fore wing to reduce downwash effect

9.1.3. **Airfoil Selection**

As discussed earlier, it is required to consider both transition to cruise and cruise segments. Therefore, an airfoil

with high C_l and low C_d in flight speed range is required. In cruise phase, the selected airfoil should provide $C_{l_{max}} =$

1.87. The thickness ratio is not taken into consideration, as there is no need to carry fuel in them. NASA/LANGLEY

LS (1)-0417 (GA (W)-1) AIRFOIL (ls417-il) is selected, as it complies with the mentioned requirements. The airfoil

geometry and characteristics are presented in Figure 18and Table 13, respectively.

Table 13: Airfoil characteristics

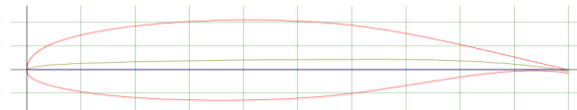| Name	LS(1)-0417 (GA(W)-1
Max Thickness	17% at 40% chord
Max Camber	2.4% at 65% chord

Figure 18: Airfoil geometry

The lift and drag coefficients variation with angle of attack are plotted in Figure 19, respectively ([27]). Reference

[27] is used to plot the trends for low speeds (at the beginning of transition; from 1.2 to 24 $\frac{mile}{hr}$) and [28] for high

speeds (starting from the end of transition through cruise; from 45 to 190 $\frac{mile}{hr}$).

9.2. Aerodynamic-based mission analysis

Spricho has two main segments of flight; hover and transition to cruise plus cruise. In each flight phase, a different

combination of propulsors is used to provide the required lift and thrust. These segments are analyzed individually in
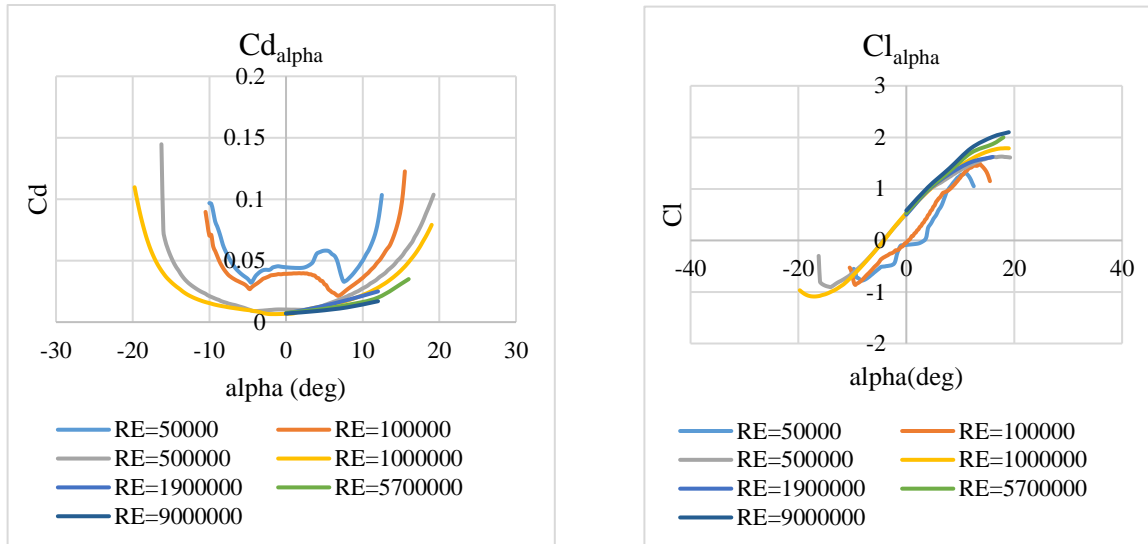
the following section.

Figure 19: right) lift coefficient left) drag coefficient vs alpha

9.2.1. **Hover and Transition to cruise**

Starting from the ground up to 50 ft. altitude is considered as the hover phase. In this flight mode, there is no lateral travel. The aerodynamic surfaces are ineffective, thus the only source to generate lift and drag are the motors. This mode does not require an extensive study. The lift and drag forces in transition mode consist of two part; lift and drag caused by aerodynamic surfaces and by thrust. Mach number changes from 0 to 0.09, so as the airfoil lift curve slope. Consequently, aircraft's lift curve slope varies from 0 to 4.16 rad^{-1} based on the method suggested by [29], which is modified by decreasing the exposed wing area (Figure 20).

In addition, C_{D0} varies with speed due to skin friction coefficient change and tilting sequence (Section 9.4). Moreover, Wing span efficiency and modified span efficiency e_x vary with the lift coefficient and flight speed in transition phase, respectively [23], [27].

9.2.2. **Cruise**

In this phase, the aerodynamic behavior can be assumed steady. Also, to reduce the drag, hover motors will be covered by means of lids, which is numerically verified in (Section 9.4).

9.3. Lift Distribution Analysis

In this section, the lift produced by aerodynamic surfaces along with the lift due to thrust is analyzed in transition and cruise. The lift curve slope and its variation with speed is shown in Figure 20.
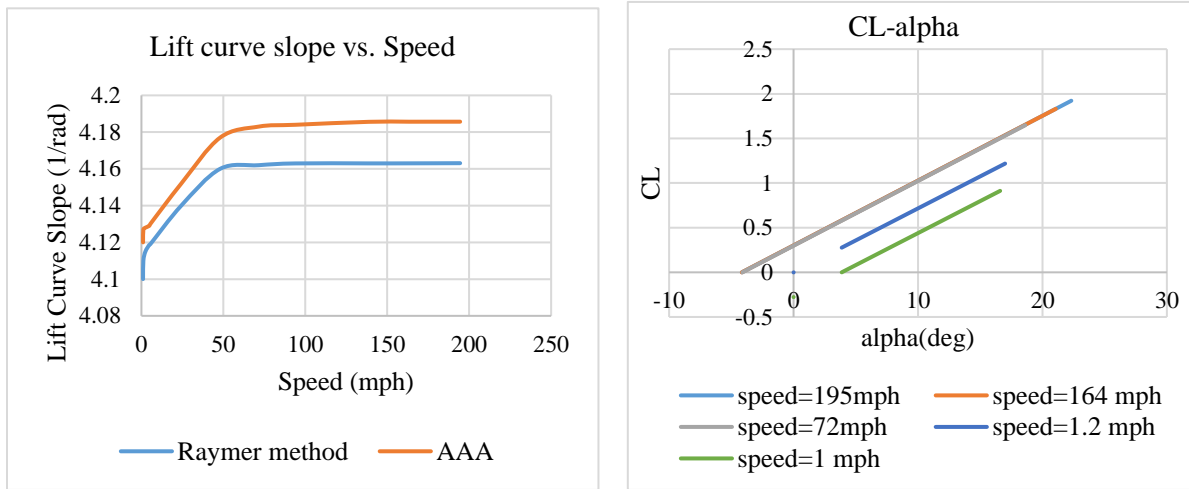

Figure 20: right) CL-alpha vs alpha, Left) Lift curve slope vs speed

Lift curve slope increases rapidly at the start of forward flight and is then slowed down near $50 \frac{mile}{hr}$. Afterwards, the aircraft's lift curve slope becomes nearly constant and reaches a value of 4.163 calculated by Raymer's method [26] and 4.186 based on AAA [28] results. $C_{l_{max}}$ increases with speed and obtains a value of 1.648 at the end of transition (speed of $71.5 \frac{mile}{hr}$) and reaches 1.83 at cruise speed ($163.5 \frac{mile}{hr}$). A value of 1.922 is achieved at the max cruise speed ($194.5 \frac{mile}{hr}$) (11).

The other source of producing lift in transition are motors. The total lift produced by motors and wings should be equal to W_{TO}. The minimum required vertical component of thrust vs. speed is shown in Figure 22. Note that the AOA in figure is the aircraft's AOA. Finally, the lift distribution of the wing is obtained by AAA, plotted in Figure 21. The effects of wing-embedded motors and fuselage is taken into account by equaling the value of lift curve slope to zero at those areas. The distribution of lift coefficient, starting from the root-located motors to half of the span, is shown in Figure 21. These values are numerically verified using CFD.
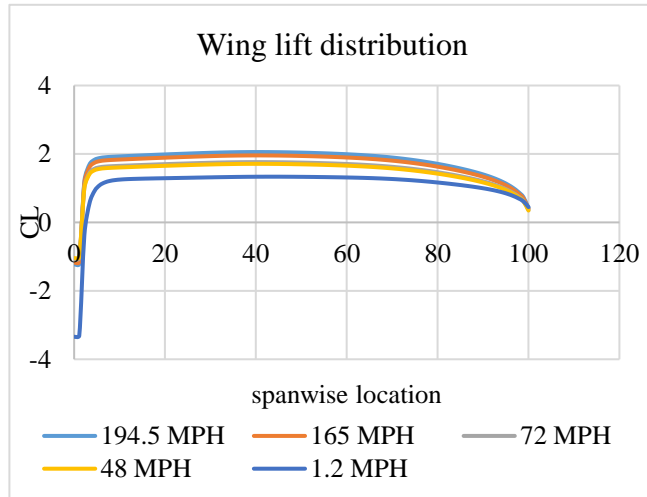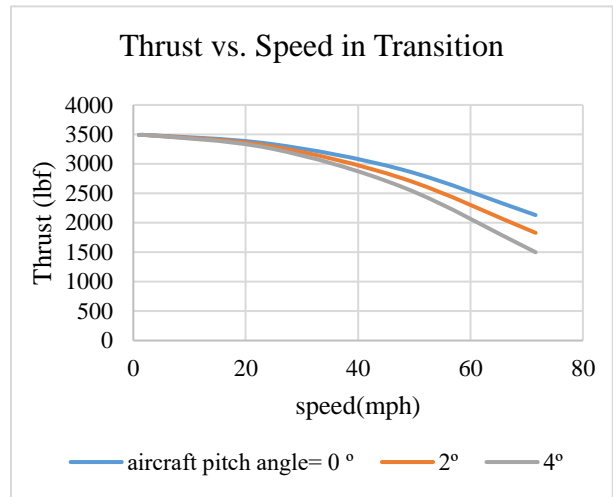
Figure 21: Wing lift distribution

Figure 22: Minimum vertical thrust-speed

9.3.1. **Aerodynamic Center Calculation**

The aerodynamic center is determined using AAA. For an isolated wing, X-location of aerodynamic center in terms of wing mean geometric chord is 0.2796 [Figure 53] at the start of forward flight, reaching the value of 0.2802 at the max cruise speed. Hence, it can be considered constant in the operating envelope. At the start of forward flight, other parts of the aircraft (i.e., fuselage, motors, and ducts) move the aerodynamic center -0.6 ft. in the X-direction. This value reaches -0.625 at the max cruise speed.

9.4. Drag Determination

In transition, aerodynamic surfaces and drag due to thrust resulting from motors are the sources of drag [32]. The aerodynamic surfaces' drag consists of zero-lift drag and induced drag. Compressibility drag is negligible, as the aircraft Mach number is less than 0.3. Zero-lift drag is calculated by component build-up method [29] and is shown in Figure 23. C_{D0} decreases as the speed increases, due to the reduction in skin friction drag. Besides, the aircraft's configuration changes with motors tilting, which affects the value of C_{D0}. Eventually, it reaches a value of 0.04355.
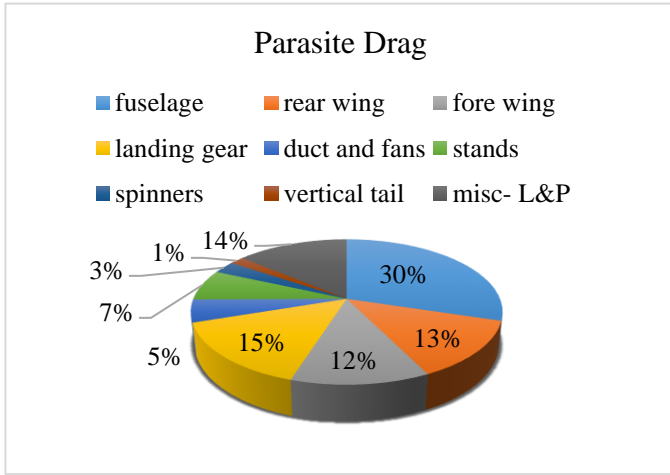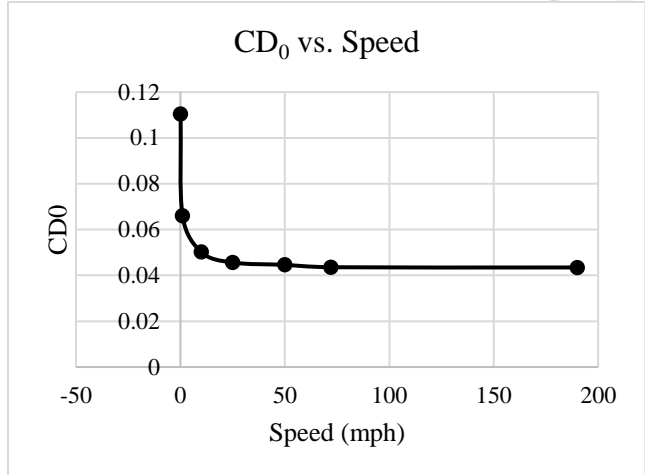
Figure 23: Component parasite drag

Figure 24: Parasite drag vs, speed

Calculation of induced drag is done based on the method suggested in [23]. For a tandem-wing airplane, modified span efficiency factor e_x can be greater than 1 [23]. During transition, this factor changes rapidly because of the changes in lift coefficient. After this phase, C_L slowly varies with speed and e_x is relatively constant at a constant AOA. The variation of e_x vs. speed is shown in Figure 26 at different AOAs. In transition, drag due to thrust is calculated by [29]. It is proportional to the thrust produced by motors in Z-direction, as shown in Figure 22. This drag is illustrated in Figure 25.
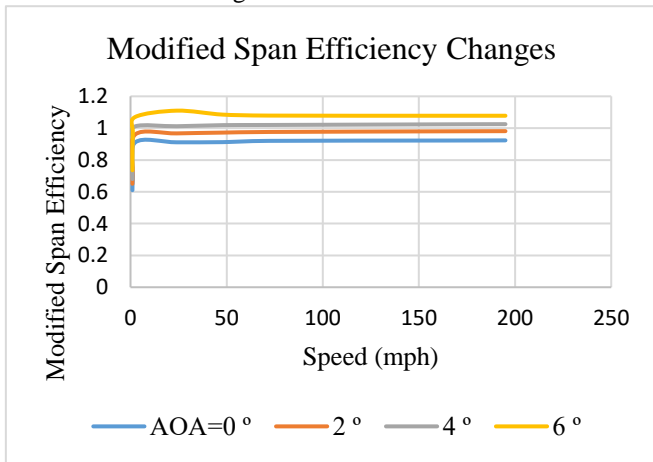

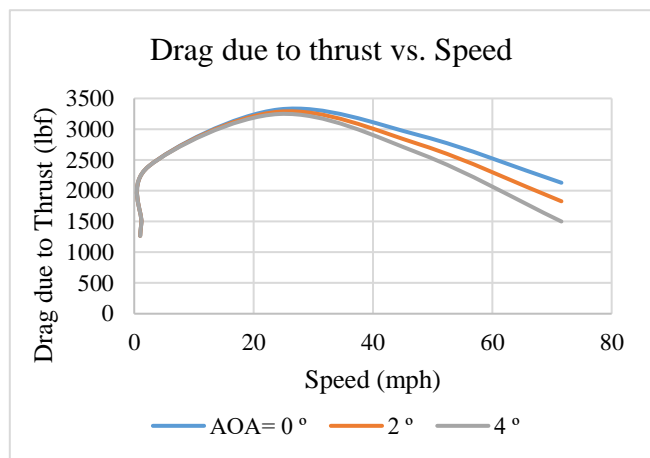Figure 26: modified span efficiency factor vs. speed

Figure 25: Drag due to thrust vs. speed

During transition, span efficiency, aerodynamic and lift due to thrust, aerodynamic, drag due to thrust, and zero-lift coefficient vary rapidly with AOA and speed. For a constant AOA, the aircraft total drag coefficient vs. lift coefficient can be drawn based on [23]. For simplicity, the effects of wingtip-located motors on induced drag is not

taken into consideration. the aircraft darg polar is plotted in Figure 28 for the selected cruise speed. The obtained $\frac{L}{D}$ is compared to a monoplane with the same wing area and AR.

As can be seen in Figure 29, the variation of L/D vs Mach number is rapid in low Mach numbers which is the case
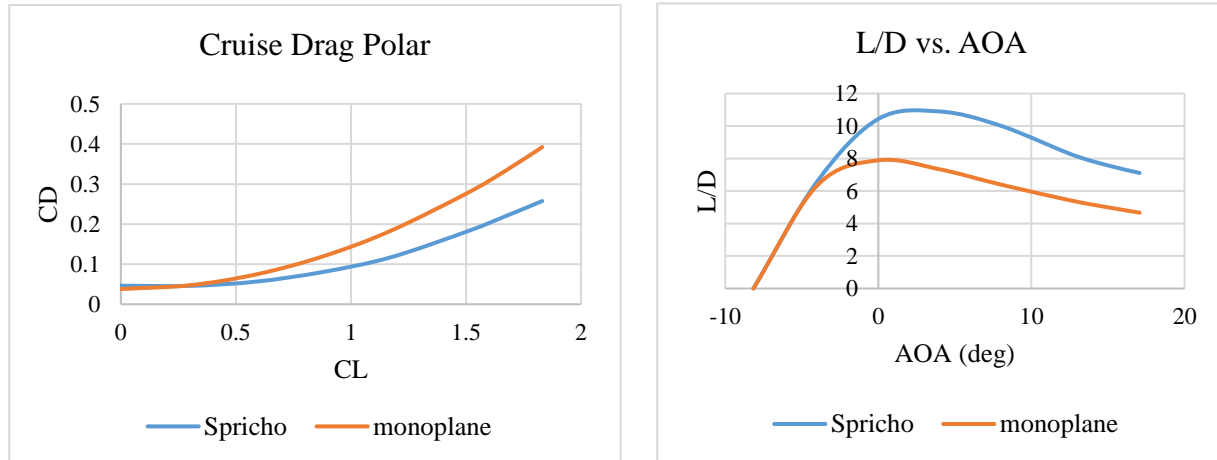

Figure 28: drag polar in cruise speed

in transition phase. However, since this phase only lasts 10, it can be neglected. Moreover, the stability is reached as explained in [13]. These variations then is slowed in higher Mach numbers and is constant at 164 mph (0.201 Mach) which is the cruising speed of Spricho.
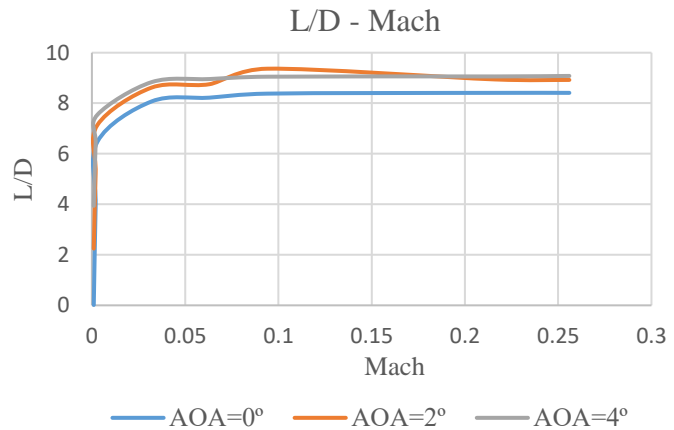

Figure 29: Aircraft L/D vs. Mach

10. Propulsion System Design & Integration

This chapter addresses different aspects of electrical propulsion system of Spricho in order to meet RFP requirements.

10.1. Propulsion System Architecture

The architecture of the electric propulsion system is shown in Figure 30 that consist of E-motors, power electronics, controller, rectifier, power transmission devices, propeller, shafts, and gears.

10.2. Electric Motor Selection and Trade Study

Performance specifications of electric propulsion system's components and batteries are selected based on

Figure 30: electric propulsion architecture

future studies and technology trends till 2028 and current electric motors. Two parameters are considered for different classes of E-motors. There is a relation between power and the required torque and the technology level of E-motors affecting their weight. Although there are motors with higher power to weight ratio, the required torque for producing enough thrust is relatively high which limits the value of power to weight ratio. These values are shown in Figure 31 and Figure 32and compared with available motors.
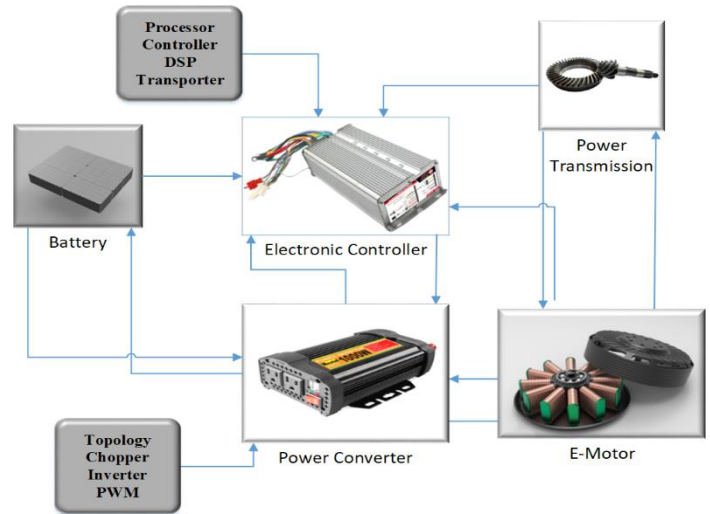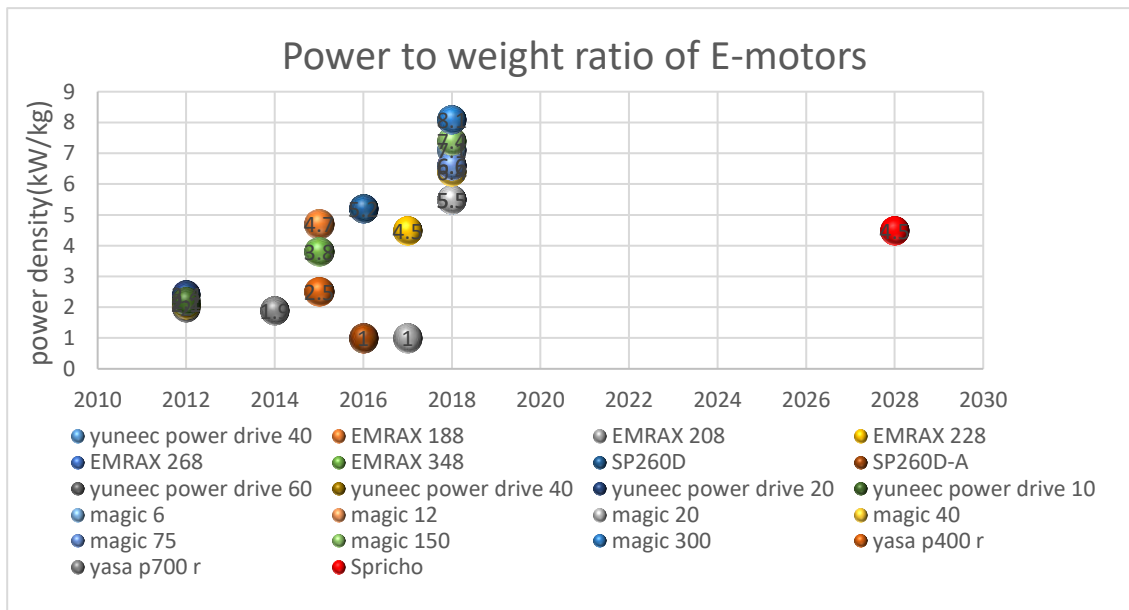

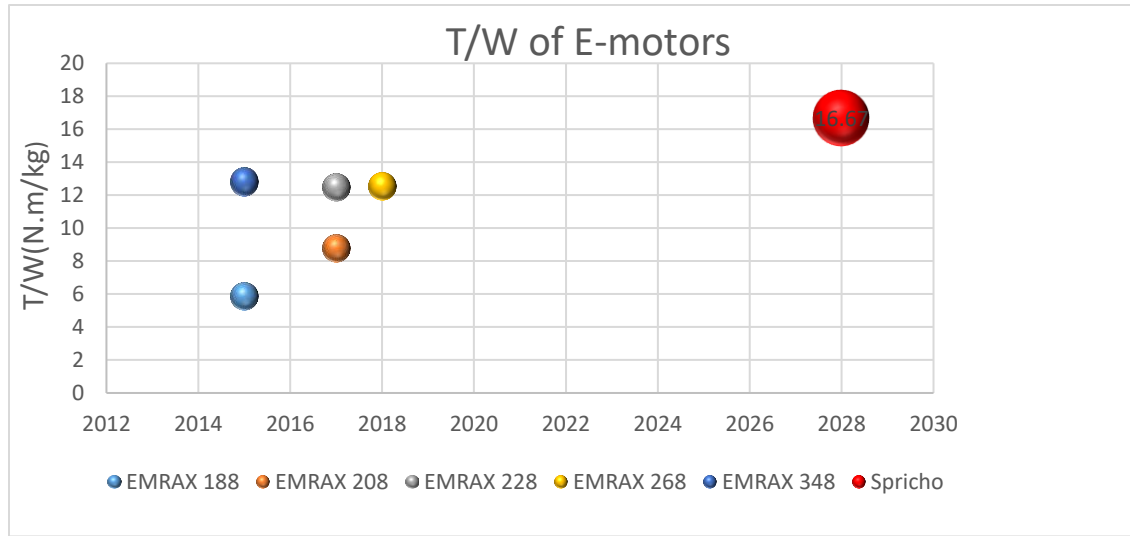*Figure 31: power to weight ratio of Spricho`s motors and other E-motors*

Figure 32: torque to weight ratio of Spricho's motors and other E-motors

10.2.1.   **Selection Method**

Disk loading and power loading are two main parameters to determine each motor's power and rotor area. These values are obtained from section 11. It is also required to consider noise level and prevent the occurrence of tip stall.

The tip speed of blades shall not exceed 140 m/s in order to meet the noise level requirement of 60 dB in urban areas [30] which is considered as one of the design constraints.

Although electric motor manufacturers claim E-motors have zero shutdown rate and the mean time between failures of synchronous motors is about 4 years and repair rate is 2 repair per year indicating a high level of reliability, [34] propulsion system is sized with two redundant motors to increase the safety of flight. Therefore, in case of failure of e-motors, Spricho is designed to be capable of continuing its operation despite the loss of one or two motors, but with a higher level of noise.

Motors are chosen based on EMRAX e-motors performance curves and adjusted 400 N.m for each motor torque. The designed electric motor's specifications are tabulated in Table 14.

Table 14: designed electric motor specifications

| Continuous power (kW)	Dry mass(kg)	Dimensions (diameter(mm)× length(mm))	Continuous Torque(N.m)	efficiency	Continuous power(kW)	Continuous power(HP)
90	24	316 × 100	400	0.95	Up to110	Up to 148
Cooling system	Temperature sensor on the stator windings	Max temperature of copper winding in the stator (°C)	Continuous motor current (Arms)	Max Motor voltage(v)	Maximal rotational speed (RPM)	Ingress protection
Air cooled	Kty 81/210	120	160	480	3000	IP21
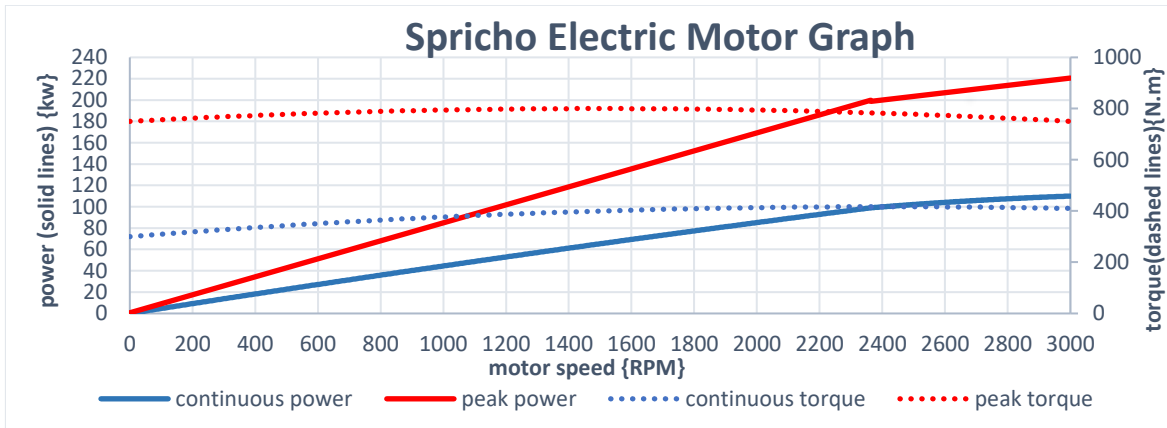
Figure 33: electric motor graph

The voltage of motors is selected based on battery packs' weight, motor controller voltage limitation, wire weight, and cross section area optimized in this voltage level.

As mentioned before, there is a relation between E-motor power output or torque×RPM and dry mass of motor, this ratio is specified according to the database and future studies which shows improvements in motors weight with same performance [35]. The cooling system used for electric motors is selected to be air cooled as they are less complex, cheaper, lighter, and easy maintenance.

Figure 34: E-motors components

10.3. Energy supply system

10.3.1.   Battery selection

According to RFP understanding, batteries are the only and main energy supply for our vehicle. There are few feasible choices for battery type which is tabulated in Table 15.

Table 15: battery types' options

Battery	Specific energy (Wh/kg) 2025	Current TRL	Projected TRL 2028
Li-Ion	250	9	9
Li-Ion with Ultrathin Li Foil Anode(Li-metal)	450	8	9
Zn-air	400-500	7	8
Li-S	500-1250	5	8

Important parameters in choosing the battery type are weight performance factors such as volumetric and gravimetric energy density and other parameters such as manufacturing cost, life cycle, safety during operation, failure modes, reliability, cost of maintenance, self-discharge rate, and operating conditions such as temperature (thermal runaway) and pressure. Here six important parameters are considered in order to choose the battery type using decision matrix method in Table 16.

Table 16 battery selection decision matrix

	Physical dimensions	Specific energy	Cycle life	Cost	Environmental issues	Thermal runaway	Final score
Priority weights	3	7	5	1	5	3	
Li-Ion	5	3	7	7	7	3	**122**
Li-metal Anode	7	7	7	3	7	5	**158**
Zn-air	7	7	5	1	3	7	**141**
Li-S	7	7	7	5	5	6	**153**

Todays, Lithium-ion based batteries have widespread usage in different electric powered systems such as electric automobiles and small aircraft due to their high energy density and resilience to different conditions as well as their low price.

Although Li-Metal anode batteries are categorized as Li-Ion based batteries such as Lithium Cobalt Oxide (LCO), Lithium Manganese Oxide (LMO), Lithium Iron Phosphate (LFP) and Lithium Nickel-Manganese-Cobalt Oxide (NMC) [17], revolutionary enhancements in structures and performance of this type of battery has made it a suitable option to be used in our vehicle

Table 17 shows the specifications of the chosen battery. [36]

Table 17: battery cell specifications

Nominal voltage	3.8 V	Operating C Rate	3.0 C
Typical capacity (25°c)	3.4 Ah	Charge Temperature Range	0°c to 45°c
Nominal energy	13 Wh	Charge Temperature Range	-20°c to 45°c
Dimensions ($H \times W \times T$)	$66 \times 37 \times 6.35$ mm	Discharge Cut-off Voltage	3 V
Typical weight	29 g	Pulse Discharge Rate	Up to 16A (5C_Rate)

Table 18: discharge characteristics of battery

Discharge Characteristics at 25°C	0.1 C	0.5 C	1.0 C	2.0 C	3.0 C
Capacity, Ah	3.4	3.2	3.2	3.1	3.1
Capacity Retention, %	100	93	93	91	92

Energy, Wh	13.0	12.0	11.8	11.2	11.0
Gravimetric Energy Density, Wh/kg	450	415	408	386	381
Volumetric Energy Density, Wh/L	1157	1068	1050	996	979

To provide required level of current is chosen to operate at 3 C rate in mission.

10.3.1. Design limitation for battery sizing and refinement of mission

In the initial sizing section, the power supply system is designed with energy method and weight of batteries is calculate by dividing the required energy consumption by battery energy density. In detailed design, the effect of current as a limiting factor is considered as well. There is a high current demand by E-motors during hover and vertical climb segments. Providing this level of current, increases the energy capacity. It affects the charging plan of batteries by reducing the number of battery replacement between missions and increases the potential range.
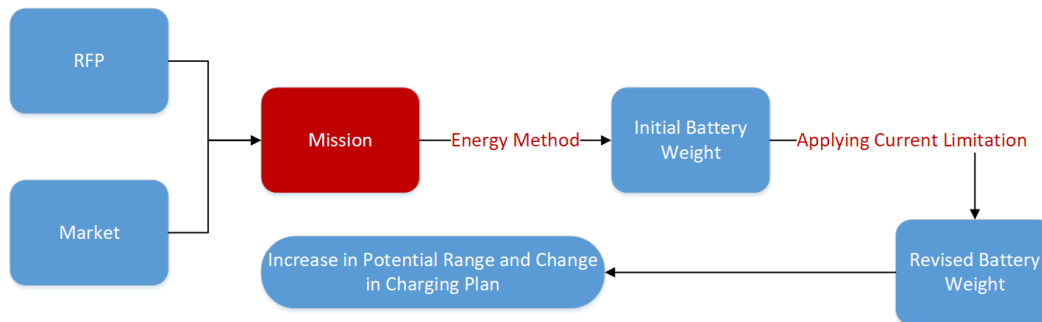
Figure 35: battery weight calculation procedure

10.3.2. Battery packaging

The entire energy supply system consists of 50 battery modules and 19110 battery cells to meet the requirements of sized mission in section 7 considering 10% of deemed energy is unavailable in every mission according to RFP.

Design parameter's limitations in order to construct the battery modules are the weight and volume of modules, for replacement and arrangement in the aircraft, and motor voltage supply, as each module is able to provide the required voltage. [37] 50 modules are paralleled to provide the required current for motors operating at maximum power.
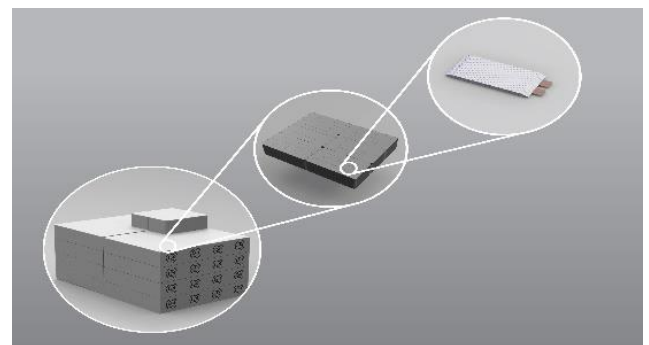

Figure 36: battery pack, module and cell

Table 19: battery modules and pack datasheet

Battery cells in series	130
Battery cells in parallel	147
Cells in one module	390
Module dimensions ($H \times W \times T$)	$37 \times 19.8 \times 12.3$ mm
Continuous motor current supply	160 Arms
Module's weight	11.3kg
Number of modules	50

10.3.3. Battery Management System (BMS)

To monitor the battery status indicated by voltage, current, temperature [38], state of charge, state of health, state of power, and so on, there is a BMS in propulsion system architecture.

10.3.4. Battery Thermal Management System

Life cycle and performance of batteries are heavily dependent on their operating temperature as it requires to stay within an allowable range.

The heat generation of battery cells depend on battery's state of charge (SOC), charging or discharged current (I) and internal electrical resistance where resistance is function of cell temperature and current is changing during mission by power output of E-motors. The performance of batteries is dependent on their operating temperature. Moreover, they are vulnerable to thermal shock. Therefore, a cooler-heater with water as working fluid is selected due to its high specific heat capacity.

10.3.5. Power Electronics, Controller and Wiring

To convert AC sinusoidal three phase current for E-motors from DC current of batteries an AC-DC pure sine wave inverter should be used with maximum Arms of 160 for each motor and voltage level should be synchronize with motor voltage therefore its operating power would be 76.8 kVA.

A variable-speed drive (VSD) is needed to be used in order to control the motor rpm. An efficiency of 97% is taken into account for sizing [39]. An IGBT based inverter is used because of large range of power support and high frequency, minimum cooling required and more reliability. Frequency range is between 0 to 5 kHz. [40]

Due to considerable number of motors and the distance of each motor from batteries, there is a vital need for an efficient wiring system to distribute energy among E-motors. In addition, to ensure safety there is two series of 3-phase selected wire and magnetic isolation to mitigate magnetic field hazards for human body considered. Wire specification is shown in Table 20.

Table 20: wiring system of Spricho

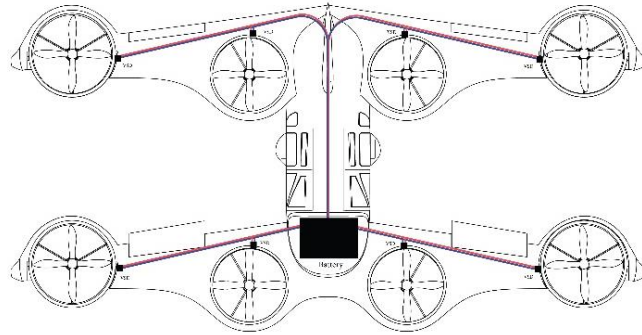| Wire type	AWG000
Max amps for power transmission	239
Cross section(circular mils)	167800
voltage	480v 3-phase
Voltage drop percentage	0.2%
Total length(m)	108
Overall efficiency	98.5%

Figure 37: Spricho Wiring architecture

10.3.6. Charging Method & Battery life cycle

According to experiments, life cycle of lithium based batteries depends on many complex parameters such as discharge profile, operating conditions, and charge algorithm. There is a trade-off between constant current-constant voltage (CC-CV) and pulse charging algorithms which affects the life cycle of battery, charging time, and cost of charging instruments. It is decided to use a combination of these two methods to

Figure 38: Battery life Cycle

provide a reasonable charging time and meanwhile being cost efficient. There is not a certain model to quantify these parameters hence, experiments on lithium-ion batteries are used to estimate the number of cycles [42]. Rapid charging in C Rate at 20°c takes up to 2 hours to fully charge the batteries. However, there is no need to fully charge them in short missions. Therefore, charging in boarding time is time saving and prolongs the battery life. Battery cycles are calculated based on battery datasheet with 125% extension of its lifecycle [9] as shown in figure.

10.4. Propeller Selection and Refinement

Disk loading and the required thrust and speed for the cruise are two parameters to determine propeller specifications. To do so, a combination of blade element theory and advanced ratio method [38] is used. A variable pitch propeller is selected due to the different characteristics of flow field in rotorcraft and fixed-wing modes and the

dependence of propeller efficiency on blade pitch angle. Moreover, in order to reduce the drag in case of failure in motors and tilting mechanism, the Spricho utilizes ducted fan motor Duct fans have more advantages than propellers in reducing propeller blade tip losses. Propellers are more efficient in producing thrust especially in fixed-wing mode. It also serves for passenger experience, safety, and noise reduction. However, using ducts make the vehicle heavier and less efficient at hover. [33]. Propeller and blades' specifications are tabulated in Table 21.

Table 21: propeller specifications

Number of blade	Blade length (inch)	Blade chord (m)	C_t of propeller	Blade max thickness(m)	Blade max pitch(in)
4	34	8	0.0382	0.02	21

11. Performance Sizing

In order to meet the mission and RFP requirements, performance sizing is done. This section acts as one the elements of the loop [section 4] with weight sizing and motor selection. Performance sizing is done for each of aircraft's modes separately. Since half of the motors used in rotorcraft mode are tilted to power the fixed-wing mode, there is a relation between power loading of these two modes. The equations and relations used in this section are derived from [43].

11.1. Constraint Diagram

The matching chart used for rotorcraft sizing is shown in Figure 39. In addition, design points of our two main rivals in order to compare our aircraft with them are shown. Hovering, Vertical Climb, and Hover Ceiling are selected as main criteria of rotorcraft mode.

Figure 39: matching chart for rotorcraft mode

Here, a tradeoff between power loading and disk loading is done to reduce the power required while the total rotor area remains in an acceptable

limit. It can be seen that the design point is placed somewhere between two of our rivals where the disk

loading is approximately the same and power loading is higher compared to Vahana. However, Cora has a better

power loading since its mission is less power consuming. It is decided that Spricho is able to complete its mission

even if two of the motors fail. Therefore, performance sizing is done based on two of motors being inoperative. Hover

ceiling is chosen based on allowed unpressurized flight (12500ft.). A summary of important data from rotorcraft sizing

is tabulated in Table 22.

Table 22: summary of rotorcraft performance

Design Point	$W/P = 5.569\ lb/HP$
	$DL = 20.48\ lb/ft^2$
Hover Ceiling Altitude	$100\ fpm\ @8500\ ft.$
Max Vertical RoC	$2100\ fpm\ @MSL$

- Note that it complies with RFP's ''Hot, High'' takeoff and hover requirement.

There are 4 motors used in fixed wing mode. Therefore, with weight known, the power loading is $8.33\ lb/HP$.

The matching chart for fixed wing mode is as shown inFigure 40.

Here, design points of some electric and non-electric airplanes are also shown in order to make our design point

comparable to other airplanes in the market. Moreover, as can be seen there are also lines for takeoff and landing

length since It is decided for Spricho to be capable of taking off and landing conventionally in order to increase its

versatility (Section 0). Since the aircraft is no different from a GA airplane in fixed wing mode, FAR23 climb

regulations are used and compliance is shown.
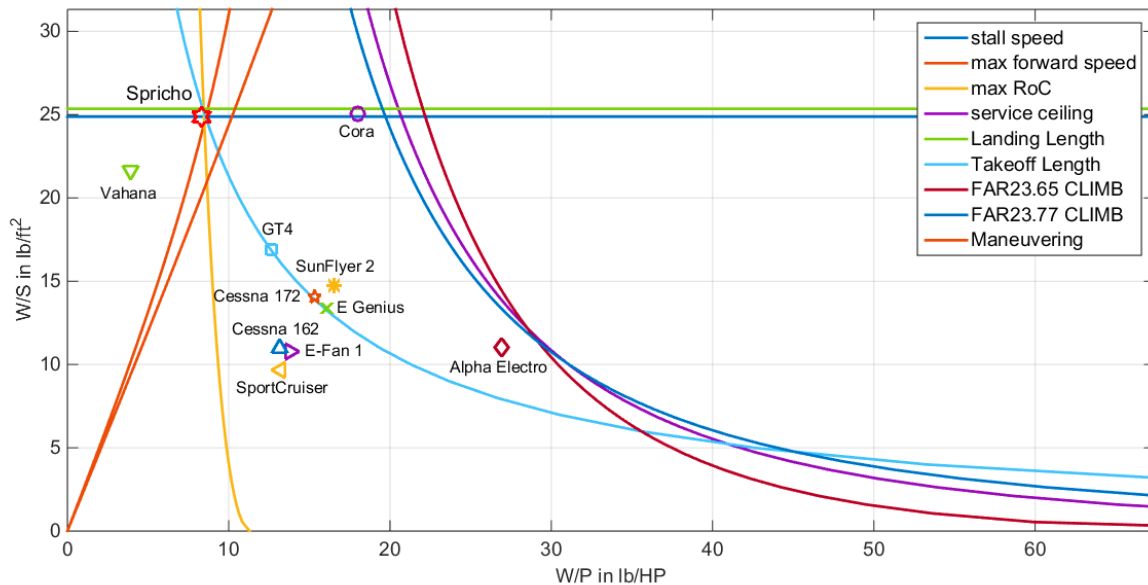
Figure 40: matching chart for fixed wing mode

As can be seen, Spricho has also a better wing loading compared to Vahana. With power loading derived from rotorcraft sizing and wing loading limited mainly by stall speed, other performance capabilities are determined. In other words, the required power is pushed toward the available power. The service ceiling is chosen to be 12500 ft. which is the maximum allowed altitude for unpressurized flights. The performance capabilities of Spricho is summarized in the Table 23.

Table 23: summary of fixed wing mode performance

Design Point	$W/P = 8.33\ lb/HP$
	$W/S = 24.88\ lb/ft\ ^2$
Stall Speed	$61\ knots$
Maximum Cruise Speed	$169 knots\ @\ 1500\ ft.$
Maximum RoC	$2460\ fpm\ @\ MSL$
Landing Length	$1900\ ft.\ @\ MSL$
Takeoff Length	$1100\ ft.\ @MSL$
Maneuvering Limit	$+3.8\ g$
Service Ceiling	$12500\ ft.$

- Note that it complies with RFP's requirement for maximum speed of at least 178 mph at 1500 ft.

11.2. Mission Optimizing

The available power of motors is selected in previous section. However, as one of the design objectives it is needed to minimize the energy consumption of each mission. In order to do this, first the behavior of energy consumption in different phases of flight is studied and the results are illustrated in this section.

A typical diagram is shown in Figure 41, as can be seen there is an optimum speed in which the least energy consumption occurs but since market forces us to have a minimum average speed of 150 mph it is not necessarily where we fly. In addition, cruising at higher altitudes requires less energy. Here, it is assumed that the range is constant in all cases.
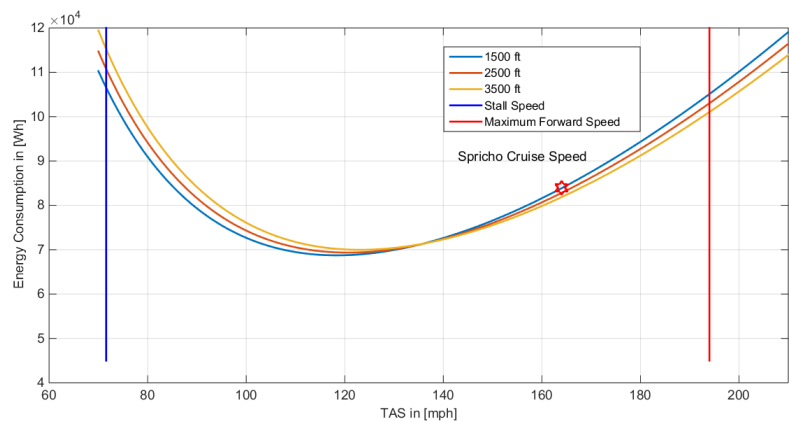
Figure 41: variation of energy consumption vs TAS for a fixed distance

Figure 42 shows that for a specific height as the vertical speed is increased both time and energy consumption to reach that height is reduced. However, vertical acceleration limits us. The vertical acceleration is determined to be $1.5 \frac{m}{s^2}$ for passenger comfort. Hence, assuming flying with constant acceleration, for each height there is a best maximum vertical speed. Which is:

Figure 42: variation of energy consumption vs vertical speed for a specific height

Equation 2 best vertical speed for a given height

$$\left(\frac{Height}{1.5}\right)^{0.5} * 1.5 = Best\ Vertical\ Speed\ in\ [\frac{m}{s}]$$

Note that its value must be lower that maximum RoC for vertical climb. For instance, for 50ft, it is 627 fpm.

However, in order to optimize the mission, it is needed to evaluate climb and cruise phase together. It is done using a MATLAB code which finds the best cruise speed, cruise altitude and rate of climb. Here, it is assumed that the minimum average speed for climb + transition + cruise is 150 mph as RFP has requested. Moreover, a minimum 5 degrees of flight path in climb is assumed [15]. As stated earlier, there are three type of mission and there is a reserve mission. The reserve mission is based on RFP and its description can be found in section 7.

Note that in all the computations of this section the required power for transition phase is assumed to be equal to hover power. This assumption is used also in initial sizing of Vahana [10].

For the typical mission of RFP, the performance details for the least energy consumption and the minimum average

Figure 43: variation of energy consumption vs ROC for three altitudes

speed of 150 mph are tabulated in Table 24.

Table 24 mission specification for typical mission

Cruise Altitude	1500 ft.
Vertical RoC & RoD	627 fpm
RoC	1000 fpm
Cruise Speed	164 mph
Rate of descend	1000 fpm
Maximum L/D	10.7

However, Spricho also operates in higher altitudes but with higher energy consumption, since in a busy airspace, it is not possible to place every airplane in one corridor (section 5).

For other missions it is assumed that the mentioned specifications result in best energy consumption as well.

In Figure 44 and Figure 45, the energy consumption and duration of each segment for each mission is illustrated. Note that following diagrams are drawn for MTOW.

A summary of duration and energy consumption of each segment for reserve and sightseeing missions are tabulated in Table 25 and Table 26.
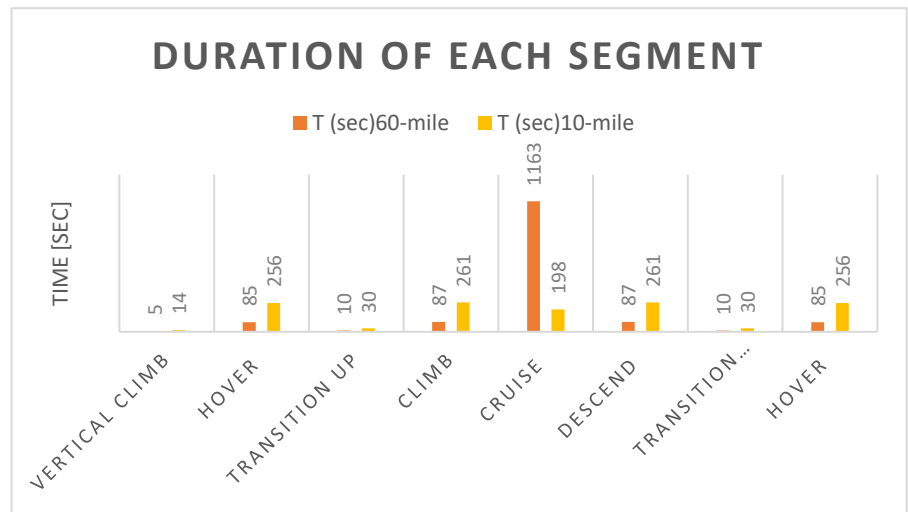
Figure 44: duration of each segment for 1 stop and 3 stop missions
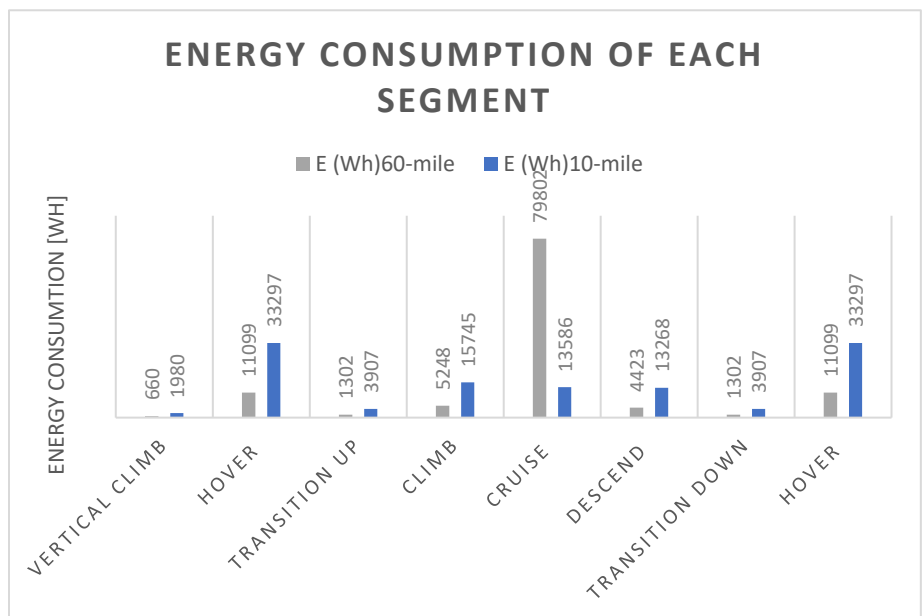
Figure 45: energy consumption of each segment for 1 stop and 3 stop missions

Table 25 duration and energy consumption of each segment for reserve mission

Reserve Mission	Transition up	Climb	Cruise	Descend	Transition Down	Hover	Vertical Descend
Time [Sec]	10	60	45	60	10	85	5
E [Wh]	1303	3620	2550	2550	1302	11071	617

Table 26 duration and energy consumption of each segment for sightseeing mission

Sightseeing Mission	Vertical Climb	Post Hover	Transition Up	Climb	Cruise	Sightseeing Hover	Descend	Transition Down	Pre Hover	Vertical Descend
Time [Sec]	5	85	20	174	342	600	174	20	85	5
E [Wh]	660	11071	2605	10497	23453	78147	8845	2605	11071	590

The mean propulsive power for each mission is tabulated in Table 27.

Table 27 mean propulsive power of each mission

Mean Propulsive Power [KW]	
Reserve Mission	404
60-Mile Mission	363
3*10 Mile Mission	441
Sightseeing Mission	478

11.3. Payload-Range Diagram

This diagram is shown in Figure 46. The variation of payload is shown continuously in order to account for deviation from standard weight breakdowns. However, the points on the curve account for where the number of passengers (pilot included) changes.
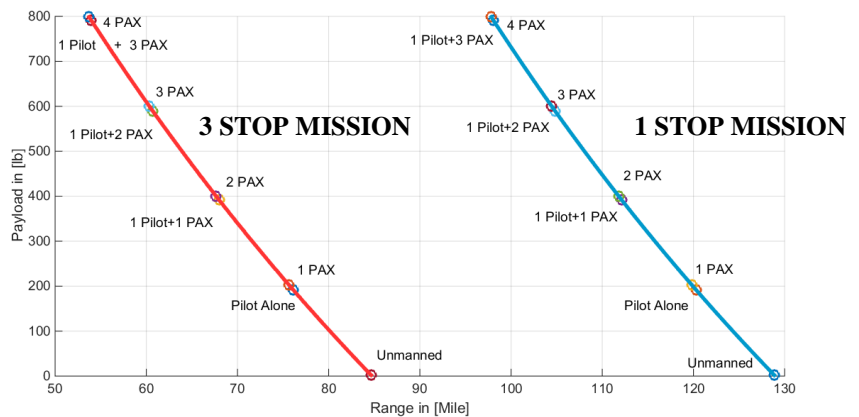
Figure 46: payload range diagram for one & three stop missions

As it can be seen there is much difference between the requested mileage and what Spricho is able to travel. It is due to extra battery needed to support the maximum required power. This issue is discussed in section 0.

For sightseeing mission payload-time diagram is shown in Figure 47. The horizontal axis shows the available time for sightseeing. It is assumed that sightseeing is done by hovering over the target area.
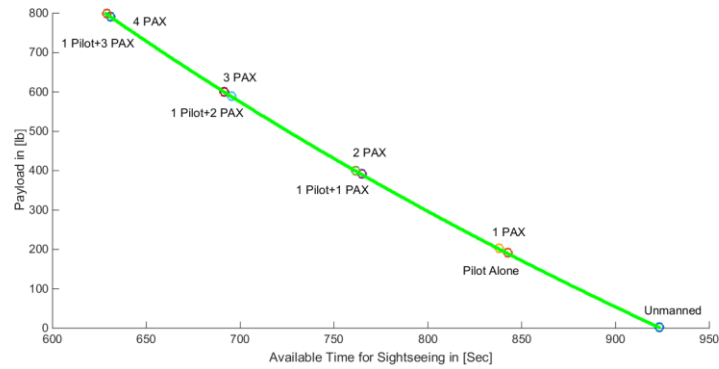
Figure 47: payload-time available for sightseeing diagram for sightseeing

11.4. Flight Envelope

The flight envelope of Spricho is shown in Figure 48. Although Spricho motors are able to operate up to 30000 ft., the red line stands for the unpressurized flight and it is set to 12500 ft. The max Q is set to 0.99 psi or 6830 Pa. (section 18). As can be seen, operation of Spricho is within allowed boundaries. Spricho cruise
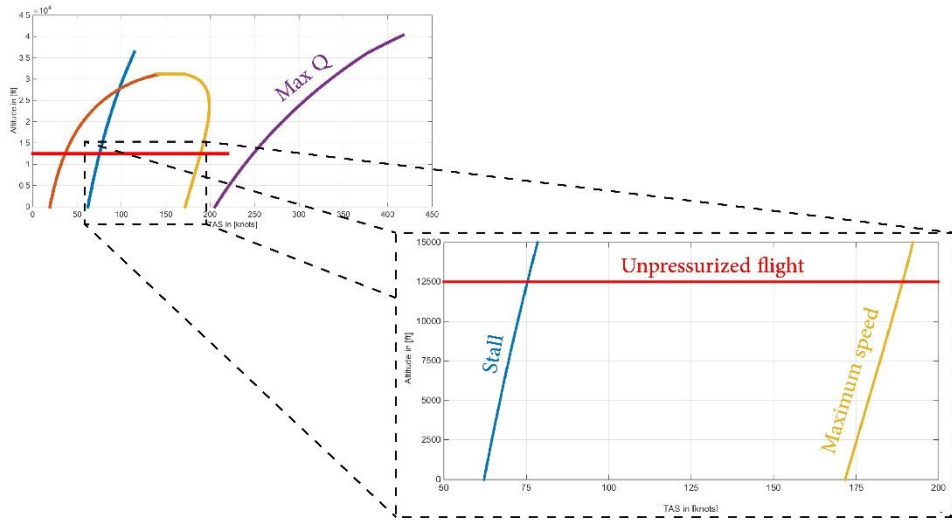
Figure 48: Flight envelope

speed is found to be 142 knots. This is away from max forward speed line since the same motors used in hover are used for fixed wing mode. However, this number is found to result in the minimum energy consumption.

12. Weight Breakdown and Weight & Balance

This section presents a detailed description of all component weights and locations in Spricho.

12.1. Weight Breakdown

In this section, more details have been considered contains subsystems, wiring, and actuators weights. In this part, weight fractions have been calculated based on [44] methods (Table 28). Weight fractions of wing, vertical tail and fuselage have been calculated based on USAF method. Landing gear has been calculated based on CESSNA method. Propeller, motors, battery, and wiring weights have been added based on section 0. Ducts weights have been calculated approximately due to its inner and covering material density (section 18). Passenger, pilot and baggage weights have been added based on RFP. Subsystems weights have been considered based on section 15.

Table 28: Aircraft Weight Breakdown & C.G. Location

Max. take-off weight 4371 [lb.]			
Max empty weight 3582 [lb.]			
Component name	Component weight[lb.]	C.G. X component[ft.]	C.G. Z component[ft.]
Structure group			
Fore wing	138.10	2.10	1.96
Aft wing	138.10	17.37	5.93
Vertical tail	25.20	15.80	10.30
fuselage	283.20	10.47	3.51
Landing gears	99.90	8.30	1.04
Paint	17.40	10.47	4.98
Propulsion group			
Front hover motor plus lid and duct	69.60	0.0	2.66
Front cruise motor plus duct	67.1	1.94	2.66
Rear hover motor plus lid and duct	69.60	16.36	6.11
Rear cruise motor plus duct	67.1	18.33	6.11
Front hover propeller	26.25	0	2.98
Front cruise propeller	26.25	1.94	2.98
Rear hover propeller	26.25	16.36	6.43
Rear cruise propeller	26.25	18.33	6.43
Energy supply group			
electric propulsive wiring system	200.00	10.39	2.96
Battery	1230	3.34	3.38
Battery cooling syst.	33.00	3.60	3.44
Battery management syst.	25.00	1.23	2.51
Passenger and pilot			
Front right passenger plus baggage	200.00	8.52	3.28
Rear passenger plus baggage	200.00	12.95	3.28
Pilot	180.00	8.52	3.28

Subsystem group			
Flight control syst.	60.00	13.85	5.19
Electrical syst.	117.1	15.33	5.11
Instrumentation	40.00	5.14	2.81
Avionic	60.00	13.87	5.19
electronics	32.0	13.86	5.19
Air condition(heater)	10.9	4.93	3.34
Air condition(cooling)	50.0	15.37	5.11
Power electronics	33.06	1.23	2.51
Cabin Interiors group			
Each Front passenger seat frame plus seat belts and cushions	20.00	8.84	2.75
Each rear passenger seat frame plus seat belts and cushions	20.00	13.27	2.75
Pilot seat frame plus seat belt and cushions	31.00	8.84	2.75
Cabin syst.	19.18	7.97	3.6
Autonomous syst.	13.2	4.93	3.34
Actuators plus bell-cranks	120.00	10.2	5.1

The major weight fractions are shown in Figure 49.
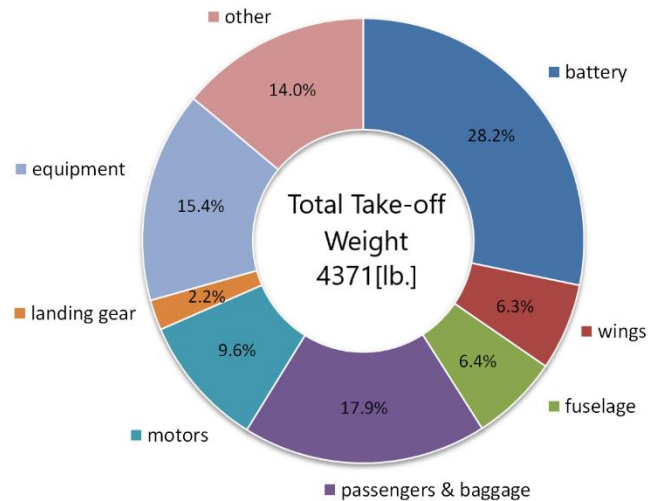
Figure 49: weight fractions

12.2. Weight & Balance

All scenarios that might happen during flight or on the ground while changing battery packs for both autonomous airplane and pilot driven airplane have been considered [15] suggests a minimum static margin of 10% for homebuilt aircraft. Moreover, a typical value of static margin for general aviation aircraft is about 15% [15]. It is up to designers to decide about the desired static margin for the aircraft at hand. Therefore, ShadX has decided to secure a level of maneuverability for the aircraft, while maintaining a static margin of at least 20% to ensure longitudinal static stability.

Table 29: SM scenarios for pilot driven

Scenarios								
Static Margin Percentage	20.9234	21.0138	25.2702	25.2702	25.5840	30.0548	25.5840	30.6390

Table 30: SM scenarios for autonomous Spricho

Scenarios								
Static Margin Percentage	31.2789	20.9367	30.6313	30.6313	25.9347	25.9347	30.0488	21.1275
Scenarios								
Static Margin Percentage	25.5882	25.5882	25.5882	25.5882	25.2748	25.2748	21.0276	21.0276

• Each black solid circle shows an onboard passenger and black solid circle with "P" sign shows the pilot. Note that black empty circle shows the vacant seat. Nose of the aircraft is left side of each scenario figure.
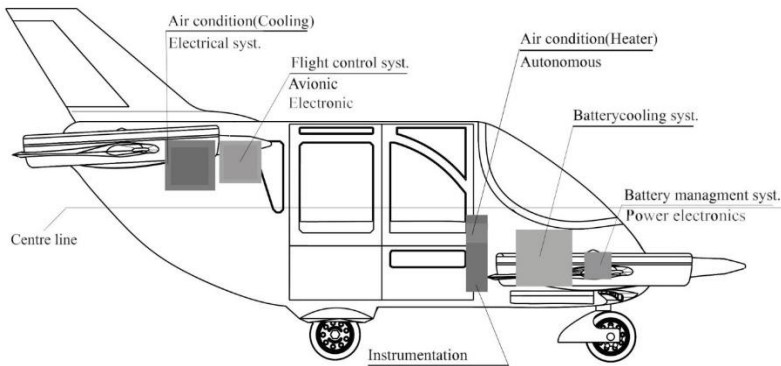

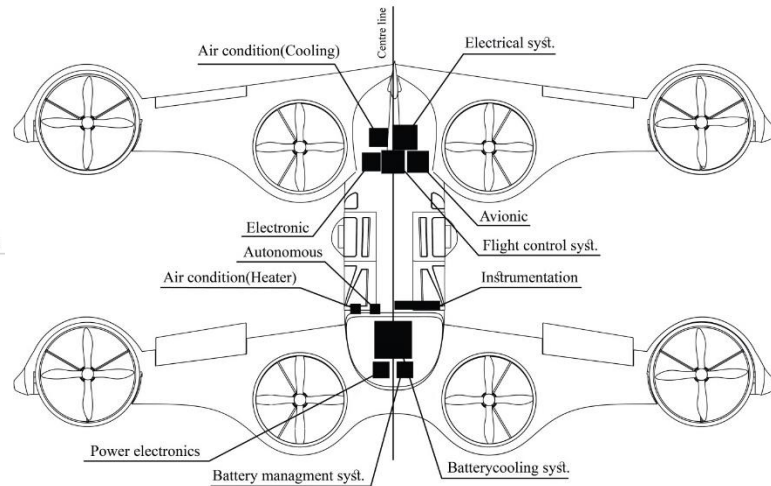*Figure 51: Spricho Systems integration- right view*

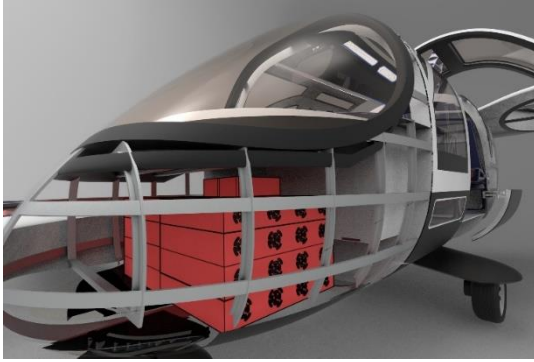*Figure 50: Spricho Systems integration- top view*
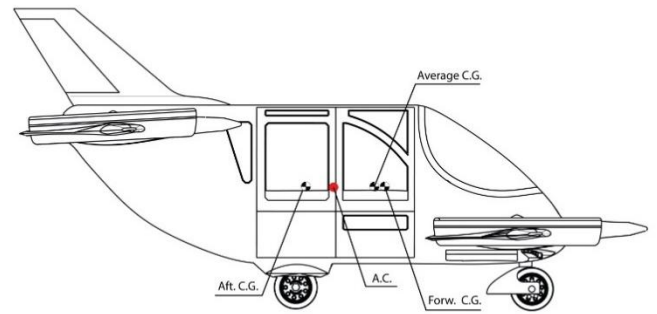
Figure 52: Battery placement

Figure 53: A.C. and C.G. locations

12.3. Landing gear

Although skids are lighter and cheaper, it is decided to utilize wheels in landing gears as it offers unique capabilities and increases the versatility of the aircraft by enabling it to take-off as a typical airplane. In addition, in case of emergency the aircraft can follow usual procedures of emergency landing. Considering weight and balance, cost estimation and aerodynamic analysis, a tricycle landing gear is selected. The benefits of using this type of landing gear includes lower weight, higher stability during ground operation, and easier ground maneuvering. Also, to mitigate the parasite drag, fairing is used (Figure 54).
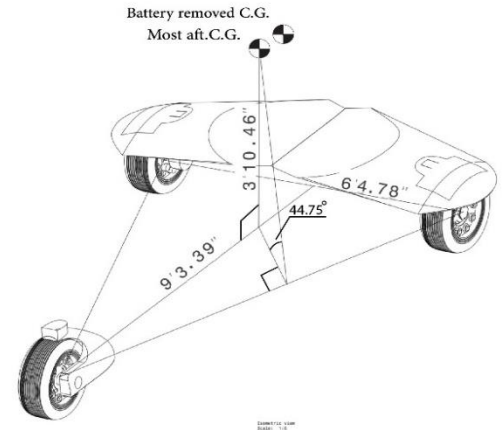

Figure 54 :Geometric angle criteria for positioning of gears

Moreover, the shorter the strut the less number of stairs is required for boarding and egress therefore, the height of strut is selected to be 1ft. As shown in Figure 54 displacement of C.G. is within the location of landing gears. Since the load is applied to all landing gears during landing all of them are designed similarly.

Rear and front landing gears are placed 10.66 ft. and 1.38 ft. aft of the aircraft nose, respectively Figure 54. The thickness of each tire is determined as shown in table R assuming each of them carries one third of the aircraft's weight. Complying with geometric angle criteria of landing gears is shown in Figure 54.

Table 31: tire specification

Tire wheel diameter	16 inch
Tire wheel width	6 inch

13. Control & Stability

S&C analysis, coupled with safety concerns and failure mode analysis, mainly depends on the final configuration and specifications of the aircraft, including the location of the CG, distance of the electric motors from that CG, location of the fore and aft wings, control surfaces moment-arms, weight properties of the aircraft, wing area, span, and etc. Initial flight condition and S&C derivatives are of importance as well. The required data from the configuration is presented in Figure 55 and summarized in Table 32 and Table 33.

In this section of the proposal, firstly, vertical tail and control surface sizing and disposition have been done, then S&C derivatives been calculated and tabulated. Next, Trimmability, ride quality, and flying handling qualities have been assessed. Finally, an extensive 6-DOF nonlinear simulation has been carried out and the results been presented and discussed.
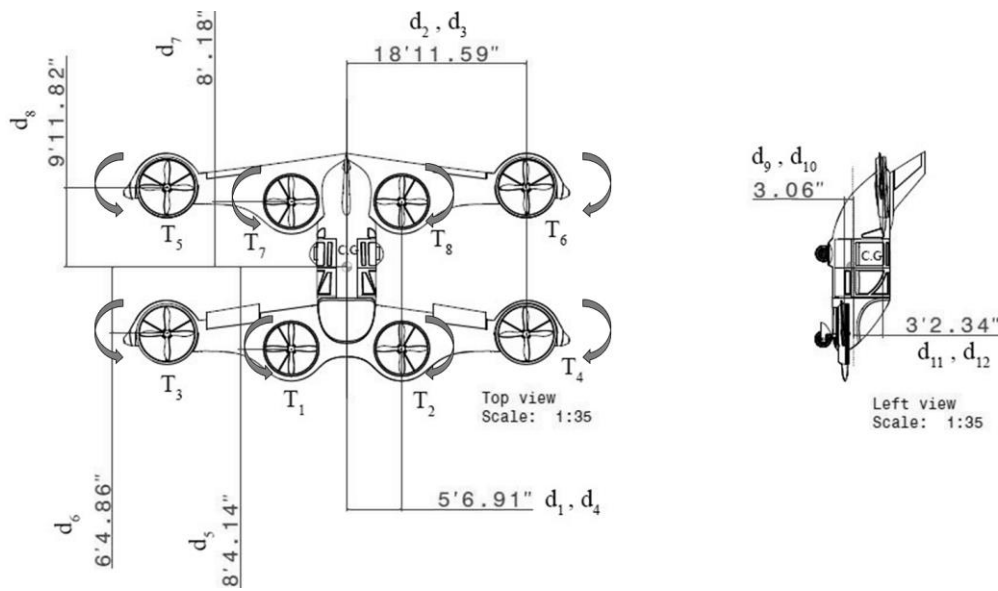

Figure 55: Required geometric parameters

Table 32: The vertical distances of motors with respect to the CG location

Scenario	Weight [lb.]	X_{CG} [ft.]	d_9 [ft]	d_{10} [ft]	d_{11} [ft]	d_{12} [ft]
3 PAX + pilot	4371	5.9547	-0.2554	-0.2554	3.1946	3.1946

Table 33: The longitudinal and lateral distances of motors with respect to the CG location

d_1 [ft]	d_2 [ft]	d_3 [ft]	d_4 [ft]	d_5 [ft]	d_6 [ft]	d_7 [ft]	d_8 [ft]
5.5762	18.9662	18.9662	5.5762	-8.3447	-6.4047	8.0153	9.9853

13.1. Empennage Design

To ensure directional stability in different flight phases and controllability in turn maneuvers and OEI case, a vertical stabilizer together with a rudder for yawing channel has been utilized in the design. As a matter of fact, limited number of cruise-motors (four) had necessitated this physic.

The vertical tail area has been determined using the methods described in [24]. First, an estimation has been made based on available air taxi and electric VTOL database, utilizing volume coefficient and vertical tail moment-arm. The calculated values are presented in Table 34.

Table 34 Estimated vertical tail area and moment-arm based on database

$\bar{V}_v$	$X_v \, [ft]$	$S_{v,initial} \, [ft^2]$	$S_{v,final} \, [ft^2]$	$\Lambda_{LE} \, [°]$	$i \, [°]$
0.032	9.09	12	15.47	45.02	0

The yawing moment coefficient due to sideslip ($c_{n\beta}$) of at least $0.0573 \, rad^{-1}$ has been recommended in [24]. So, to refine the initial estimation, directional X-plot has been plotted and assessed. Eventually, the vertical tail area has been raised to $15.47 \, ft^2$ to ensure directional stability (with 5% margin) and a level I handling quality in all flight conditions. The final directional X-plot and the dimensioned view of vertical stabilizer and rudder are presented in Figure 56 and Figure 57 respectively.
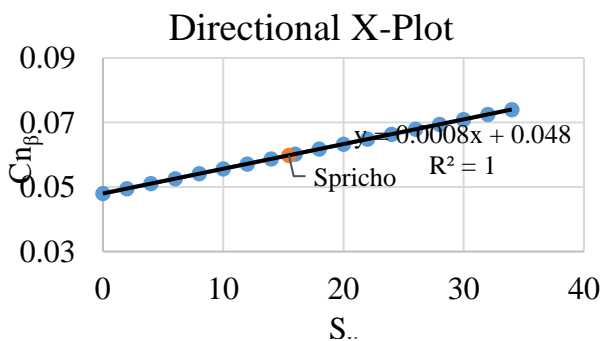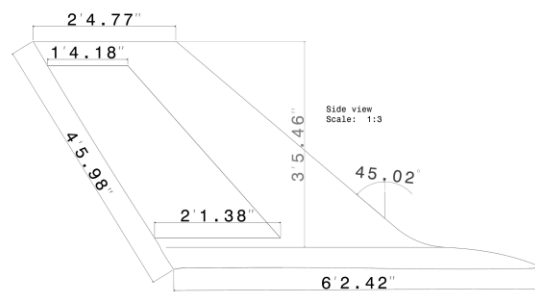

Figure 56: Directional X-plot

Figure 57: Dimensioned view of vertical stabilizer and rudder

13.2. Control Surface Sizing and Disposition

13.2.1. **Sizing Procedure**

As hover motors have been embedded inside the wings [section 10], to maintain the wing's structural integrity [reference structure], a control surface placement problem emerges. So, to address this issue, the canardvator is partly located inside the fore-wing and the remaining required surface is placed outside the wing, starting from the trailing edge. This solution enables the wing to generate more lift, as the airflow is not disturbed by the canardvator. Also, no major change in stability occurs before the plane reaches high angle of attacks [45].

Control surfaces have been sized to stabilize the aircraft in transition to cruise and cruise flight modes. Table 35 summarizes the main geometric parameters for control surfaces.

Other control surfaces, if needed, can be sized properly after wind tunnel or flight tests and can be applied to Spricho, accordingly. Figure 58 presents a dimensioned view of control surfaces of Spricho.

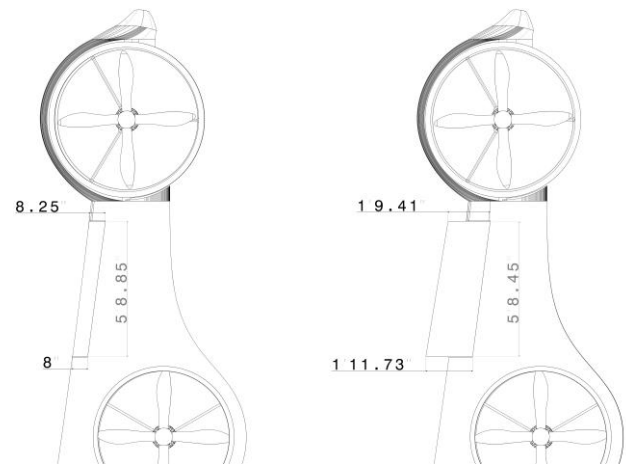*Table 35 Control surfaces geometric parameters*

Control Surface	Canardvator	Aileron	Rudder
S $[ft^2]$	16	5.2	5.79
AR	6.38	6.38	1.16
λ	0.6	0.7	0.38
Moment-arm $[ft]$	-5.15	6.44	10.25

Figure 58: Dimensioned view of control surfaces

13.2.2. **Critical Engine Out**

For sizing purposes and later nonlinear simulation, it has been assumed that the front starboard cruise motor fails during cruise. This failed motor generates a yawing moment due to the drag force, which is calculated based on [44] and [46], suggesting an additional yawing moment N_D to be modeled as the failed-motor drag induced yawing moment.

N_D is then estimated to be $0.25N_t$ for a propeller driven airplane with variable pitch propellers (thus providing feathering option), with N_t being the critical engine-out yawing moment. So, for Spricho, a rudder deflection of 0.5454 degrees is needed to negate the yawing moment of 6544 lbf. ft^2, which is well below the 25-degree limitation specified by [44]. This deflection angle has been verified in section [Simulation Results, OEI]

13.3. Stability and Control Derivatives

Stability and control derivaties in pitch, roll, and yaw channel have been calculated for transition to cruise and cruise flight conditions and are presented in Table 36. AAA software has been used for this purpose.

Table 36: Stability and control derivatives of Spricho (X_{CG}=6.0359ft.)

h [ft.]	2500	1500	50		2500	1500	50
Velocity [kts]	146	146	70		146	146	70
Phase	1	2	3	Phase	1	2	3
C_{D_0}	0.0436	0.0436	0.0436	C_{l_β}	-0.1386	-0.1386	-0.1386
C_{D_u}	0.0000	0.0000	0.0000	$C_{l_{\dot\beta}}$	0.0000	0.0000	0.0000
C_{D_α}	0.1825	0.1771	1.0470	C_{l_p}	-0.4473	-0.4473	-0.4402
$C_{D_{\dot\alpha}}$	0.0000	0.0000	0.0000	C_{l_r}	0.0666	0.0666	0.0647
C_{D_q}	0.0000	0.0000	0.0000	$C_{l_{\delta A}}$	0.1198	0.1198	0.1183
$C_{D_{\delta CV}}$	0.0036	0.0036	0.0047	$C_{l_{\delta R}}$	0.1338	0.1338	0.0195
$C_{T_{X_u}}$	-0.0685	-0.0665	-1.0768	C_{y_β}	-0.0529	-0.0529	-0.0432
C_{L_0}	0.0349	0.0349	0.0349	$C_{y_{\dot\beta}}$	0.0013	0.0013	0.0000
C_{L_u}	0.0220	0.0212	0.0168	C_{y_p}	0.0003	0.0003	0.0000
C_{L_α}	4.7041	4.7034	4.6183	C_{y_r}	0.0095	0.0095	0.0009
$C_{L_{\dot\alpha}}$	0.0013	0.0013	0.0011	$C_{y_{\delta A}}$	0.0000	0.0000	0.0000
C_{L_q}	16.7894	16.7866	15.8157	$C_{y_{\delta R}}$	2.0777	2.0780	0.4332
$C_{L_{\delta CV}}$	1.2298	1.2298	1.2170	$C_{y_{T_\beta}}$	0.0000	0.0000	0.0000
C_{m_0}	-0.0104	-0.0104	-0.0104	C_{n_β}	0.0319	0.0320	0.0208
C_{m_u}	0.0003	0.0002	0.0002	$C_{n_{\dot\beta}}$	0.0008	0.0008	0.0000
C_{m_α}	-6.7882	-6.7872	-6.4157	C_{n_p}	0.0253	-0.0253	-0.0253
$C_{m_{\dot\alpha}}$	-0.0018	-0.0018	-0.0015	C_{n_r}	-0.0075	-0.0075	0.0000
C_{m_q}	-19.4481	-19.4439	-17.4203	$C_{n_{\delta A}}$	-0.0054	-0.0054	-0.0052
$C_{m_{T_u}}$	0.0172	0.0167	0.2544	$C_{n_{\delta R}}$	-1.9161	-1.9163	-0.1668
$C_{m_{T_\alpha}}$	0.0000	0.0000	0.0000				
$C_{m_{\delta CV}}$	1.6768	1.6768	1.5620				

13.4. Trimmability Assessment in Cruise

To best do the task at hand, the flight envelope has been divided into three main flight phases; hover, transition to cruise, and cruise. First, Trimmability in cruise mode has been assessed for two different flight conditions and the

associated trim condition calculated using MATLAB. The pertinent flight conditions and required control

surface deflection are presented in Table 37 and Table 38, respectively.

Table 37: Flight condition & weight data for cruise mode

Flight Scenario	3 PAX + pilot	4 PAX w/o pilot	2 PAX + pilot	2 PAX w/o pilot	0 PAX w/o pilot
Altitude [ft.]	2500	2500	2500	2500	2500
Flight Speed [ft./s]	240.51	240.51	240.51	240.51	240.51
Weight [lbs.]	4362	4371	4171	3971	3571
I_{XX} [slug. ft^2]	6431	6430	6408	6391	6351
I_{YY} [slug. ft^2]	5126	5137	4975	4996	4836
I_{ZZ} [slug. ft^2]	10083	10099	9915	9922	9727
I_{XZ} [slug. ft^2]	1407	1407	1391	1395	1381
I_{rot} [slug. ft^2]	0.44	0.44	0.44	0.44	0.44
X_{CG} [ft.]	6.0359	6.0352	5.8190	5.8031	5.5191

I_{XY} and I_{YZ} are very close to zero and have been neglected suggested by [47]. To accurately calculate the moments

of inertia in time, an updating procedure can be implemented to take the tilting mechanism into account.

Table 38: Longitudinal Trim condition for Spricho

h [ft.]	Scenario	Weight [lb.]	X_{CG} [ft.]	α [deg]	δ_{CV} [deg]	T [lbf.]	CL_1	CD_1	CT_1
2500	3 PAX + pilot	4371	6.0359	1.7852	9.5583	1104	0.3867	0.0491	0.0491
1500	3 PAX + pilot	4371	6.0359	1.7207	9.2809	1128	0.3754	0.0487	0.0487

Here, the most aft CG location has been considered as the most critical and thus been used in these calculations.

The results indicate that the aicraft is of course trimmable in cruise, with the required canardvator deflection being

about +9.5 degrees. The total required thrust for four cruise motors is 1104 lbf, which translates into a rotational speed

of 87.35 $\frac{rad}{s}$ per motor. The behavior of aircraft in this flight phase is assessed later, in section [simulation] as the

values in Table 38 had acted as initial conditions for the 6-DOF nonlinear flight simulation.

Moreover, the trim diagram has been plotted to verify the results achieved before. The current configuration lies

well within the CG limits and verifies the AOA and δ_{CV} associated with the trim condition.

The most critical cruise scenario (most aft CG) has been considered for the sizing of canardvator [24].

The area of canardvator has then been finalized, after the simulation results had been studied. Through many iterations done to assess the feasibility of trim condition, canardvator, aileron, and rudder maximum and minimum deflection angles have been decided on.

Table 39: canardvator, aileron, and rudder deflection range

δ_r [°]	δ_{CV} [°]	δ_A [°]
±15	±10	±10
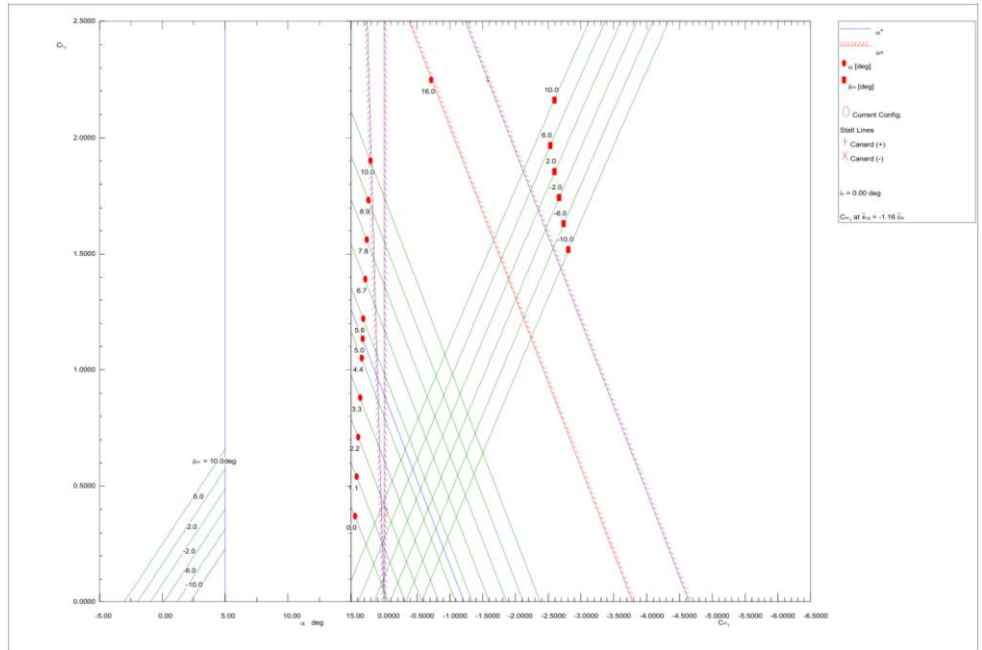
Figure 59: Trim diagram for X_CG=6.0359 ft [AAA]

13.5. Ride Quality and Passenger Experience Criteria

According to [48] and [49], the ride quality criteria are used to ensure that the controlled aircraft will provide passenger comfort to an acceptable level. A ride discomfort index J_{RD} has been proposed in [48], stating that the resulting ride shall not degrade to below the levels specified. The short-term requirement for a flight phase duration of less than 0.5 hour is that $J_{RD} \leq 0.28$. For Spricho this value is 0.26; thus, complying with the requirement.

13.6. Flight Handling Qualities (FHQ) Evaluation

Spricho can be classified as a class I aircraft based on [44]. The handling qualities have been evaluated for flight phase category B (cruise); the corresponding undamped natural frequencies and damping ratios have been calculated using AAA and the results are presented in Table 40.

Mode	Short Period	Phugoid	Spiral	Roll	Dutch Roll	Dutch Roll
Handling Quality	ζ	ζ	T_{half}	τ	ω_{n_D}	ζ_D
Level I Requirements	> 0.30	≥ 0.04	> 20 s	< 1.4 s	$> 0.4 \frac{\text{rad}}{\text{s}}$	> 0.08
Spricho	0.51	0.40	22.51	0.27	2.73	0.10

Hence, the aircraft is able to meet all of the requirements for level I.

14.   Simulation Setup

To simulate the behavior of the aircraft in flight, two steps have been taken; first, the physical system has been modeled and equations of motion derived. In this part, proper modeling of tilt-rotor dynamics, thrust vectoring
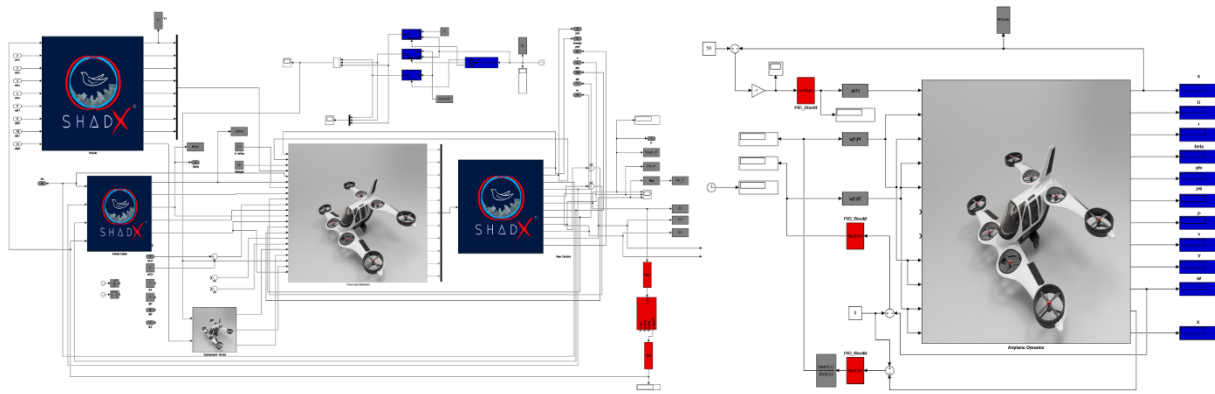
Figure 60: Schematic of nonlinear simulator

moments, and gyroscopic terms generated by motors have been the most crucial steps. Next, the general control strategy has been determined for each flight phase, to be implemented in controller design. A novel 6-DOF nonlinear simulation has been carried out using MATLAB & Simulink, to simulate the flight of Spricho in two primary flight phases; namely cruise and hover to cruise transition. With the associated flight control system that had been developed, the aircraft has thus been proven controllable during these flight modes. The simulation has indeed verified the design process and ensured a stable transition, as well. The schematic of Simulink blocks and associated designed controller (for transition to cruise) is presented in Figure 60.

14.1. Mathematical Modeling

Two different dynamics govern the flight dynamics of Spricho; Quad-rotor dynamics plus airplane-mode dynamics. As the aircraft gains forward speed, that is high enough to enable the wings to generate lift, the quad-rotor

dynamics are converted into fixed-wing dynamics. This transition sequence is presented in Figure 61. To best assess the stability and controllability of the vehicle, mathematical modeling has been done mainly based on [46] and the tilt-rotor dynamics has been modeled with the help of [50] [51] [52]. ShadX utilized a component build-up method, in order to incorporate the two aforementioned dynamics together. To model the generated thrust by the motors, equation 3.11 of [53] has been used.

There exist a number of considerations regarding the mathematical modeling, and further flight simulation:

- [51], [52], and [54] suggest a tilt-angle rotational rate of 10, 40, and 15 degrees per second, respectively. For Spricho, tilt-angle rotational rate has been initially assumed to be 9 degrees per second and later validated by the simulation results. For future work, to avoid rapid changes in state variables' behavior in time, a quadratic distribution can be used instead.

- Maximum permittable rotational speed for the rotors are 3000 RPM ($314.16 \frac{\text{rad}}{\text{s}}$).

- The thrust-lines of aft cruise motors (5 and 6) are higher relative to CG, thus generating negative pitching moment. On the contrary, the fore motors (3 and 4) are lower and produce positive pitching moment.

14.2. General Control Strategy

The general control strategy for the proposed design is to achieve the desired force and moment commands and also, minimize deviations from the trim condition; this in return helps increase the passenger experience during flight. Use of electric motors enable the designer to use motors RPMs as control inputs, due to the fast command response speeds of the motors. During tilting procedure, the motors RPMs are not kept constant and they vary to feed the proper command into the system.

The main consideration which has been taken into account in solving this control problem is "not exceeding the thrust threshold"; the maximum thrust (motor RPM) an individual motor can provide. Moreover, there is no need to reverse the rotor system to provide negative thrust. In order to maintain or reduce the forward speed, motors RPMs are reduced accordingly or in case of hover flight, forward speed is controlled by increasing and decreasing the forward and aft hover motors, respectively.

Use of classic control surfaces, i.e. elevator, ailerons, rudder, etc., motors RPM, use of unconventional control surfaces or a novel control method are amongst the possible control policies for this type of aircraft [55]. A combination of canardvator, ailerons, and rudder have been used for control in pitching, rolling, and yawing channel.

Motors rotational speed has been used as control input for numerous functions in different flight phases; for instance, altitude hold and pitch damper in transition to cruise mode are obtained by this means.

Tuned PID controllers have been used to attain performance and control objectives, which have been a short response time, maintaining a specific level of robustness, and relatively low gains. As the simulation results suggest, PID controllers have worked just fine. For future work, in case of operating point being too far from equilibrium point, a nonlinear controller can be designed or a robust control approach may be adopted, too.

14.3. Control Allocation

Here, the problem of control allocation is to determine how much each control surface is deflected to get a desired force-moment output. Each rotor affects thrust and the moments in all three channels in hover and transition to cruise flight modes. In cruise, again each lift fan affects the same forces and moments, but they primarily contribute to the forward force (thrust) and yaw moment. Figure 61 represents the control allocation and transition sequence accomplished for Spricho.
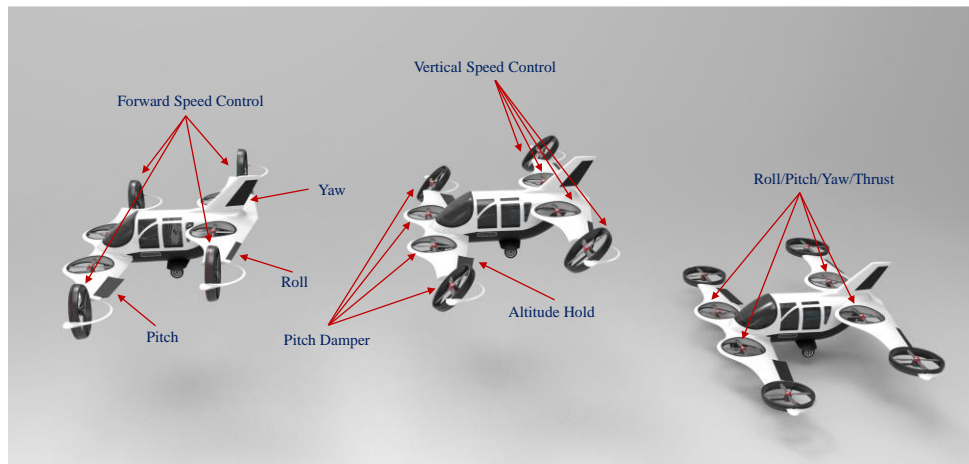
Figure 61: Transition sequence & Control allocation for Spricho in hover, transition to cruise, and cruise

The system at hand is of course over-actuated, due to actuator redundancy implemented in the design. It has 29 degrees of freedom (8 motors, 8 variable pitch actuators, 5 control surfaces, 8 tilt actuators). The proposed control strategy is executed without the use of variable pitch capability and tilt actuation, so the setup reduces to 13 degrees of freedom. This actuator redundancy is of high importance because it ensures the controllability and safety of the aircraft. A case of OEI is studied later as a demonstration of this matter. Control allocation for different flight modes are as follows.

14.3.1. **Hover and Transition to Cruise**

The ability to perform a stable hover at an altitude of 50ft. MSL has been stated as an RFP requirement. Now, the operational environment plays a significant role in this phase of the flight; as a severe vertical or horizontal gust can jeopardize a safe hover. Motors rotational velocities are employed as control inputs to stabilize the aircraft in pitch, roll, and yaw channels. In addition, the torques on the main body have been cancelled out by properly deciding on the direction of rotation of the motors, which can be seen in Figure 55.

Transition from hover to cruise is the most crucial part of this section, both for stability analysis and controller design, due to its high dependency on the aircraft configuration. When the cruise motors start to tilt, losing altitude becomes a concern; the motors produce nose-down pitching moment when tilted, so the controller uses hover motors RPMs to hold the altitude of the aircraft.

14.3.2. **Cruise**

In cruise, canardvator are used to control the pitch moment, while roll moment is controlled by deflecting the ailerons. As mentioned before, use of vertical stabilizer and rudder has been rendered necessary to control the yaw moment whenever needed. Altitude and speed hold have been accomplished by the employing the canardvator and 4 cruise-motor rotational speeds as control inputs.

In case of rudder failure during flight, a virtual rudder can be used instead, which then is converted to differential thrust of cruise motors as the new control input [53].

14.4. Simulation Results

The simulation has been carried out for a flight scenario where there are three passengers and a pilot onboard the aircraft. The initial results have been feedbacked to control surface design 13.2] and W&B [12] sections, to properly modify the design to help achieve the best performance. Through this cycle, the canardvator area has been raised from the initial value of 15 ft^2 to final value of 16 ft^2. The closed-loop responses of state variable and control inputs are presenter later in this section.

14.5. Hover Flight & Transition to Cruise

Two equations have been solved simultaneously to attain the equilibrium condition at hover; where aircraft is balanced in a constant altitude. Flight condition and Initial required thrust to maintain altitude and pitch stability are tabulated and presented in Table 41.

Table 41 Flight condition and thrust data for stable hover flight

h [ft.]	Scenario	Weight [lb.]	X_{CG} [ft.]	T_1 [lbf]	T_2 [lbf]	T_3 [lbf]	T_4 [lbf]	T_5 [lbf]	T_6 [lbf]	T_7 [lbf]	T_8 [lbf]	T_{total} [lbf]
50	3 PAX + pilot	4371	6.0359	600	600	600	600	492	492	492	492	4368

The simulation starts from a stable hover at an altitude of 50 ft. at $t = 0$. At this moment, the cruise motors start to tilt with a tilt-angle rate of 9 degrees per second. After 10 seconds, the transition is completed. Hover motors are operating throughout the transition sequence and are gradually shut down after the end of this phase (which takes about 4 seconds).

Based on the results, the aircraft is able to maintain the altitude (50 ft.) throughout the transition, with only a ± 2 ft. change in altitude at the end of 10 seconds. The forward velocity reaches the value of 132.2 $\frac{ft}{s}$ (78.33 kts), which has been an objective for the design (1.3 V_{stall}) [ref]. It also travels 434 ft. in x-direction in 10 seconds of transition. The simulation results are presented in Figure 62 to Figure 75.
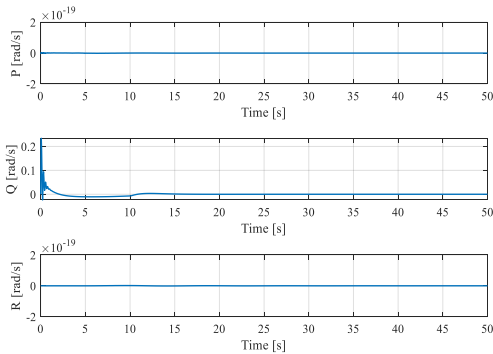
Figure 64: The response of angular velociti
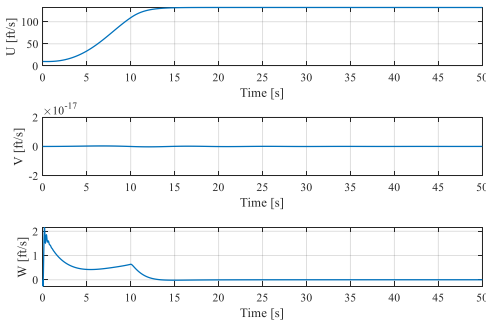
Figure 63: The response of linear velocities
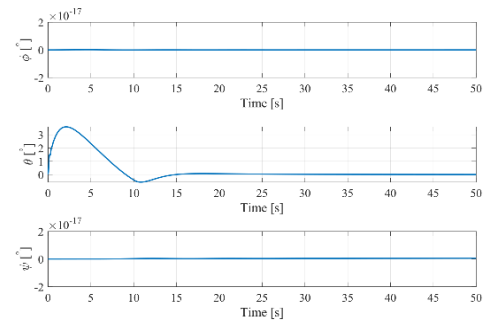
Figure 62: The response of Euler angles
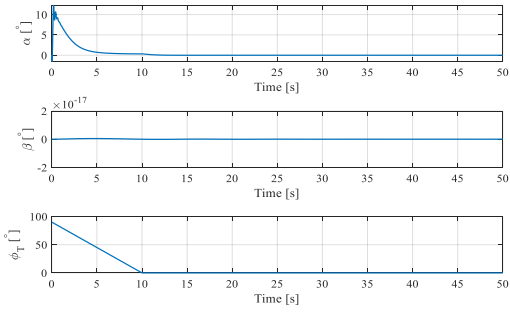
Figure 67: The response of AOA, β, and φ_T
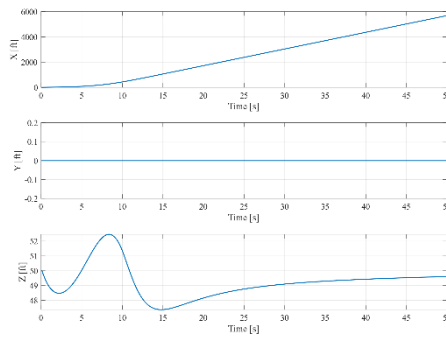
Figure 66: Position of the Aircraft
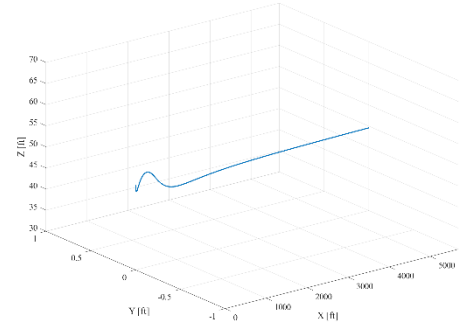
Figure 65: 3D Flight Path
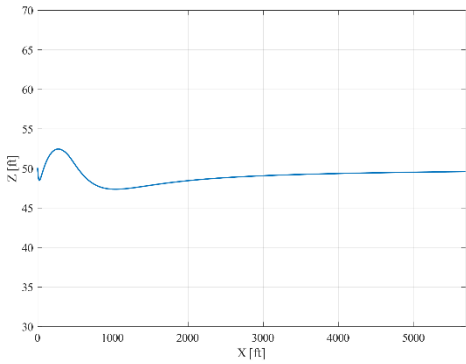
Figure 69: 2D Flight Path (ZX)
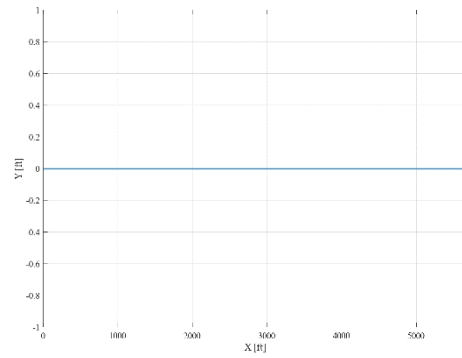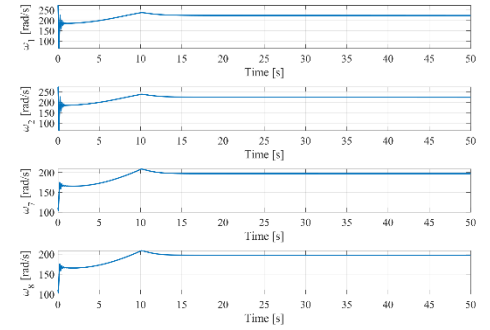

Figure 73: 2D Flight Path (YX)

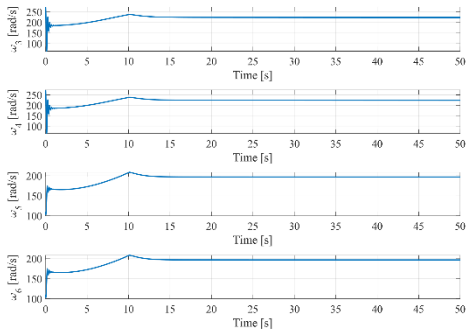Figure 68: Hover Motors' Rotational Speed
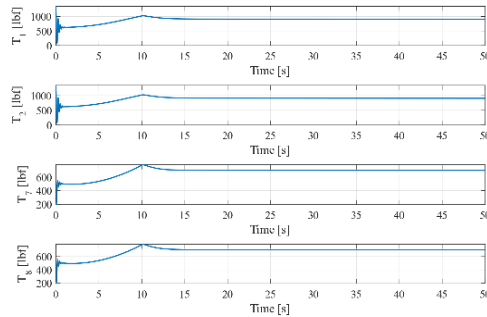

Figure 72: Cruise Motors' Rotational Speed
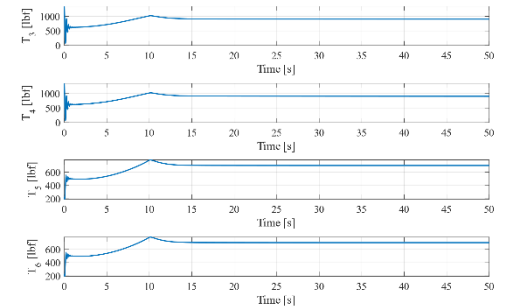

Figure 71: Hover Motors' Thrust Level

Figure 70: Cruise Motors' Thrust Level

Figure 75: Control Efforts
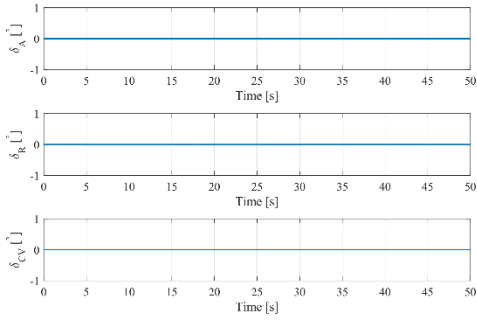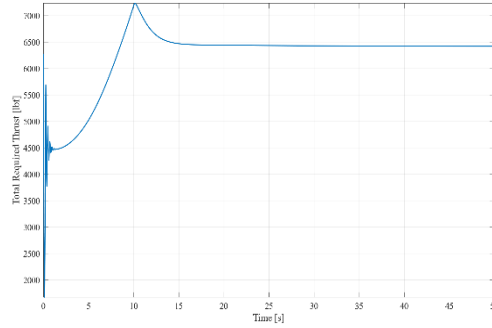

Figure 74: Total Required Thrust

It can be seen in Figure 75 that the control efforts are well below the maximum allowable motor RPM of 314.16 $\frac{rad}{s}$.

14.6. Cruise Mode

14.6.1. Steady State, Rectilinear Flight

Level of stability and controllability of the aircraft can be deduced by examining each figure. The linear velocities have behaved the way they were supposed to; the forward velocity, flight altitude, AOA, and δ_{CV} have attained the objective values of $240.51 \frac{ft}{s}$ (164 mph), 2500 ft, 1.9652, and 8.8178 degrees. There is no lateral travel in flight path and the control efforts are well below the maximum allowable motor RPM. The simulation results are shown in Figure 77 to Figure 85
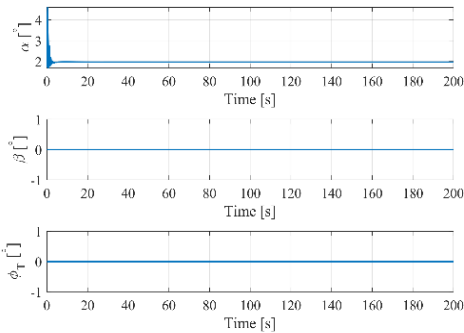
Figure 76: The response of AOA, β, and
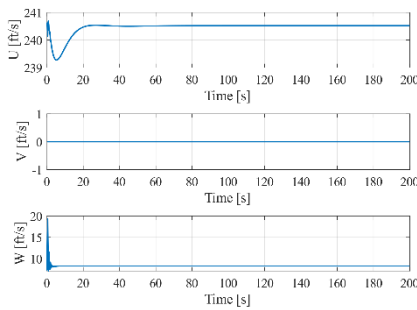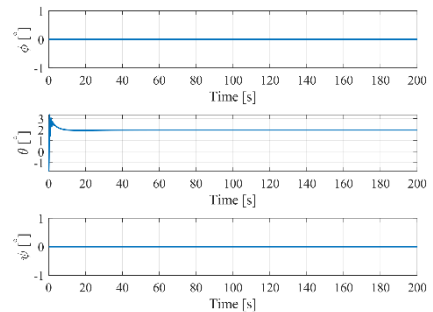

Figure 78: The response of linear velocities

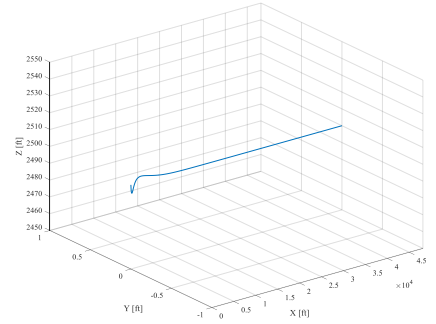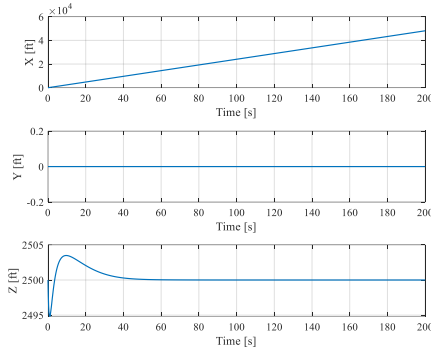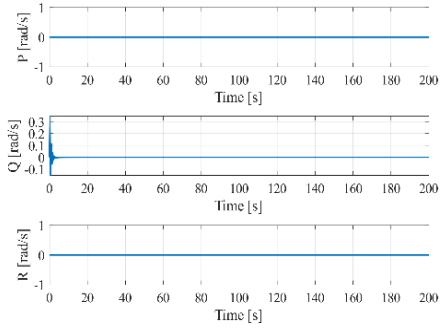
Figure 77: The response of Euler angles

Figure 81; The response of angular velocities

Figure 80: Position of the Aircraft
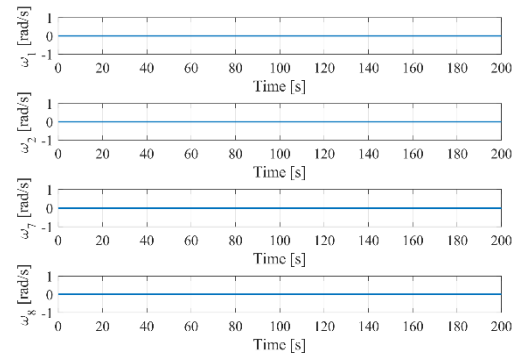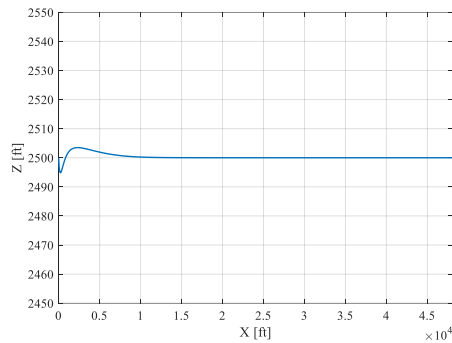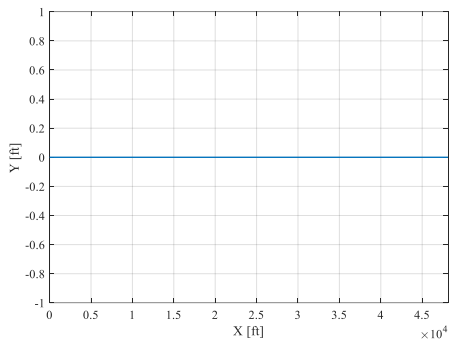

Figure 79: 3D Flight Path

Figure 84: 2D Flight Path (YX)

Figure 86: 2D Flight Path (ZX)

Figure 83: Hover Motors' Rotational Speed
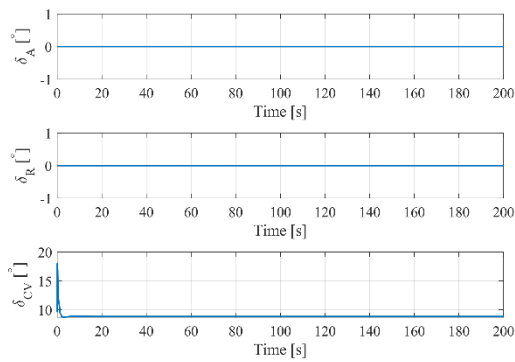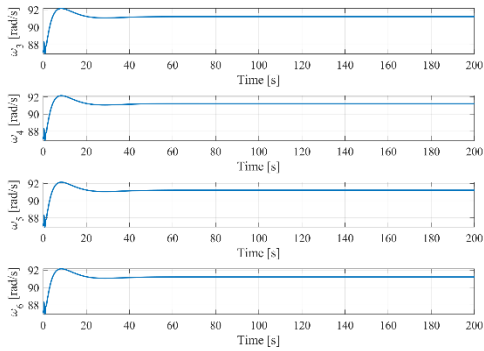

Figure 85: Cruise Motors' Rotational Speed

Figure 82: Control Efforts

14.6.2. Perturbed, Rectilinear Flight

Here, a $25[\frac{ft}{s}]$ vertical gust velocity based on FAR23 and MIL-F-8785C is introduced into the system, by the means of Dryden Turbulence Model [46], between simulation times of 80 to 120 seconds. The system proves to have sufficient level of robustness in order to reject atmospheric disturbances in cruise.

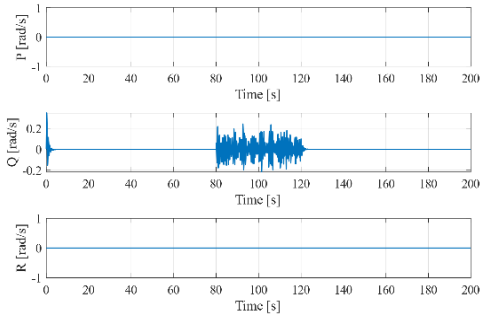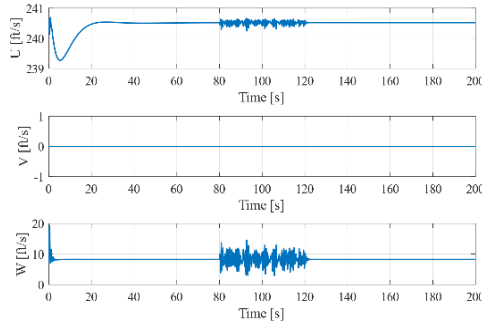Figure 88: The response of angular velocitie
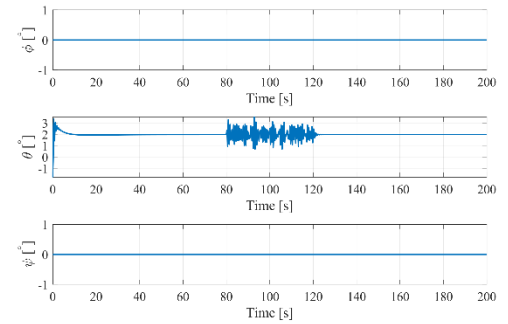

Figure 87: The response of linear velocities

Figure 89: The response of Euler angles

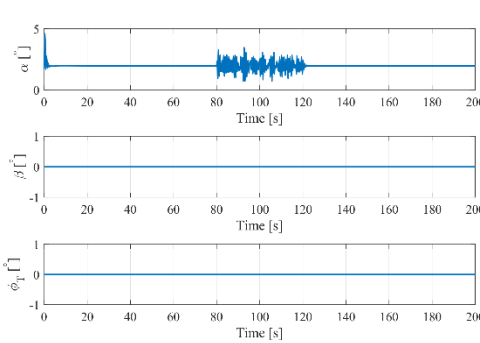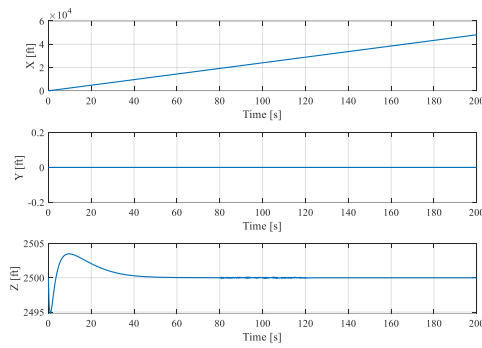Figure 92: The response of AOA, β, and φ_
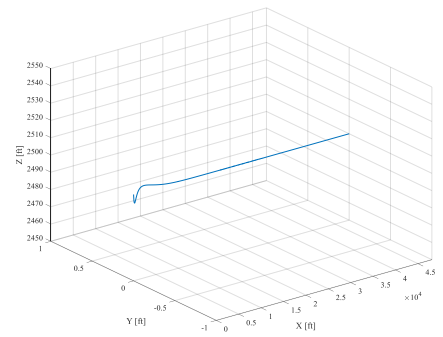

Figure 91: Position of the Aircraft

Figure 90: 3D Flight Path

Figure 97: 2D Flight Path (ZX)

Figure 96: 2D Flight Path (YX)
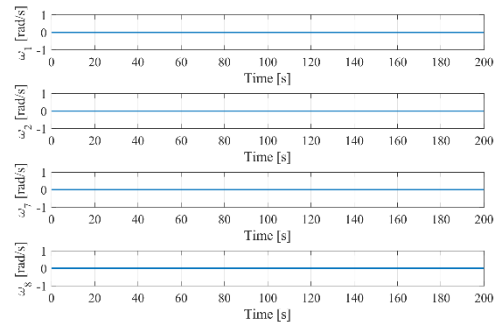
Figure 95: Hover Motors' Rotational Speed
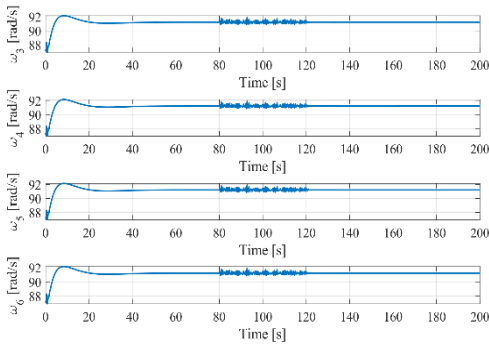
Figure 93: Cruise Motors' Rotational Speed
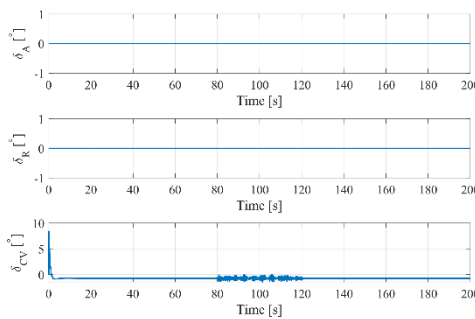
Figure 98: Control Efforts
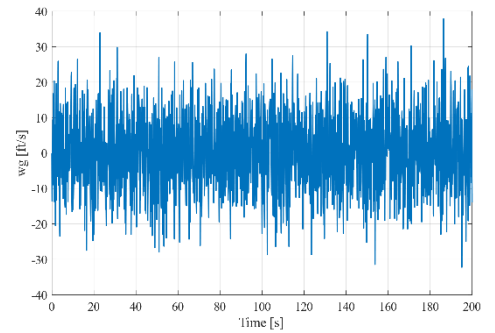
Figure 94: 25[ft/s] vertical gust velocity

14.6.3.   **Steady State, Level Turning Flight**

Although the aircraft is able to hold a 74.7 degree-bank angle (based on a 3.8g load factor), passenger comfort plays an important role to limit the maximum bank angle. Typically, airliners are limited to a 25 degree-bank angle. Here, a minimum turn radius of 1500 ft. is desirable, assuming a 1000 ft. wide building with a safety margin of 1000 ft. from each side of the building.

Trimmability assessment has been done for steady state turn maneuver and the results are presented in Table 42.

Table 42: Steady 3.8g 360-degree turn trim data

h [ft.]	Scenario	V [ft./s]	Weight [lbs.]	φ [deg]	α [deg]	β [deg]	δ_{CV} [deg]	δ_R [deg]	δ_A [deg]
2500	3 PAX + pilot	240.51	4371	25.0008	2.1543	-0.0216	0.1948	-0.0007	-0.1662

As mentioned in [41], flight in a steady level turn takes place at a higher angle of attack in comparison with steady state rectilinear flight, as has been verified by this calculation. Maintaining maximum bank angle of 25 degrees has been the objective in the following simulation results, which are presented in Figure 100 to Figure 109

Figure 101: The response of angular velocities

Figure 102: The response of linear velocities

Figure 103: The response of Euler angles

Figure 107: The response of AOA, β, and φ_T
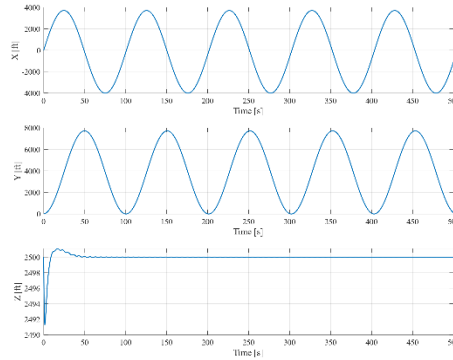
Figure 106: Position of the Aircraft
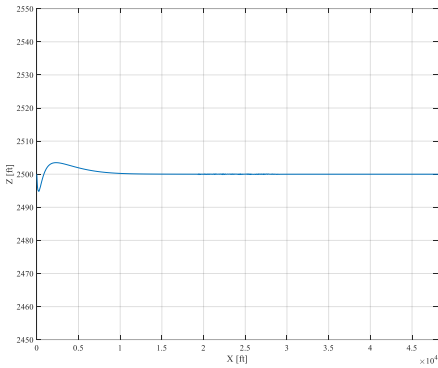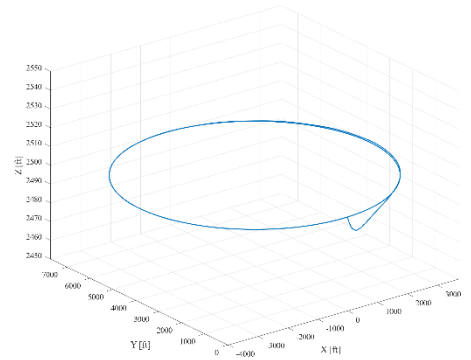

Figure 100: 3D Flight Path
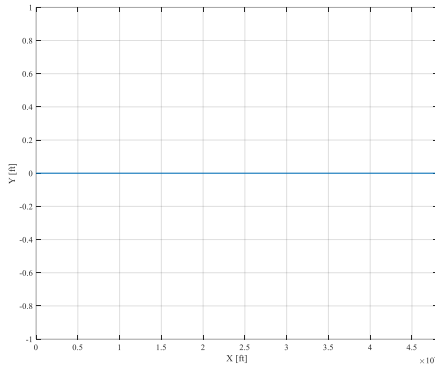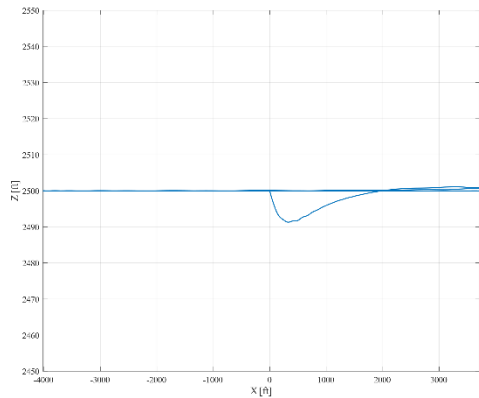

Figure 99: 2D Flight Path (ZX)
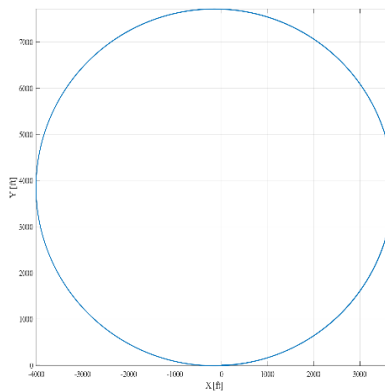

Figure 105: 2D Flight Path (YX)
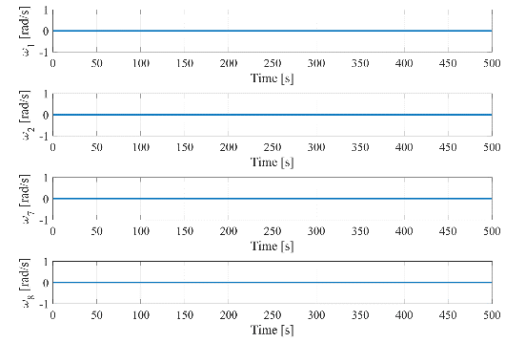
Figure 104: Hover Motors' Rotational Speed
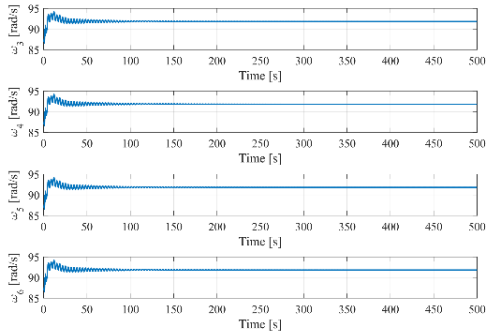
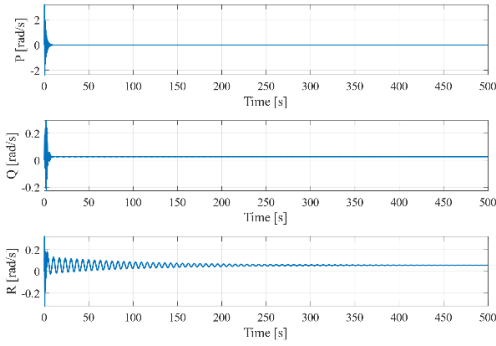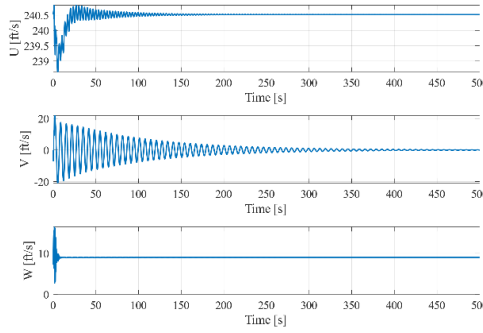Figure 108: Cruise Motors' Rotational Speed
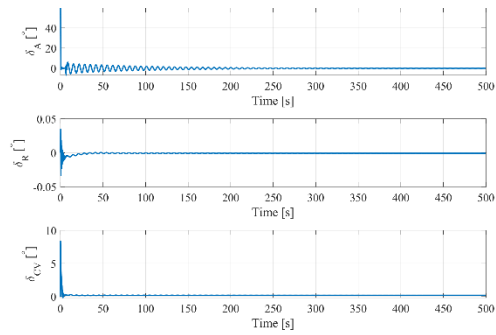
Figure 109: Control Efforts

14.6.4. OEI Failure Mode

For the simulation purposes, it has been assumed that the front starboard cruise motor fails during cruise at 2500 ft. and the front-left motor is running at its initial cruise required thrust. The two aft cruise motors and the front port motor will compensate for the required thrust to cruise and the aircraft will carry on with its mission. The effect of failed-motor drag induced yawing moment has been discussed in [Critical Engine Out].

In order to maintain straight and level flight with a bank angle of less than 5 degrees, the required aileron and rudder deflections have been calculated and the results presented in Table 43. The desired bank angle has been set to zero.

Table 43 Lateral-directional trim condition for Spricho (in case of OEI)

h [ft.]	Scenario	V [ft./s]	Weight [lbs.]	φ [deg]	α [deg]	β [deg]	δ_{CV} [deg]	δ_R [deg]	δ_A [deg]
2500	3 PAX + pilot	240.51	4371	-1.6749	1.9251	0	8.9725	0.3151	0.3495

The results indicate that the aircraft can be stabilized in case of an OEI Figure 110 to Figure 119 represent the results of the nonlinear simulation.
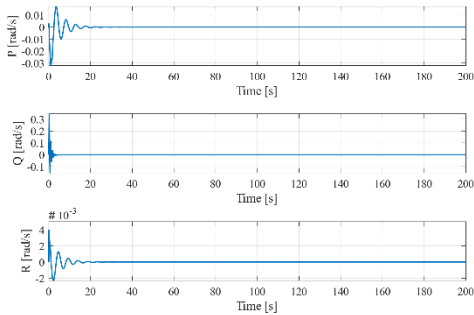
Figure 112: The response of angular velocitie   *Figure 111: The response of linear velocities*   *Figure 110: The response of Euler angles*
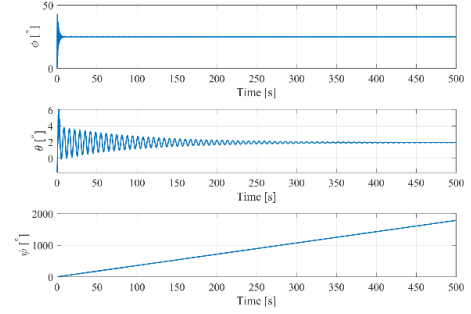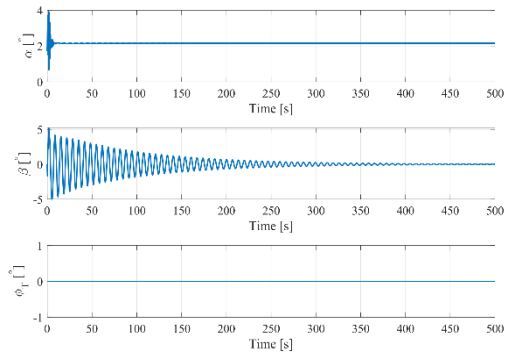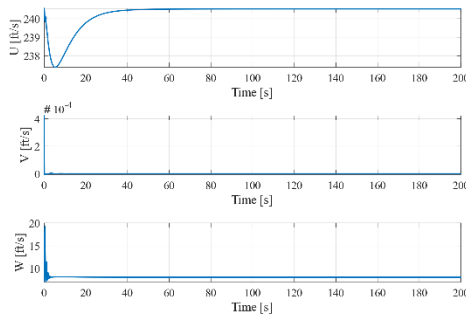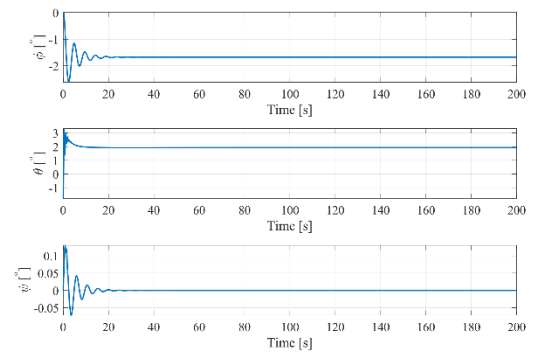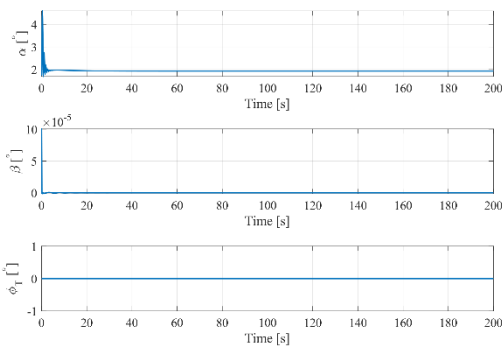
Figure 115: The response of AOA, β, and φ_T
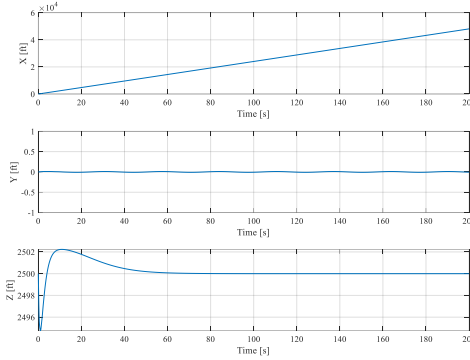
Figure 114: Position of the Aircraft
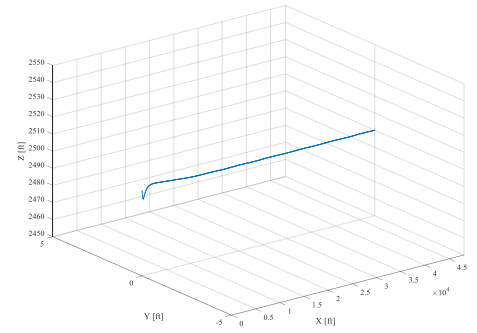
Figure 113: 3D Flight Path
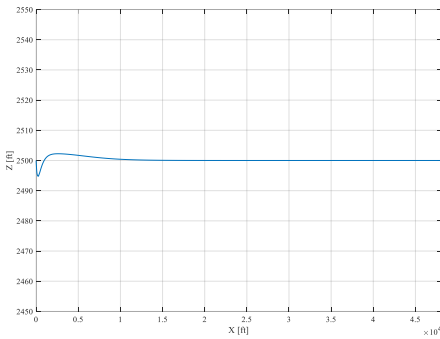
Figure 117: 2D Flight Path (ZX)
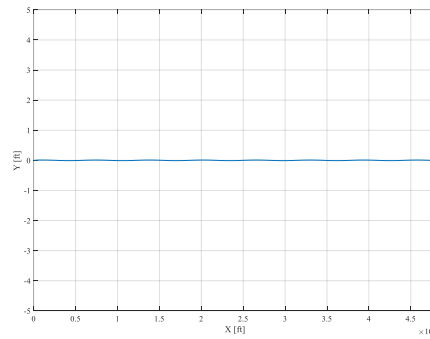
Figure 120: 2D Flight Path (YX)
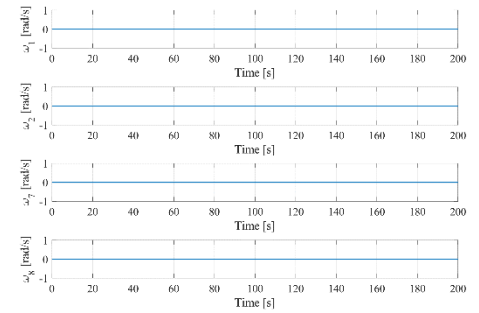
Figure 116: Hover Motors' Rotational
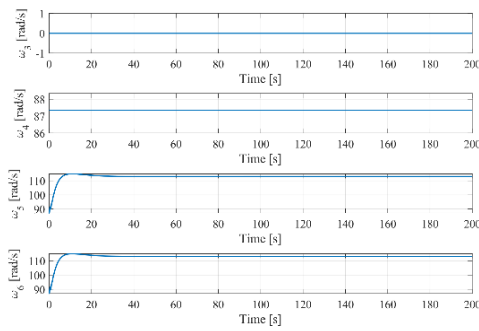
Figure 118: Cruise Motors' Rotational Speed
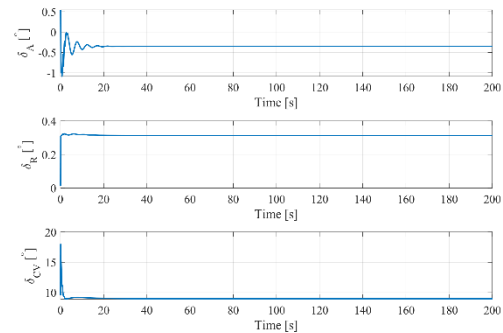
Figure 119: Control Efforts

It can be concluded that, in case of an OEI, safety of flight is guaranteed and the aircraft is post-failure operable.

The results are also proving that the designed vertical tail area has been sufficient to control the yawing channel.
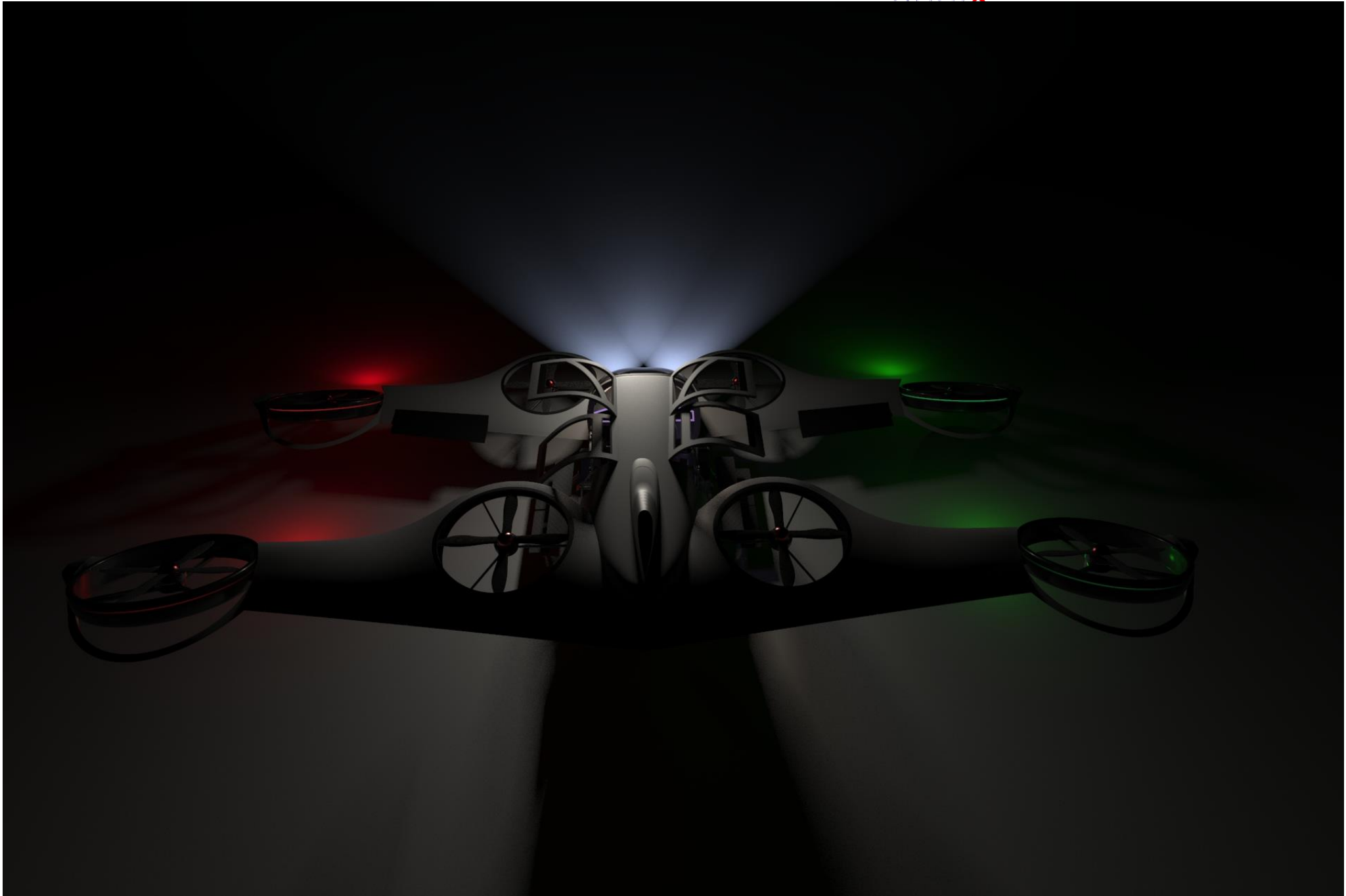
15. Systems

In this section, a brief description of Spricho's systems are presented. In most cases, the systems are accompanied by a backup to ensure a safer flight.

15.1.1. ADS-B Transceiver

In absence of TCAS, ADS-B transceiver is used in aircraft's avionic to provide a low-cost, and reliable method to avoid mid-air collision. There are two ADS-B transceiver in each aircraft to ensure safety, and there is more than one ADS-B receiver used in the air traffic control center.

15.1.2. Electromechanical Actuator

Two types of actuators are usually used in aircrafts, hydraulic actuators and electromechanical actuators. Electromechanical actuators in comparison to hydraulic actuators are lighter, smaller, and more efficient, and also they require less maintenance. These actuators are more reliable and need less redundancy [5].

15.1.3. Exterior Lighting

The aircraft is equipped to Pulsar NSP (Navigation/Anti-collision Strobe/Position), Taxi and landing lights to comply with night operation's requirements.

15.1.4. Cabin Environment Control System

Environment control system is equipped to an Arctic air RAC (for cooling) and two Hornet 45 heater (for heating). their modular design results in easier maintenance.

15.1.5. Flight Control System

Flight control system is equipped to a pair of customized Lambda quad as deep learning PC, and two Arduino 2560. This system requires a monitoring unit using a pair of EO/IR cameras and WASP's AGL sensors.

Moreover, as a future aircraft, Spricho possess a fly-by-wire control system.

15.1.6. Avionics and Instruments

Avionic system mainly consists of three Skyview HDX, a 10" touchscreen panel display from Dynon avionics providing the pilot with required information. Skyview HDX has complete compatibility with used Mode-S transponder, ADS-B (traffic and weather), and COM radio. Its exclusive moving map and navigation platform combining with MGF Skydisplay's HUD (head-up display) makes flight more reliable and safer in both IFR and VFR

modes. All avionic systems use 12V current. Displays are equipped to backup batteries which can provide enough energy for 1 hour in case of emergency. Redundancy in all vital components including ADAHRS, AOA/Pitot Probe Heated w/controller, ADS-B transceiver (traffic and weather), GPS receiver, Flight Control System, cameras, AGL sensor, IFR navigator, actuators is complied.

16. Fuselage Layout Design

16.1. Fuselage

An inside-out approach is utilized to determine the geometry of the fuselage. The main criteria are providing a comfortable cabin and having enough space to place the required components, systems, and instruments. Birds have been developing for millions of years always have been the source of inspiration for humans. Hence, after the interior arrangement is determined, it was tried to fit the body of a bird to the proposed layout. Swallows are small birds residing in almost every corner of the world. They are among the most agile passerine birds and are excellent flyers, and their streamlined body shape has provided them with an efficient flight [1]. Therefore, the geometry of Spricho's fuselage is inspired from swallow body shape and then is tailored to be able to carry wings, motors, vertical tail and other components. Moreover, further modifications have been done to improve its aerodynamic performance and visual appeal.

16.2. Door and stairs

There is a variety of options for the door of the aircraft. Number of doors and their location has a direct effect on the seat positions as well as size and shape of the cabin. Moreover, the opening affects the beauty and ease of boarding and egress.

Although it is desirable for pilot to have a separate door, four doors arrangements is decided, because after 8 years we will enter to autonomous phase and we want all passengers to have the same comfort. Moreover, Moving in cabin is difficult for passengers and it is unpleasant during

Figure 121: doors and stairs of Spricho

the flight. Also using an aisle results an unnecessary large cabin and unusable space. Taking these into consideration, four doors Spricho is confirmed, causing a remarkable easiness in boarding and egress and decreasing the boarding time. Three options for stairs are considered. Using access boarding stairs needs additional use of ground crews thereby increasing both the cost of operation and boarding time. Skid tube step or attached stairs cause lack of comfort and beauty. It also increases parasite drag during flight. On the other hand, Air stairs are fast deployed and comfortable. Therefore, Air stair is selected Figure 121. Each door consists of two parts. The lower part opens deploying the stairs and the upper part opens upward preventing passengers to get wet in rainy days.

17. Interior Design

17.1. Seat Arrangements

The purpose of this section is to determine the cabin seats arrangement to reduce unnecessary empty space as it reduces structural weight thereby decreasing energy consumption.

In Figure 122, five different layouts are conceived and their pros and cons are evaluated in Table 44.
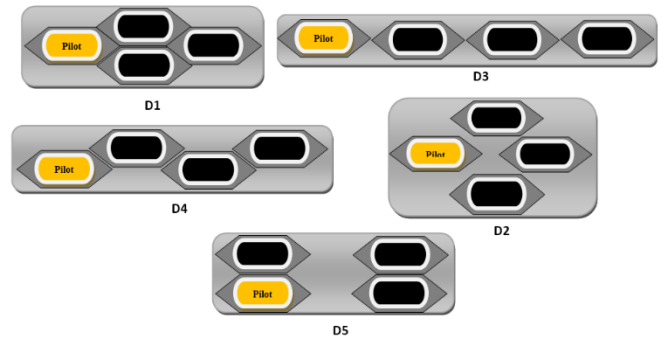
Figure 122: types of seat arrangement

Table 44: Pros and cons of seat layout

Configuration	PROS	CONS
D1	Optimal use of space	Two seats are backward facing
D2	---	Uncomfortable boarding
D3	---	Lengthy fuselage and Uncomfortable boarding
D4	Sufficient privacy	Lengthy fuselage and Uncomfortable boarding
D5	Ease of boarding	Pilot's distraction due to the adjacent seat passenger

D5 layout is selected as its problem is solved when the aircraft changes to its autonomous version.

Shows cabin changes after eight years which pilot seat will replaced with passenger seat.

17.2. Seat Dimensions

Seats and cabin of Spricho is designed to assure a high level of comfort and safety. The geometrical parameters of seats and cabin are illustrated in.Figure 123 and Figure 124
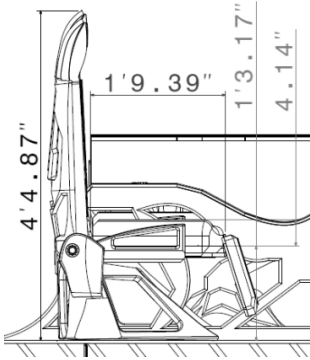
Figure 123: seat dimensions
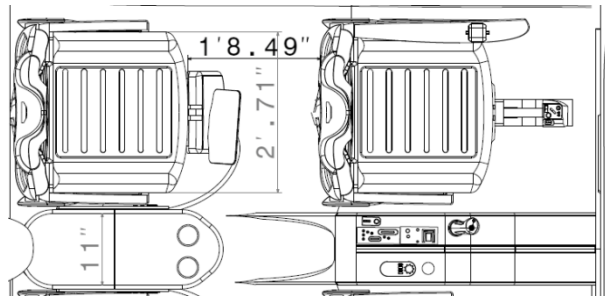
Figure 124: seat and cabin dimension

17.3. Pilot Instrument Arrangement

Spricho is designed with one pilot. As a next generation aircraft it boasts a glass-cockpit. It provides the pilot with a user-friendly interface for controlling the aircraft. Pilot controls the aircraft with the Hands-on Throttle and Stick (HOTAS) concept. The pilot seat is designed for high visibility and full control over the aircraft during different phases of flight, as shown in Figure 125

The cockpit instruments are illustrated in Figure 125 and summarized below.

1- Side Stick

2- Heads up Display

3- Pedals

4- Throttle

5-multifunction Display 1

6-multifunction Display 2

7-multifunction Display 3

8-EngineStart/Emergency Landing switch

9-VHF COM Radio
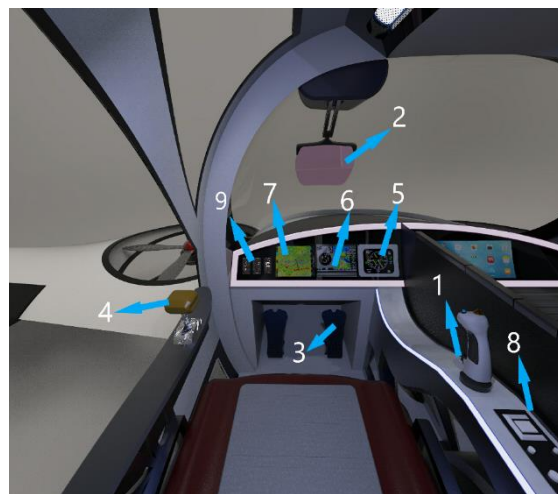
Figure 125: pilot instruments

17.3.1.   Multifunction Displays

The user (pilot or passenger in autonomous version) controls the settings using a touch panel. The location and type of displays, controls, and other instruments is selected to achieve the highest commonality.

17.3.2.   Side Stick

Spricho has a special stick, which helps to control the aircraft in both rotorcraft and fixed-wing modes. It also eases controlling the transition phase. There is a transition switch on the stick (Figure 126) .Pressing this switch forward and backward starts the transition between rotorcraft and fixed-wing modes, respectively. Moreover, there is a shutdown button for hover motors on the stick. It allows the pilot to change only the power of cruise motors after this button is pressed off.
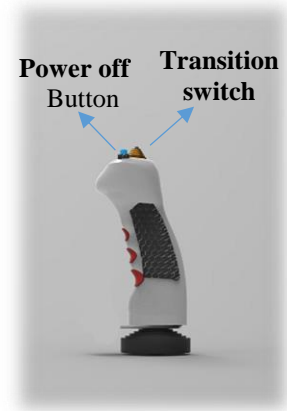
Figure 126: Stick

17.4. Cargo Compartment

The cargo compartment is allocated for passengers comfort. Passenger is allowed to carry on baggage within weight and dimension limit which is 20 [lb.] and 0.5[ft.]*1[ft.]*1.5[ft.].
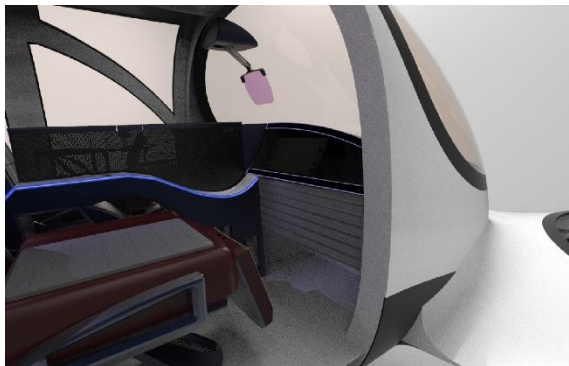
Figure 127: Front Passenger's cargo door

Figure 128: Rear passenger's cargo compartment

18. Structural Analysis and Manufacturing

This section addresses the structural aspects of Spricho and determines the material used as well as dimensions of aircraft's components such as spars, ribs, etc.

18.1. V-N Diagram

The first step of structural analysis is drawing the V-n diagram. Due to the presence of hover and transition phase, Spricho is similar to a helicopter, and in fixed-wing mode Spricho is an airplane. Therefore, both regulations must be met.

Figure 130 is drawn for clean configuration at the maximum gross weight at sea level, which is the high loaded structural condition. This figure shows the combined V-n diagram with gust lines.

According to [11], the maximum upward gust load is specified at 25ft/s and 50 ft/s for structural consideration.

Figure 129: combination of FAR27 and FAR23 for v-n diagram

18.2. Material selection & Manufacturing method

Given the fact that Spricho's ETS is 2028, it is necessary to utilize up-to-date technologies. By studying the market and new technologies, it is expected that 3D printing technologies and also Nanocomposites will make significant progress and will take a large part of the market.

Figure 130: V-n Diagram

Here, 3d printing with carbon fiber is used just for fuselage skin due to its complex geometry. It allows manufacturing with 3d printing to be cost-effective and straightforward. To support the fuselage skin, autoclaved carbon composite is used in frames and longerons.

Weight reduction is the prominent advantage of composite material usage and is the essential factor in incorporating it in aircraft structure; especially, for electric aircraft. Moreover, composite materials do not corrode as easily as other types of structures and composite designs last longer than aluminum, meaning fewer maintenance and repair costs. Therefore, the great advantage (weight reduction) of using composite materials outweighs its disadvantages such as harder surface repair and Spricho is decided to be a full composite E-VTOL.

Furthermore, in order to avoid potentially negative consequences such as damages from a lightning strike,

a protective aluminum film is used.

Table 45: materials and manufacturing methods

Material	Manufacturing method	application	Reason for use
HexTow®HM63Carbon Fiber	Autoclave	Wing skin, spars, ribs, empennage structure, frames, longerons, bulkheads	High strength, high performance, high modulus
HexWeb® Acousti-CAP®	Autoclave	Motor's fan	Reduce engine noise by up to 30%. [56]
CarbonX™ Carbon Fiber Ultem™ PEI 3D Printing Filament [57]	3D printing	Fuselage skin	Easy manufacturing
acrylic/ polycarbonate	automated thermoforming	Windows, pilot windshield	It is transparent and lightweight
Lamitex®PL-68	Autoclave	Motor's blades	High flexural, compressive and bond strength [40]

Table 46: HexTow® HM63Carbon Fiber properties

Material	0º Tensile Strength	0º Tensile Modulus	0º Tensile Strain	0º Short Beam Shear Strength	0º Compressive Strength	0º Compressive Modulus	Fiber Volume
HexTow® HM63Carbon Fiber	2,410 MPa(349. 541kpsi)	255 GPa	0.9%	101 MPa	1,310 MPa	221 GPa	60%

Table 47: CarbonX™ Carbon Fiber Ultem™ PEI 3D Printing Filament properties

Material	Tensile strength	Tensile modulus	Tensile elongation
CarbonX™ Carbon Fiber Ultem™ PEI 3D Printing Filament	145Mpa	7700Mpa	1.5%

18.3. Wing Structural Design

The wing design is begun with determining the load wingspan. Figure 134to Figure 136 show load, shear force,

and bending moment distribution in 3.8g aerodynamic maneuver in forward flight and rotorcraft mode (vertical take-

off or landing). As can be seen, the root of the wing is the critical point. Hence, the wing root is designed with a safety

factor of 1.5

.
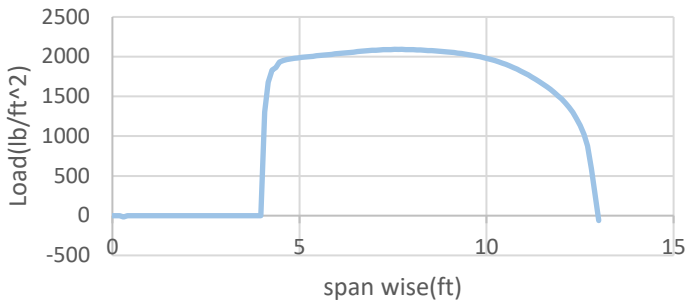
Figure 134: Load distribution along wing span in forward fly
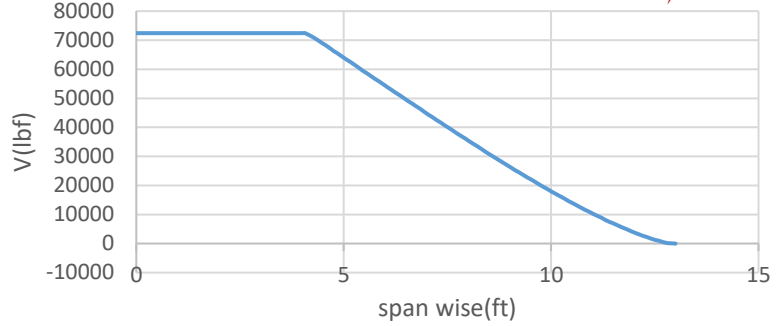
Figure 134: shear force distribution along the wing distribution in forward fly
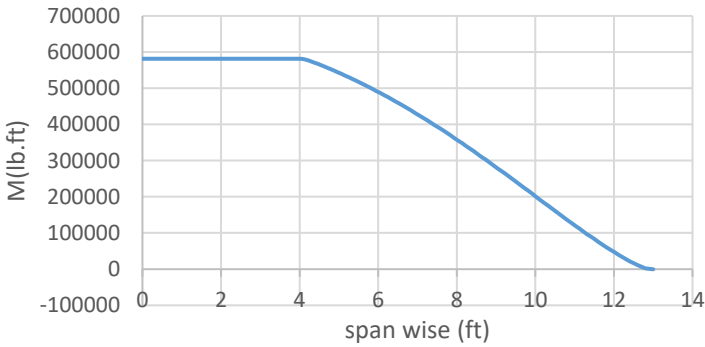
Figure 132: Moment distribution along the wing span in forward fly

Figure 132: Moment distribution along the wing span in hover mode
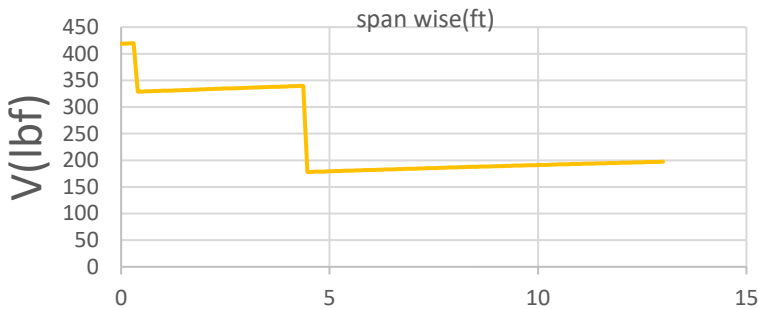
Figure 136: shear force distribution along the wing distribution in hover mode
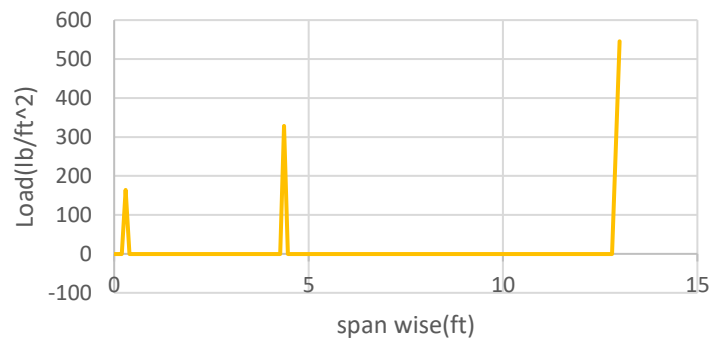
Figure 136: Load distribution along wing span in hover mode

The composite material used for the wing is made by quasi-isotropic laminates [- 45/0/+ 45/90]8s of HexTow®HM63Carbon Fiber as told in material section.

The wing structure consists of two spars. One is at 20% chord, and another is at 75% chord. There is an engine at the wing root, therefore,
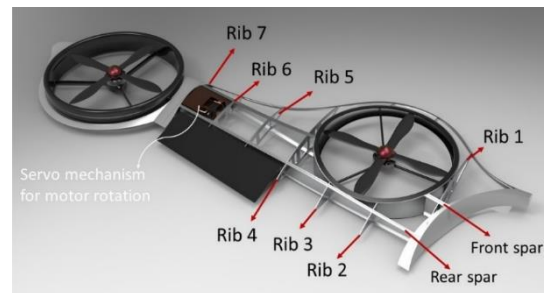
Figure 137: Wing Structure

the front spar which is in 20% chord should turn around the engine and then two spars merge to each other

and turn around the tip wing motor as illustrated in as illustrated in Figure 137.

Since there are two motors in Spricho's wing the rib spacing is chosen to be 30 inches.

Table 48: the wing spar specification

	Suggested [18]	Chosen
Front spar	15-30% chord	20%
Rear spar	65-75% chord	75%

Table 49: skin and spar's thickness

Object	Value
Skin thickness	0.08 in
Front spar thickness	0.2 in
Rear spar thickness	0.15 in

Rib number 5 and 6 help the spars to withstand bending moments. Rib 1,2, 3, 4 and 7 are reinforced components

which in addition to doing the job of rib 4 and 5, hold the motor weight and hover force made by motors.

Table 18-50 Rib Functions and their thickness

Rib number	function	thickness
Rib 1,2,3,4,7	Hold the motor weight and hover force made by engines	0.15in
Rib 2,3	Help Rib1,4 to hold the engine weight and hover force	0.15in
Rib 5,6	Help the spars to withstand bending moments	0.1 in

18.4. Fuselage design

Since the maximum flight altitude is 12500ft, there is no need to pressurize the cabin. The fuselage consists of

three parts.1) Fore body 2) mid body 3) Aft body.

The suggested value for longeron spacing is 10-15 inches [5], and the chosen value for longeron spacing is 12

inches. The lower longeron of the fuselage is reinforced as it is the main longeron without any breaking point. It is

connected to landing gears hence, it must withstand a large load.

Moreover, the longerons connected to wing should be reinforced as well, because they transfer the wing loading to the fuselage. The suggested frame spacing length for a small aircraft is 24-30 inches [14]. But in any part, these values are different from each other based on their functions and the loads they must withstand.
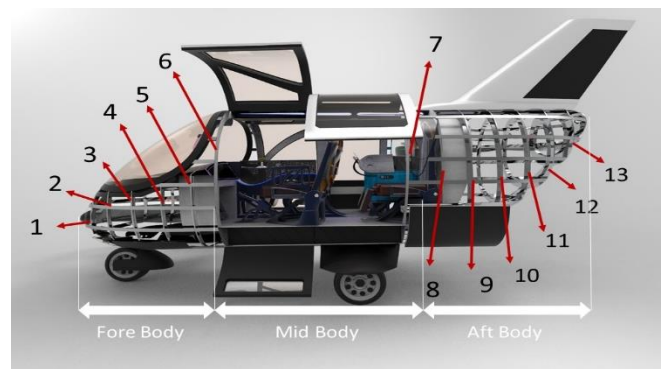
Figure 138: Fuselage Structure

18.4.1.   **Fore Body**

In front of the fuselage, batteries are placed which weigh 1200lb. In addition, the landing gear is attached to front

frames. Therefore, there are more frames in front of the fuselage as shown in Figure 138 fuselage frame spacing is

decreased to 12 inches due to the heavy weight of batteries and motors placed in front of the fuselage. The frames

which are connected to wings and nose landing gear are reinforced with increasing the frame depth.

18.4.2.   **Mid Body**

Doors and windows are located in this part. Frames cannot be close to each other thereby there are reinforced

frames in position number 6 and 7.

18.4.3.   **Aft Body**

The frames in this part should be close to each other and also be reinforced as heavy motors, and the vertical tail

are placed at the rear wing. The chosen value for frame spacing is about 13 inches.

Table 51: fuselage frame specification

		Fore body	Mid body	Aft body
	Suggested [5]	chosen		
Frame depth	1.5 inches	1.5 inches	1.8 inches	1.5 inches
Frame spacing	24-30 inches	12 inches	-	13 inches

18.5. Empennage design

Empennage structure is similar to the wing structure. It has two spars. Due to the big area of rudder, these spars

are near the leading edge of the vertical tail. The spars are connected to longerons and frames in fuselage. In Figure

139 the empennage structure with its spars and ribs is shown.

Table 52: Empennage structural specification

	suggested [5]	chosen
Front spar location	15-25%chord	10%chord
Rear spar location	70-75%chord	40%chord
Rib spacing	15-30 inches	8 inches
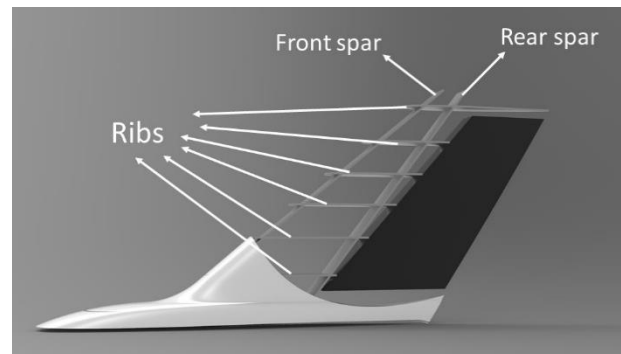
Figure 139: Empennage structure
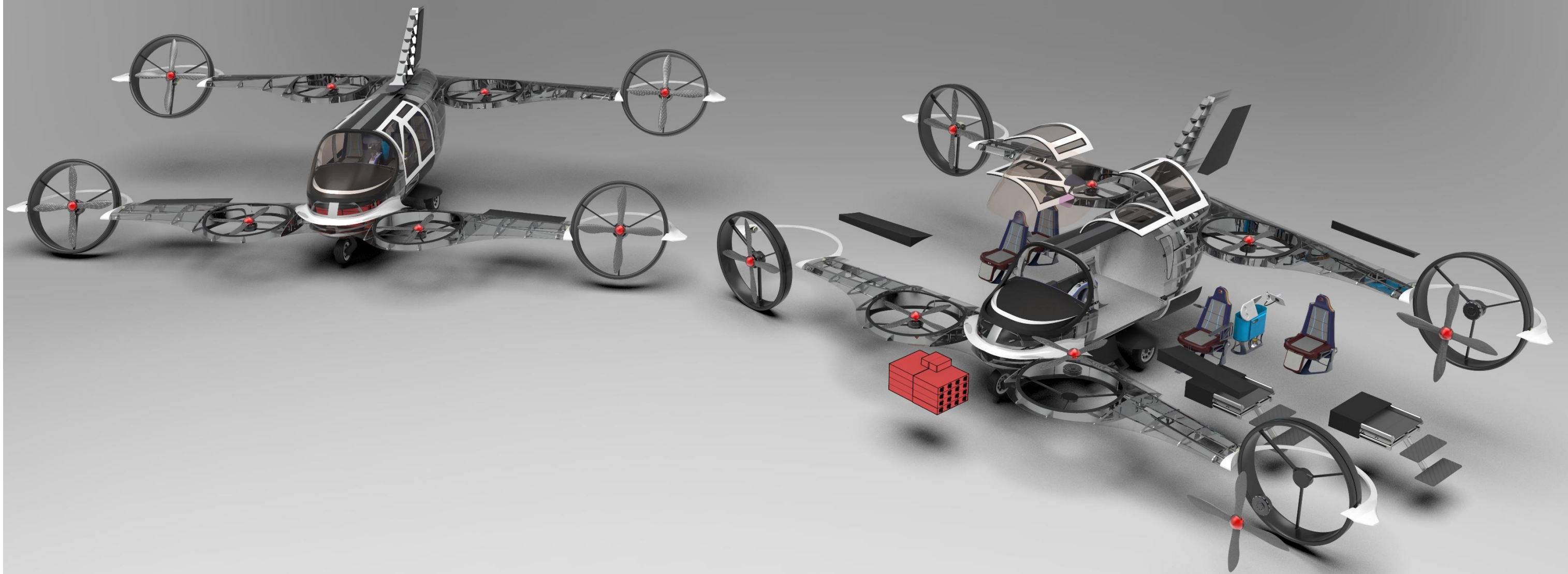
19. Safety & Risk Assessment

Safety is one of our main objectives in design as aircrafts in this category needs to pass every safety regulations and these regulations will logically be stricter in urban areas. We do a risk assessment by finding our failure modes and contemplate some solutions to mitigate those risks. Since the regulations for this category are not written, we decide to comply FAR23 for cruise phase and FAR27 for hover phase.

19.1. Failure Modes

Risks		Probability	Severity	Risk Mitigation	Probability	Severity
One Engine Out	Cruise	Low	Moderate	Ability of landing with 2 motors	Low	Low
	Hover	Low	High	Ability to hover with .. motors	Low	Low
Two Engine Out	Cruise	Very low	High	Emergency Conventional Landing	Low	Low
	Hover	Very low	Very high	Redundant	Very low	Very low
Midair collision		Moderate	High	ATC and ADSP	Very low	Low
Bird Strike		High	High	Use stretched Acrylic for Canopy	Moderate	Moderate
Autonomous system Failure		Moderate	High	Pilot	Low	Low
Battery Failure		Low	High	Conventional Landing	Low	Low

Considering abovementioned risks and their mitigation, we can decisively claim that Spricho can compete in the market as a safe urban air taxi.

20. Cost Estimation of Aircraft

In this section, modified Roskam (58) and Eastlake (59) methods are used to estimate flyaway, unit, and operating cost of electric aircraft. In this section, all costs are reported in 2019 USD.

20.1. Avionics, Instruments and Motors

In this part, avionics and motors' costs are accurately calculated.

20.1.1. Motors

For calculating a customized electric motors cost, an equation is developed by considering a regression based on widely used EMRAX (60) products. This equation and its diagram are shown in Figure 140. Cost of a single electric motor

$$y = 0.0022x^3 - 0.4209x^2 + 48.62x + 1612.1$$
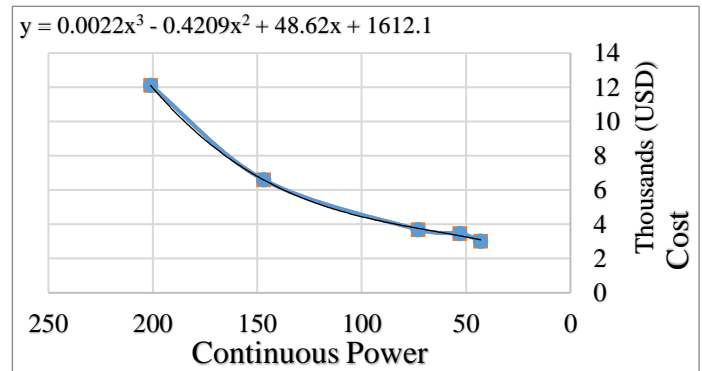
Figure 140: Correlation for calculating electric motor cost

can be estimated based on its maximum continuous power. So, a 147 HP electric motor costs 6700 USD.

20.1.2. Avionics and Instruments

Bottom-up method is used to find avionics cost. The cost of avionics and instruments of a single Spricho is 111655 USD. The cost breakdown is shown in Table 53.

As Spricho starts operating autonomously, flight displays, HUD, and pilot controls are eliminated. As a result, avionics and instrument cost will decrease to 72090 USD.

Table 53: Avionics and instruments components ((61) (62) (63) (64) (65)).

Name	Cost per Unit ($)	Units per Aircraft
Skyview HDX	4490	3
Primary Wiring Harness, Ethernet Cable, Network cable	170	3
Network 5 Port Hub	50	2
Network Splitter (primary)	65	1
VHF COM Radio 25khz	1295	1
Knob Control Panel	250	1
Two-Place Stereo Intercom	295	1
Network cable for Radios, intercom and audio	40	1
ADAHRS - Primary and Secondary	2000	1
Autopilot Servos	750	10
Servo Mounting Brackets Kits	75	10
Network cable for autopilot	40	2
Servo Wiring kit	55	10
AOA/Pitot Probe, Heated w/controller	450	2
Backup Battery	180	3

Pitot/Static/AOA Pneumatic Installation Kit	115	2
Engine controller unit	440	8
Network cable for engine controller	40	24
Class 1, Mode-S, FAA 2020 ADS-B Out compliant	2200	2
Traffic/Weather	995	2
High Integrity GPS for 2020 - Compliant ADS-B Out	590	2
third party IFR navigator	450	1
Wi-Fi Adapter for SkyView	35	1
WASP-200 LRF (AGL Sensor)	500	2
SanDisk 2TB Extreme Portable External SSD - USB-C, USB 3.1	350	6
Lambda quad premium 4x RTX 2080 Ti	11309	2
Arduino 2560	100	2
MGF Skydisplay HUD	25000	1
Yoke, Throttle control, Rudder Pedals, and collective	1000	1
FLIR Vue R 640, 32° FOV, 19MM, 30HZ (IR Camera)	4849	2
Lumenera LT965R (EO camera)	3600	2
E.L.T. 406 WITH GPS	1279	1

20.2. Unit Cost

In this part, RDT&E and manufacturing cost are estimated for calculating flyaway cost, assuming 22 years of production.

20.2.1.   RDT&E[2]

To estimate RDT&E cost, following assumptions are made [Table 54] In order to accelerate the certification process, considering the level of complexity of Spricho's features, 10 prototypes are considered in this phase.

Table 54: Assumptions for calculating RDT&E cost

Parameter	Value
F_{diff} (judgmental factor for difficulty (i.e. complexity))	1.5
F_{CAD} (judgmental factor for the effect of computer aided design)	1
Engineering dollar rate per hour	120 (USD/Hour)
Manufacturing labor rate per hour	35 (USD/Hour)
Tooling labor rate per hour	60 (USD/Hour)
Number of prototypes	10
Rate of manufacturing prototypes	0.33 (Unit/month)
F_{mat} (Correction factor that depends on materials)	2.5
F_{Fin} (Finance Rate)	0.15

---

[2] RDT&E profit is not included in this section.

Total RDT&E cost will be 38.245 million USD. The Breakdown is shown in Table 55.

Table 55: RDT&E cost breakdown

Parameter			Cost (in million USD)
Engineering			5.075
Development, Support and Testing			0.299
Flight Test Operation			0.179
Autonomous Development			4.800
Flight Test Airplanes	**Parameter**	**Value (in million USD)**	24.414
	Avionics and engines	0.722	
	Manufacturing Labor Cost	10.952	
	Materials	3.388	
	Tooling	7.926	
	Quality Control	1.423	

The contribution of RDT&E phase in flyaway cost is shown in Figure 141.

As shown in Figure 141, producing less than 450 units of aircraft is not reasonable, and it is financially logical to produce more than 2000 units of aircraft to reach a RDT&E cost per aircraft lower than 20000 USD.
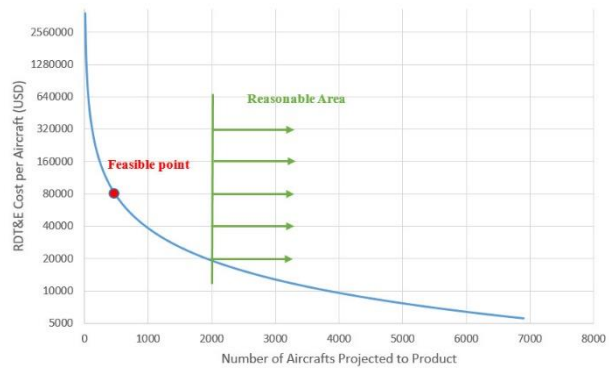
Figure 141: Contribution of RDT&E Phase to Flyaway

20.2.2. Manufacturing[3]

Manufacturing program begins in 2026 with initial production rate of 8.33 aircraft per month. This phase of production can help us to find failures in production line. At the end of the first phase (2028), second phase of production will begin and production rate will increase to 19.7 aircraft per month. Second phase programmed to last 5 years (2028-2033). Third phase of production will start with the same production rate of second phase, but in this phase, assumed battery cost will decrease. Figure 142. 4th phase of production will begin by starting autonomous operation. Some of instruments can be eliminated and unit cost will decrease. 5th and final phase of production will begin with another reduction in assumed battery cost.

Cost of batteries is not considered in Roskam method and is added separately. to estimate the cost of batteries, results of an article from U.S.
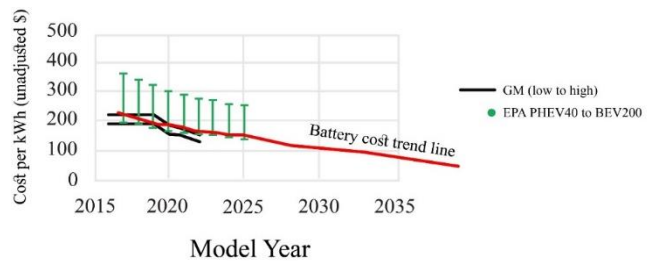
Figure 142: Estimated Battery Cost

---

[3] Manufacturing profit is not included in this section.

Environmental Protection Agency (66) are used and it is reasonable to consider 110$/kwh as battery cost

(67). This changes to 90 USD/kwh at 2033, followed by 65 USD/kwh at 2036, and 55 USD/kwh for 2038. These costs

will be considered to calculate the unit cost of the aircraft in each phase of production.

Manufacturing cost is calculated by taking into account the following assumptions.

Table 56: Manufacturing Cost Estimation Assumptions

Parameter	Value
Number of aircraft built in 1st phase of production	200
Number of aircraft built in 2nd phase of production	1182
Number of aircraft built in 3rd phase of production	710
Number of aircraft built in 4th phase of production	472
Number of aircraft built in 5th phase of production	2366
Flight test hours per aircraft	2
F_{Fin} (Finance Rate)	0.10

Total manufacturing cost will be 1982.815 million USD. The breakdown is shown in Table 57.

Table 57: Manufacturing Cost Breakdown

Parameter	Cost (in million USD)
Engineering	15.493
Avionics, Instruments, and Engines	771.441
Interior	192.703
Manufacturing Labor	271.550
Materials	457.264
Tooling	23.391
Quality Control	35.301
Flight Test Operation	3.549
Batteries	94.596
Finance	186.529

Considering the results of RDT&E and manufacturing cost, unit cost of the aircraft in each phase, can be estimated.

This estimation was done for different profit margins, and these profit margins are selected based on having reasonable

selling plan and maintaining at least 15% of overall profit margin. Results of this estimation are shown in Table 58.

Table 58: Unit Cost Estimation Results with Selling Plan

Phase Section	Duration (years)	Flyaway Cost (K USD)	Profit Margin (%)	Selling Price (K USD)
1st Phase	2 (2026-2028)	499	0	499
2nd phase	5 (2028-2033)	457	10	499
3rd phase	3 (2033-2036)	452	10	493
4th phase	2 (2036-2038)	401	22	482
5th phase	10 (2038-2048)	398	22	478

A brief comparison between electric powered aircrafts is presented in Table 59.

Table 59: A brief comparison between electric powered aircrafts

Name	VTOL capability	Unit Cost (in thousand USD)	Number of PAX + Pilot(s)	MTOW (lb.)	Cruise Speed (knots)
Spricho	Yes	478-499	3+1/4	4371	142
Sun Flyer 2	No	289	1+1	1900	135
Sun Flyer 4	No	389	3+1	2700	130
GT4	No	408	2+2	3800	310

As shown in Table 59, Spricho's unit cost is very competitive compared to the mentioned rivals.

20.3. Operating Cost

In this section, Eastlake's method is used to calculate operating cost of the aircraft. Some changes are made on this method to adjust it to electric aircraft.

Calculations are based on five production phases. typical/economic mission is considered as the reference mission.

Following assumptions are used for calculating the operating cost:

➢ Using California state electricity prices

➢ Five years' loan for purchasing aircraft with 4.75% of interest rate

➢ Hourly rate for a certified airframe and power plant (A&P) mechanic = 60 USD/Hour

➢ Pilot salary is 40 USD/hour

The operating cost of the aircraft is explained in following paragraphs.

- 1st and 2nd phase of production

Operating cost in 1st and 2nd phases will be 131.4 USD/hour with considering loan repayment and 98.4 USD/hour without considering loan repayment.

- 3rd phase of production

Operating cost in this phase is 130.9 USD/hour with considering loan repayment and 94.8 USD/hour without considering loan repayment all of the aircraft that will be produced during the 3rd phase will operate autonomously.

As shown in Table 60, pilot cost has a large effect on operating cost therefore, using autonomous technology increases the aircraft's cost effectiveness.

- 4th & 5th phase of production

Operating cost for aircrafts that produced in this phase will be 78.8 USD/hour with considering loan repayment and 47 USD/hour without considering loan repayment. Cost of replacement of battery is based on published life-cycle

of battery (section 10.3.6) It will be assumed that fully-charged batteries are used in most energy consuming

missions. The used batteries are used in less energy consuming missions.

Operating cost breakdown of all phases is shown in Table 60.

Table 60:Cost Breakdown of Each Phase.

	1st & 2nd phase of production		3rd phase of production		4th & 5th phase of production	
	With loan	Without loan	With loan	Without loan	With loan	Without loan
Maintenance	16%	22%	16%	22%	27%	46%
Electricity	18%	24%	18%	24%	28%	46%
Insurance	2%	2%	2%	2%	3%	5%
Engine Overhaul	0%	0%	0%	0%	0%	1%
Inspection	1%	1%	1%	1%	2%	2%
Pilot	38%	51%	38%	51%	-	-
Loan Repayment	25%	-	25%	-	40%	-

Table 61: range and energy consumption of missions

Mission Range (miles)	Number of Legs	Energy Consumption (Wh)	Duration of mission (minutes)
60	1	110.52	25.6
30	3	114010	21.75
20	2	76000	14.5
10	1	38000	7.25
60 (W/O pilot)	1	105.73	25.6
30 (W/O pilot)	3	107780	21.75
20 (W/O pilot)	2	71850	14.5
10 (W/O pilot)	1	35920	7.25

According to Table 61 and, life of battery is calculated. The results can be found in Table 62

Table 62: Battery operational flight hours

State	Battery operational flight hours (per pack)
With pilot	354 hours
Without pilot	390 hours

Additional operating cost by battery replacement is calculated based on the results of Table 62. This additional

operating cost can be found in Table 63.
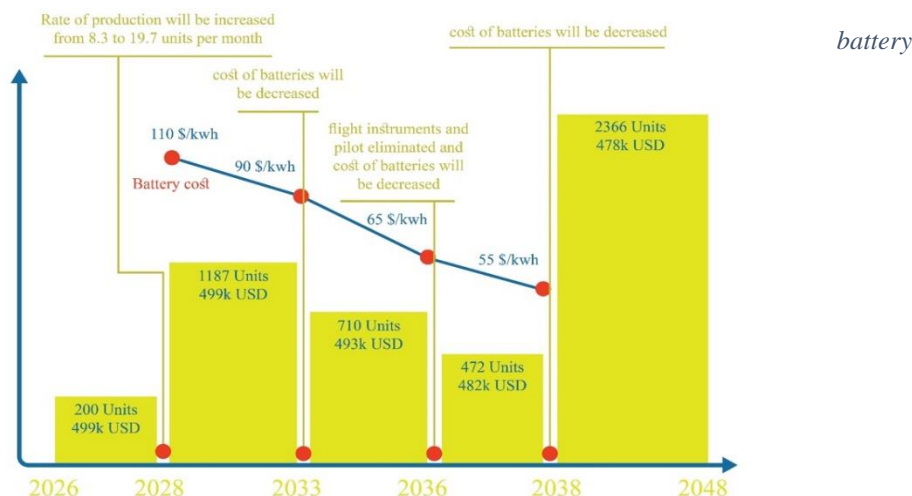
Table 63: Additional operating cost by replacement

battery

Figure 143: manufacturing and operating phases of aircraft

Time line	2028-2033	2033-2036	2036-2038	After 2038
Description	With pilot and 110 USD/kwh for battery cost	With pilot and 90 USD/kwh for battery cost	Without pilot and 65 USD/kwh for battery cost	Without pilot and 55 USD/kwh for battery cost
Additional Operating cost (USD/hour)	78	63.8	41.85	35.4

After calculating additional operating cost, total operating cost of aircraft is determined. The results are shown in

Table 64.

Table 64: Total operating cost of aircraft

Time line		2028-2033 (1st and 2nd phase of production)	2033-2036 (3rd phase of production)	2036-2038 (4th phase of production)	2038-2048 (5th phase of production
Total operating cost (USD/hour)	With loan repayment	209.4	194.7	120.65	114.2
	Without loan repayment	176.4	158.6	88.85	82.4

A brief description of manufacturing and operating phases of aircraft is shown in Figure 143.

20.4. Operating Cost of Operators

In this chapter, operating cost of the operator company is calculated to determine the trip cost. It is assumed that

all facilities for operation are provided with a 10-year loan with 3% of interest rate.

There are 3 phases for operator company. The first phase includes the loan repayment of aircraft and vertiports. The second phase includes loan repayment of vertiports, and third phase does not include any loan repayment.

Cost of facilities (Vertiports) is calculated using bottom-up method. following assumptions are used in calculations.

- Installation Labor factor = 0.4

- Major urban, and sub-urban and maintenance vertiports are 24 hours operative

- Minor urban vertiports are 20 hours operative

- Sightseeing vertiports are 14 hours operative

- There is one air traffic controller for each Vertiport

- There is one air traffic control center for each network, this air traffic control center

Vertiport equipment cost is calculated based on Table 65.

Table 65: Equipment Quantity for Each Vertiport Type

Element	Cost Per Unit (USD)	Sightseeing Vertiport	Sub-Urban Vertiport	Major Urban Vertiport	Minor Urban Vertiport[4]	Maintenance Vertiports
Station for landing and takeoff	37100 [reference]	4	10 (+3[5])	6	3 (+3)	3
Aircraft Batteries storage per Station		5	5	5	5	4
Chargers (every stored battery pack has one charger)	1200 []	1000	2500	1500	750	600
Robotic Lift Truck	15000	8	20	12	6	6
Elevator	50000	1	3	2	2	2
Hydraulic lift equipment for batteries	5000	40	100	60	30	24
Portable Foam Unit	1000	2	5	3	2	5
Safe Melt	65	8	20	10	8	20
Perimeter Light	575	64	160	96	48	48
Flood Light	595	16	40	24	12	12
Light Control Unit	4425	2	2	2	2	2
Weather Station	5450	1	1	1	1	1
Wind Cone (with replacement)	3200	1	1	1	1	1
Light Replacements	405	20	50	30	15	15

---

[4] Maintenance operation service will be done in this Vertiports []
[5] Reserve stations for aircraft storage

Crash Rescue Locker	2250	2	3	2	4	10
Hydraulic Power Cutting	4250	2	3	2	4	10
First Air Kit	950	4	10	8	4	4
Trolling Case with Tools	3400	2	3	2	6	16
Surge Protector	2300	2	2	2	2	2
Portable Lighting System	8950	1	3	2	1	1
Stretcher (ST66011)	190	4	10	6	4	4
Ambulance Stretcher	500	4	10	6	4	4

Results of cost estimation for Vertiports are shown in Table 66.

Table 66: Vertiports Construction Cost and number of vertiports per area

	Sightseeing Vertiport	Sub-Urban Vertiport	Major Urban Vertiport	Minor Urban Vertiport	Maintenance Vertiports
Cost in million USD	**4.09**	**9.536**	**5.882**	**3.864**	**4.052**
Number of Vertiports per area	**18**	**30**	**35**	**50**	**3**

Construction cost of air traffic control tower will be assumed 8 million USD, this assumption is based on trends of constructing an air traffic control tower in airport.

After calculating construction cost of vertiports and ATC tower, cost of vertiport's personnel should be calculated. Quantity of air traffic controllers will be based on number of vertiports, but they are not necessarily located in vertiports. These assumptions can be found in Table 67.

Table 67: Vertiport personnel cost assumptions

Quantity of personnel	Security	Ground Crew	Cleaning and Service	Air Traffic Controller
Hourly labor rated (USD/Hour)	20	20	30	40
Sightseeing Vertiport	2	4	2	1
Sub-Urban Vertiport	4	10	4	2
Major Urban Vertiport	2	6	2	2
Minor Urban Vertiport	2	6	2	1
Maintenance Vertiports	4	0[6]	8	1

Effects of mentioned assumptions on operating cost is shown in Table 68.

Table 68: Vertiport and ATC tower operating cost per aircraft

Vertiports and ATC tower operating cost   156.8

---

[6] Cost of ground crew for maintenance has been considered in operating cost section

Vertiports and ATC tower operating cost without loan repayment   **121.5**
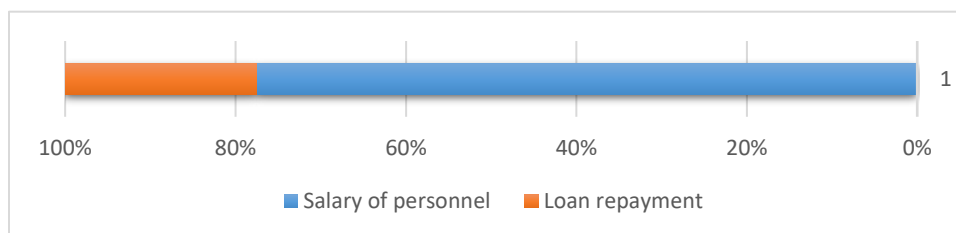

Figure 144: Breakdown of Vertiports and ATC tower operating cost

Total operating cost for operator per aircraft considering aircraft, vertiport, and ATC tower in Table 69. This total calculated by assuming a fleet of aircrafts that produced in 1st & 2nd phase of production and entering into service by 2028.

Table 69: Total operating cost for an operator company

Operation Phase	First 5 years	5-8 years after entry	8-10 years after entry	After 10 years of entry
Assumption	Pilot and loan repayment of facilities and aircrafts included	Loan repayment of aircraft eliminated and battery replacement cost decreased	Pilot cost eliminated and battery replacement cost decreased	Loan repayment of Vertiports and ATC tower eliminated and battery replacement cost decreased
Operating Cost (USD/hour)	366.2	319.0	247	205.3

20.5. Trip Cost

By calculating the total operating cost of operator per flight hour (Table 69), trip cost is determined for each operating phase, these calculations are done based on the typical mission of the RFP and a 10% profit margin. Trip cost and ticket price list can be found in Table 70.

Table 70: Trip cost and ticket price

Operation Phase	First 5 years	5-8 years after entry	8-10 years after entry	After 10 years of entry
Trip Cost (USD)	157	137	106	88
Ticket Price (USD)	87	76	59	49

It is necessary to compare this ticket price with other transportation modes. A comparison between different modes of transportation is shown in Table 71. In this comparison it is assumed that 2 passengers share a cab.

Table 71: Comparison between transportation methods based on ticket price in same distance (except Uber Elevate)

Vehicle	Average Speed (mph)	Block time (guessed in minutes)	Ticket Price (in USD for a single PAX)
Spricho (2028-2033)	140	25.6	87
Spricho (2033-2036)	140	25.6	76
Spricho (2036-2038)	140	25.6	59
Spricho (after 2038)	140	25.6	49
Uber Elevate in initial (51.3 mi) (68)	171	18	153
Uber Elevate in near term (51.3 mi)	171	18	50
Uber Elevate in long term (51.3 mi)	171	18	24
Cable car	8.1	440	7
Metro	33	110	2.75
Taxi (with 2 PAX)	42	85	84
Bus	12.2	295	2.25

As shown in Table 71, Spricho has a very competitive ticket price (even in its most expensive ticket price).

In comparison to claims of Uber Elevate project, our ticket price initially is lower, but in long term, Uber Elevate's proposed ticket price is lower than ours. But we believe that our presented cost model has more elements and it is more accurate.

21. Design Verification

In this section, the final design has been reviewed and verified through an extensive numerical verification process; CFD analysis, FEM, and Modal analysis have been performed and results been discussed.

Figure 145Figure 1 Total deformation caused by max loading

21.1. FEM Analysis

Unconventional configuration of Spricho has necessitated FEM and Modal analysis, to verify the structural design cycle. Deformation, stress, and modal analysis are of interest to be done.

21.1.1. Deformation

Here, the total deformation caused by the maximum loading on the wing during forward flight is presented in, showing a maximum deformation of 1.4486 inches.
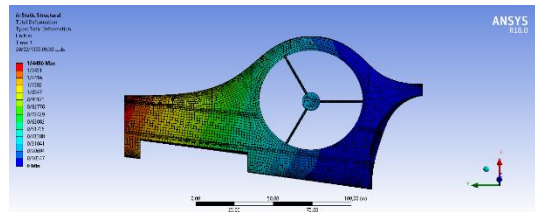
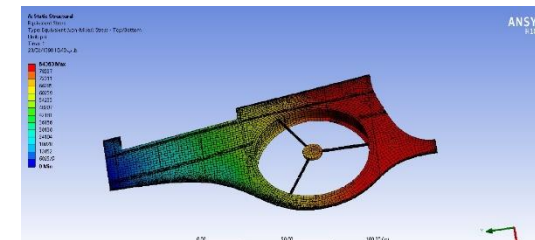

Figure 146Figure 2 Stress analysis caused by max loading

Figure 147Figure 3 mode 1 natural frequency
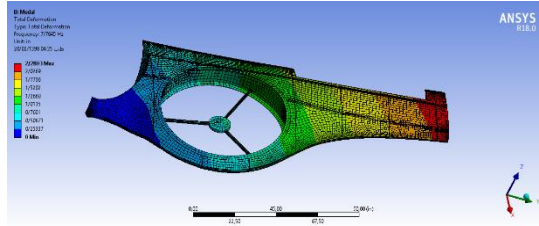

Figure 148Figure 4 mode 2 natural frequency

Figure 151Figure 6 mode 4 natural frequency

21.1.2. Stress Analysis

Based on [Figure 147], stress analysis has been done in maximum loading condition in forward flight. Maximum stress equals to 84 kpsi, which is lower than ultimate strength (349 kpsi).
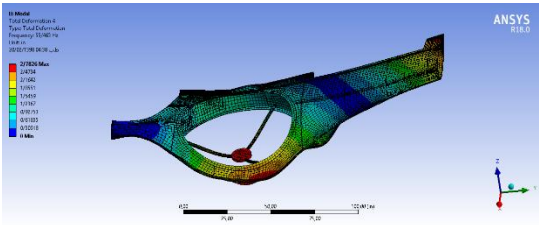
21.1.3. Modal Analysis

These figures represent first four natural frequency modes of the wing, which are 7, 10, 23, and 55Hz. The third one is a torsional mode, while others are bending modes. There are 2 motors embedded in each wing, having rotational speeds of 1800 RPM (30Hz) to 2400 RPM (40Hz). When the motors are st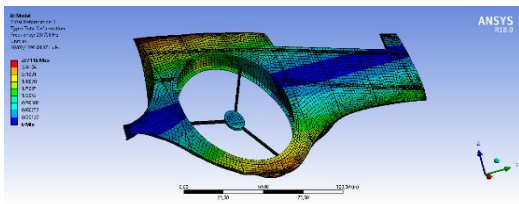arted, the RPM is rapidly increased, reaching the aforementioned RPMs. Hence, the natural frequency of the wing is not excited.
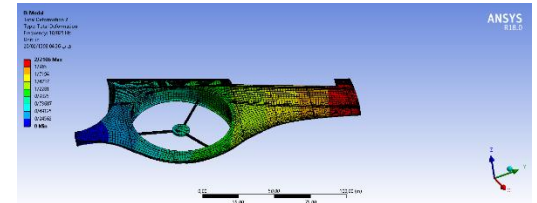

Figure 149Figure 5 mode 3 natural frequency

In conclusion, based on the analysis results, motor vibrations are of no concern and the structural design performed at previous design steps has been verified.

21.2. CFD Analysis

In this step of the design verification, two topics have been covered; downwash effect of the fore wing on the aft wing, which has been feedbacked to lift distribution analysis [lift section], and analyzing wing aerodynamic behavior and the effects of front wing duct fans and their lid mechanism. Geometry and results of downwash effects are shown in [fig and fig]. The fore wing downwash on the aft wing at AOA=8º is apparent in [figure]. The effect of this downwash on C_l vs. AOA plot are shown in [figure], for both wings.
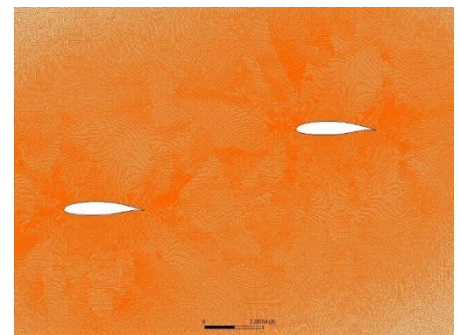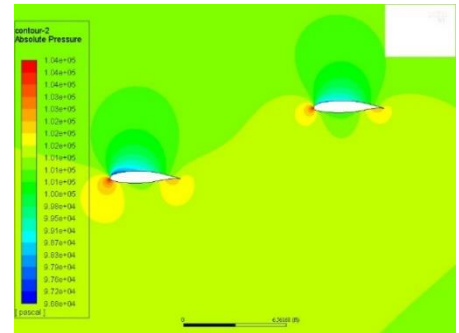

Figure 152Figure 8-geometry for downwash effects

As it can be seen, Aft-wing's lift coefficient is reduced due to downwash effect, as previously mentioned in. The airfoil $C_{l_{alpha}}$ has been calculated to be 5.7325 rad^{-1} in cruise for both wings' airfoils. Whereas the CFD analysis results in the value of 5.165 rad^{-1} for the fore wing and 4.586 rad^{-1} for the aft wing. This represents an 11% and 14% error in calculations, for the fore wing and aft wing, respectively.
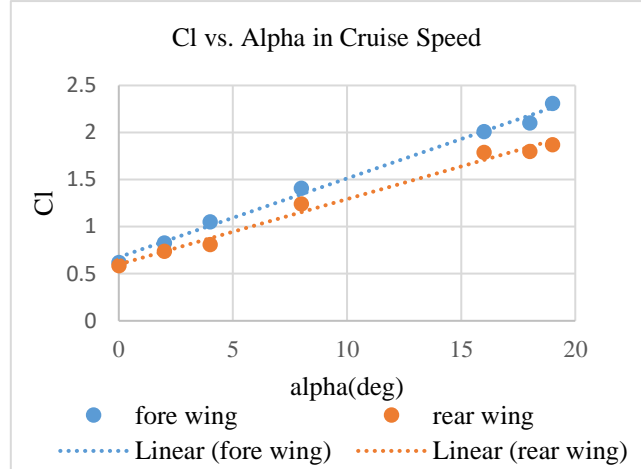

Figure 153Figure 9Table 3-rear and fore wing cl-alpha

To analyze the wing behavior and the effects of duct fan in front of the motor, the wing geometry has been created and is shown in [Figure 158] in three forms; wing without duct, with closed-lid motor, and wing with open-lid motor.
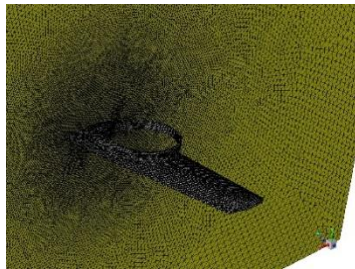

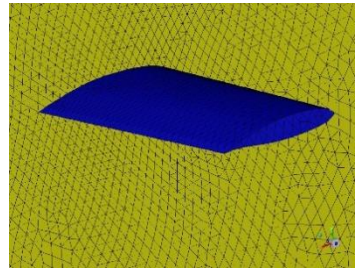*Figure 158Wing with open-lid motor*
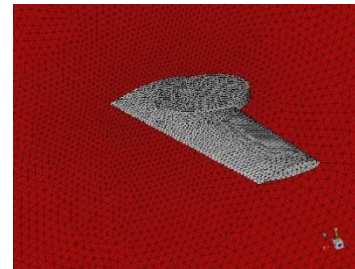

Figure 156Wing without duct

Figure 157Wing with closed-lid motor

Based on figures, there exists a drop in the generated lift (about 10%) and a jump in the drag force (10% and higher), resulting in a reduction of aerodynamic efficiency. By assessing the results, it is concluded that the use of lids for covering the hover motors in airplane-mode is substantially justified. So, it has been decided to consider a lid for each hover motor. Afterwards, the modified wing geometry has been used as the baseline for aerodynamic characteristics calculations.
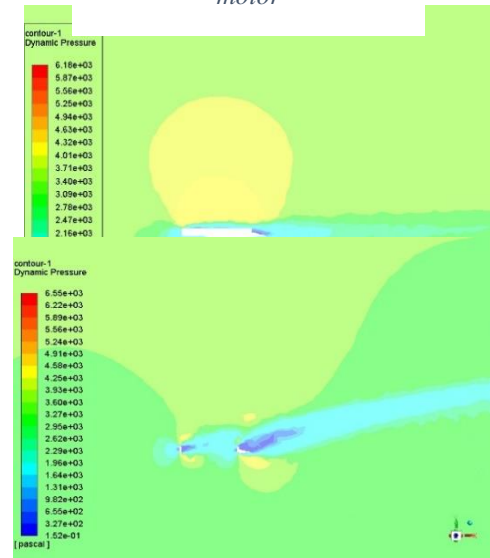

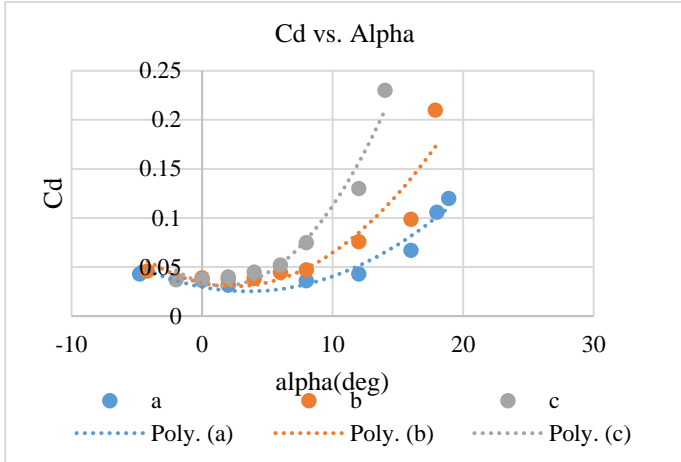*Figure 154Figure 11Dynamic Pressure for open-lid hover motors*

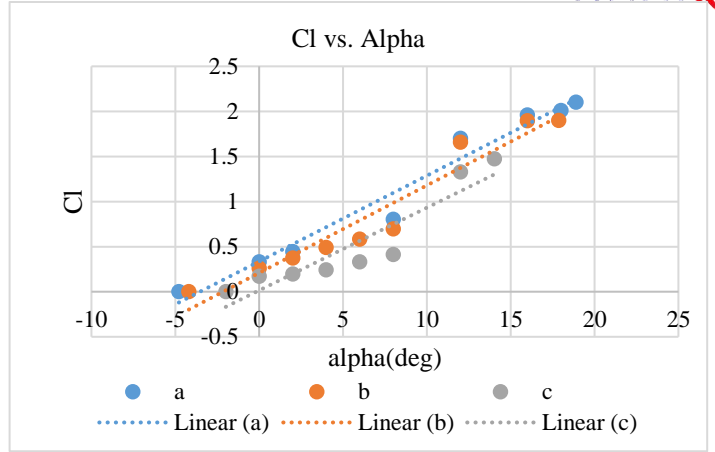*Figure 160Figure 12Cd alpha for three different forms*

Figure 159Cl alpha for three different forms

22. Critical Design Review & Future Work

In this section, the design's feasibility has been measured against a principal merit; total life cycle cost of the aircraft.

22.1. Life Cycle Cost Comparison

A brief comparison between two scenarios has been done; in the 1st scenario, no autonomous equipment or development is considered in aircraft life cycle and in the second one, aircraft development will be initiated with the target of enabling autonomous flight.

Autonomous Spricho renders the presence of pilot unnecessary, thus operating cost [figure 6 of cost] of aircraft will decrease by 51%. Although the unit cost of the autonomous version is higher, but 12 years of operation with autonomous capability, will provide more than 2 million USD reduction in operating cost and will only raise Spricho's unit cost by 36900 USD. In addition, eliminating pilot allows for more passengers, thus increasing operator's profit.

23. References

1] Harold, Essentials of management.

2] "worldbank.," [Online]. Available: http://www.worldbank.org/.

3] "world population," [Online]. Available: http://worldpopulationreview.com/us-cities/.

4] Rayle, "A Survey-Based Comparison of Taxis".

5] Pinedo, Planning and Scheduling in Manufacturing and Services.

6] M. George, Lean Six Sigma for Service.

7] [Online]. Available: http://www.businesssetfree.com/small-business-product-life-cycle/.

8] R.S.King, Cluster Analysis and Data Mining: An Introduction.

9] Vahana, Vahana (Airbus), [Online]. Available: vahana.aero.

10] A. A. Database, "www.ntsb.gov," [Online].

11] Russell, Artificial Intelligence: A Modern Approach.

12] stackoverflow, "www.stackoverflow.com," [Online].

13] faa, "www.faa.gov," [Online].

14] J. Roskam, Airplane Design, 1985.

15] D. F. Finger, A Review of Configuration Design for Distributed Propulsion, Asia-Pacific International Symposium of Aerospace Technology, 2017.

16] "emrax e-motors," 2019. [Online]. Available: https://emrax.com/wp-content/uploads/2017/10/user_manual_for_emrax_motors.pdf.

17] P. O. Jemitola, "Box wing aircraft conceptual design," Department of Aerospace Engineering, Cranfield University, 2012.

18] L. Rauno Cavallaro, "Challenges, ideas, and innovations of joined-wing configurations: a concept from the past, an opportunity for the future," *Progress in Aerospace Sciences,* 2016.

19] R. Merino-Martinez, "Design and analysis of the control and stability of a Blended Wing Body aircraft," Polytechnic University of Madrid (UPM), 2014.

20] L. C. Xinhua Wang, "Mathematical modeling and control of a tilt-rotor aircraft," *Aerospace Science and Technology,* 2015.

21] M. M. Gabriele Di Francesco, "Modeling and Incremental Nonlinear Dynamic inversion of a Novel Unmanned Tiltrotor," *Journal of Aircraft,* 2015.

22] L. C. Xinhua Wang, "Mathematical modeling and control of a tilt-rotor aircraft," *Aerospace Science and Technology,* 2015.

23] P. L. Trainelli, "The Tandem Wing: Theory,Experiments, and Practical Realisations," POLITECNICO DI MILANO university, 2013/2014.

24] J. Wolkovitch, "Subsonic VSTOL Aircraft Configurations with Tandem Wings".

25] www.airfoiltools.com, "http://airfoiltools.com/airfoil/details?airfoil=ls417-il," [Online].

26] B. W. McCORMICK, "AERODYNAMICS,AERONAUTICS,AND FLIGHT MECHANICS," 1979.

27] D. P. RAYMER, "Aircraft design: a conceptual approach," 1989.

28] D. Scholz, "Estimating the Oswald factor," 2012.

29] A. A. Analysis, AAA.

30] Z. Z. Zhi-chrng, "Analysis on the transition mode of lift-fan VTOL," 2011.

31] Stephen A. Rizzi Daniel L. Palumbo Jonathan Rathsam and Andrew Christian, "Annoyance to Noise Produced by a Distributed Electric Propulsion High-Lift System," *American Institute of Aeronautics and Astronautics,* 2018.

32] m. A. fahad s. al badawi, "Reliability modelling and assessment ofelectric motor driven systems in hydrocarbon industries," *The Institution of Engineering and Technology,* pp. 606-607, 2015.

33] "roland berger," [Online]. Available: https://www.rolandberger.com/publications/publication_pdf/roland_berger_aircraft_electrical_propulsion.pdf.

34] "solid energy systems," [Online]. Available: http://assets.solidenergysystems.com/wp-content/uploads/2017/09/08171937/Hermes_Spec_Sheet1.pdf.

35] j. lilly, "aviation propulsive lithiu-ion battery packs state-of-charge and state-of-health estimations and propulsive battery system weight analysis," *embry riddle aeronautical university,* pp. 19-21, 2017.

36] J. O. H. L. Jaewan Kim, "Review on battery thermal management system for electric vehicles," *ELSEVIER,* pp. 195-201, 2019.

37] S. M. b. M. A. a. A. S. b. H. M. R. Saidur a, "Applications of variable speed drive (VSD) in electrical motors energy savings," *ELSEVIER,* 2012.

38] M. D. Kankam, "A survey of power electronics applications in aerospace technologies," *NASA*.

39] J. D. A. Jr, Aircraft performance and design, The McGraw-Hill companies, 2010.

40] Y.-H. Liu, "Search for an Optimal Rapid Charging Pattern for Lithium–Ion Batteries Using Ant Colony System Algorithm," *IEEE,* 2005.

41] A. R.-S. Ashraf M Kamal, "Design methodology for hybrid (VTOL + Fixed Wing) unmanned aerial vehicles," Aeronautics and Aerospace Open Access Journal, 2018.

42] J. Roskam, Airplane Design, Part 2, 1985.

43] K. Karling, "Aerodynamics of the Viggen 37 aircraft," NASA Technical Memorandum, 1986.

44] J. Roskam, Airplane Flight Dynamics and Automatic Flight controls, Part 1, 2001.

45] J. Roskam, AIrplane Design, Part 5, 1985.

46] USAF, "MIL-F-9490D".

47] D. McLean, Automatic Flight Control Systems, 1990.

48] R. L. Gerardo Flores, "6-DOF Hovering controller design of the quad tiltrotor aircraft: simulations and experiments," *IEEE Conference on Decision and Control,* 2014.

49] L. C. Xinhua Wang, "Mathematical modeling and control of a tilt-rotor aircraft," *arxiv.org,* 2015.

50] W. Z. X. W. Laohu Yuan, "Study on model and simulation of the tilt rotor aircraft in transition mode," *International Conference on Advances in Mechanical Engineering and Industrial Informatics.*

51] S. N. John Seddon, Basic Helicopter Aerodynamics, 2011.

52] Q. X. W. W. Li Haixu, "Multi-body Motion Modeling and Simulation for Tilt Rotor Aircraft," *Chinese Journal of Aeronautics,* 2010.

53] M. S. K. a. O. T. Ozlem Armutcuoglu, "Tilt Duct Vertical Takeoff and Landing Uninhabited Aerial Vehicle Concept Design Study," *Journal of Aircraft,* 2004.

54] L. L. a. K. Turkoglu, "Robust H_∞ Loop-Shaping Differential Thrust Control Methodology for Lateral/Directional Stability of an Aircraft with a Damaged Vertical Stabilizer," *AIAA Guidance, Navigation, and Control Conference,* 2016.

55] Anna Douglas , ‖ Rachel Carter, Mengya Li, and Cary L. Pint, "Toward Small-Diameter Carbon Nanotubes Synthesized fromCaptured Carbon Dioxide: Critical Role of Catalyst Coarsening," p. 9, 10 2018.

56] Hexcel, "HexWeb® Acousti-CAP®broadband sound reducing honeycomb".

57] "Technical Data Sheet: CarbonX™ Carbon Fiber Ultem™ PEI 3D Printing Filament".

58] D. J. Roskam, Airplane design part3 : Layout design of cockpit, fuselage, wing and empennage: cutaway and inboard profiles, 1986.

59] J. Roskam, Airplane Design, 1985.

60] S. Gudmundsson, General Aviation Aircraft Design: Applied Methodes and Procedures.

61] EMRAX E-motors, EMRAX d.o.o., [Online]. Available: https://emrax.com/wp-content/uploads/2017/10/user_manual_for_emrax_motors.pdf.

62] Dynon Avionics, [Online]. Available: http://dynonavionics.com/public_html/yabbfiles/Attachments/Catalog-Dynon-web.pdf.

63] MYGOFLIGHT (MGF), [Online]. Available: https://mgfproducts.com/pages/hud.

64] Lumenera Corporation, [Online]. Available: https://www.lumenera.com/lt965r.html.

65] FLIR, [Online]. Available: https://www.flir.com/products/vue-pro/.

66] Lambda, [Online]. Available: https://lambdalabs.com/deep-learning/workstations/4-gpu.